

Fluid-Structure Interaction

Extended-FEM Approach to Solidification

Daniela Caraeni

Department of Mechanical Engineering

McGill University

Montreal, Quebec

April 2020

A thesis submitted to McGill University

In partial fulfillment of the requirements of the degree of

MASTER OF MECHANICAL ENGINEERING

© Copyright by Daniela Caraeni, 2020

Abstract

The ability of in-flight icing numerical codes to account for the effects of Supercooled Large Droplets (SLD), which are droplets ranging from 50-1000 μm , is still somewhat limited. Solvers that simulate SLD in in-flight icing treat an ensemble of droplets adopting a macroscopic approach, making use of some heuristic correlations based on experiments or extrapolating SLD behavior from smaller non-SLD droplets. Alternatively, taking a microscopic approach and accurately simulating the physics of individual droplets can lead to higher fidelity models when replacing empirical data. Therefore, developing models of a single SLD droplet impingement and solidification can provide a framework that expands the capabilities of current macroscopic solvers to handle water-ice fluid-structure interactions (FSI) and solidification.

This presents challenges such as the evolution of the water-ice interface and the jump in fluid/solid properties due to phase change. This thesis proposes a level set method (LSM) to capture the movement of the interface, and the extended finite element method (XFEM) to sharply account for the discontinuities in the material properties without the need for body-conforming meshes. The number of additional degrees of freedom (DOFs) introduced by the XFEM formulation of the incompressible Navier-Stokes (INS) equations can be eliminated by using static condensation as the interface evolves. Furthermore, the Brinkman penalization method is proposed to model fluid-solid boundaries, while the Stefan condition is used to simulate planar solidification. Ultimately, the loose-coupling of the hydrodynamics with the thermodynamics permits the simulation of solidification along with fluid motion.

Various test cases are used to evaluate the performance of the present methodology. The Brinkman penalization method is validated with several FSI benchmark lid-driven cavity problems. Subsequently, one-dimensional and two-dimensional solidification and melting cases have been employed to verify the implementation of the Stefan condition, and finally the coupled Stefan-hydrodynamics problem is simulated and compared against other numerical methods. The overall results illustrate that the proposed framework can efficiently solve multiphase flows along with solidification and FSI.

Résumé

La capacité des codes numériques à prendre en compte les effets des grosses gouttelettes surfondues (dites SLD), de diamètre compris entre 50 et 1000 μm , lors de simulations du givrage en vol est assez limitée. Les solveurs SLD doivent toutefois faire appel à certaines corrélations heuristiques et macroscopiques basées soit sur des expériences, soit sur une extrapolation du comportement des SLD sur la base de plus petites gouttelettes. Par ailleurs, l'adoption d'une approche microscopique et la simulation précise de la physique d'une seule gouttelette, faisant ainsi abstraction des données empiriques, peuvent conduire à des modèles de plus grande fidélité. Par conséquent, le développement d'un modèle microscopique fournissant des informations sur le comportement lors de l'impact et de la solidification d'une gouttelette pourrait augmenter la fidélité des codes en introduisant les interactions fluide-solide (dites FSI) et le phénomène de solidification de tels écoulements multiphasiques.

Ceci présente plusieurs défis tels que le suivi de l'évolution de l'interface et du saut des propriétés fluide/solide dus au changement de phase. La présente thèse propose l'utilisation de la méthode des surfaces de niveau (LSM) pour suivre le mouvement de l'interface, et la méthode des éléments finis étendus (dits XFEM) pour prendre en compte les discontinuités dans les propriétés des matériaux. La méthode XFEM fournit un traitement précis de l'interface sans nécessiter de maillages conformes. Elle entraîne cependant davantage de degrés de liberté (DOFs) dans les équations de Navier-Stokes incompressible (INS); éliminées au fur et à mesure par condensation statique. La méthode de pénalisation de Brinkman a été implémentée afin de modéliser les conditions aux frontières fluide/solide et la formulation dite classique du problème de Stefan a été retenue et mise en œuvre pour modéliser la solidification plane. Enfin, le couplage lâche entre hydrodynamique et thermodynamique permet de simuler la solidification du fluide en mouvement.

De multiples cas tests sont utilisés pour valider la méthodologie développée dans cette thèse. La méthode de pénalisation de Brinkman est validée à l'aide de plusieurs cas canoniques mettant en jeu une cavité avec ou sans convection forcée. Ensuite, des cas tests unidimensionnels et bidimensionnels ont servi à valider la résolution du problème de Stefan, et finalement, le couplage Stefan-hydrodynamique est simulé et comparé à d'autres approches numériques. Les résultats

obtenus montrent que l'approche proposée est capable de traiter de façon efficace les écoulements multiphasiques avec FSI et solidification.

Acknowledgements

I would like to express my deepest gratitude to my thesis supervisor, Professor Wagdi G. Habashi for his mentoring and generous support throughout my research. I am also thankful for the guidance and direction I have received throughout my work from Dr. Ahmed Bakkar and Dr. Vincent Casseau, post-doctoral fellows at McGill University's CFD Laboratory. I would like to thank all my colleagues at the CFD Lab, who have taken the time to impart good advice and to lend their support.

I wish to acknowledge the Natural Sciences and Engineering Research Council of Canada for funding the research through a Discovery grant. I am thankful for the system administrators, Jesse Stacey, Lily Huang, Olivier Zheng, and David Wang, for their technical support with the CFD Lab's important computing resources.

Lastly, I would like to express my gratitude to my family and friends for their encouragement and support throughout my studies.

Nomenclature

Abbreviations

BVP	Boundary Value Problem
DOF	Degrees of Freedom
FAA	Federal Aviation Administration
FEM	Finite Element Method
GLS	Galerkin Least-Squares
IB	Immersed Boundary
IBM	Immersed Boundary Method
LSM	Level Set Method
NS	Navier-Stokes
INS	Incompressible Navier-Stokes
PDE	Partial Differential Equation
PU	Partition of Unity
PUM	Partition of Unity Method
SDF	Signed Distance Function
SLD	Supercooled Large Droplets
SUPG	Streamline-Upwind Petrov-Galerkin
VOF	Volume of Fluid
VMS	Variational Multiscale

TG	Taylor-Galerkin
2TGVMS	2 nd order implicit Taylor-Galerkin Variational Multiscale
XFEM	Extended Finite Element Method

Greek Letters

α	Thermal expansion coefficient
α_l	Thermal diffusivity of liquid
α_s	Thermal diffusivity of solid
β_u	Penalization forcing term for Navier-Stokes equations
β_T	Penalization forcing term for the energy equation
δ	Delta function
Γ	Interface separating the phases
λ	Root of Stefan problem transcendental equation
μ	Fluid dynamic viscosity
ν	Fluid kinematic viscosity
v	General variable
v^e	Nodal value of a general variable
v^{enrich}	Enrichment nodal value of general variable
φ	Enrichment function

ϕ	Signed distance function
ρ	Density
ρ_l	Fluid density
ρ_s	Solid density
τ	Stabilization parameter
τ_e	Matrix of stabilization parameters
Ω	Computational domain
Ω_e	Element domain
Ω_l	Liquid Computational domain (with negative level set values)
Ω_s	Solid Computational domain (with positive level set values)

Symbols

a_i	Velocity vector at the previous iteration
c_p	Specific heat capacity at constant pressure
$d(x_i)$	Distance function
ϵ_c	Surface tension coefficient
ϵ_v	Kinetic mobility coefficient
$f(x_i)$	Source parameter
h_{cl}	Element characteristic length
F_i	Body forces vector

g_i	Gravitational acceleration vector
h_{ele}	Element size
i, j	Spatial dimensions
k	Thermal diffusion coefficient
κ	Surface curvature vector
$M(x_i)$	Enrichment shape functions
n_i	Surface normal vector
n_{elem}	Number of elements in the discretized domain
$N(x_i)$	Standard shape functions
P	Pressure
p^{enrich}	Enriched pressure
Pr	Prandtl number
Re	Reynolds number
Ri	Richardson number
s	Source function
$sign(\phi)$	Sign function
t	Time
T	Temperature
T^{enrich}	Enriched temperature
T_l	Temperature of liquid

T_m	Melting temperature
T_s	Temperature of solid
u_i	Velocity vector
u_i^a	Average velocity vector in time
u_x	X-component of the velocity vector
u_y	Y-component of the velocity vector
x_i	Euclidean vector
$x_{i,int}$	Euclidean vector of interface nodes
w, q	Standard Galerkin test functions

List of Figures

Figure 2-1 Freezing profile of water as a function of freezing time [32]	5
Figure 2-2 Schematic diagram for water droplet freezing on impact. (a) $tnuc < 30$ ms, (b) $30 \text{ ms} \leq tnuc \leq 600$ ms, (c) $tnuc > 600$ ms which is similar to supercooled water nucleation time [35]	6
Figure 2-3 Nucleation in a water drop [36]	6
Figure 2-4 Dendritic freezing in a water drop [36]	7
Figure 2-5 Planar solidification in a water drop [36]	8
Figure 2-6 Enriched elements	14
Figure 4-1 Geometric splitting of domain with red dashed line as the interface	31
Figure 4-2 Equal splitting of domain with red dashed line as the interface	32
Figure 4-3 Schematic representation of solidification domain	33
Figure 4-4 Element interface calculation	35
Figure 4-5 Characteristic lines showing the extension of interface speed	36
Figure 4-6 Min-Heap data structure	42
Figure 5-1 Lid-driven cavity with embedded cylinder boundary conditions	46
Figure 5-2 Streamlines for the lid-driven cavity flow with an embedded cylinder (left) with the body-conforming mesh, (right) with XFEM	47
Figure 5-3 Velocity contours for the lid-driven cavity flow with an embedded cylinder	48
Figure 5-4 Velocity profiles for the lid-driven cavity flow with an embedded cylinder: distribution of velocity component u along the vertical midline	49
Figure 5-5 Velocity profiles for the lid-driven cavity flow with an embedded cylinder: distribution of velocity component v along the horizontal midline	49
Figure 5-6 Forced convection with no obstruction: cavity flow domain and boundary conditions	50
Figure 5-7 Temperature profiles for flow with $Re = 1000$ and $Pr = 1.0$ at steady-state: distribution of temperature along the vertical midline	51
Figure 5-8 Temperature profiles for flow with $Re = 1000$ and $Pr = 1.0$ at steady-state: distribution of temperature along the horizontal midline	52
Figure 5-9 Square obstruction with forced convection: flow configuration and boundary conditions	53

Figure 5-10 Isotherms in the cavity with central blockage placement at $Ri = 0.1$ and $B = 0.25$..	54
Figure 5-11 Streamlines in the cavity with central blockage placement at $Ri = 0.1$ and $B = 0.25$ with (left) body-conforming mesh (right) embedded blockage	55
Figure 5-12 Isotherms in the cavity with central blockage placement at $Ri = 0.1$ and $B = \frac{1}{4}$ with (left) body-conforming mesh (right) embedded blockage	55
Figure 5-13 Temperature profiles in the cavity at $Ri = 0.1$ and $B = 1/4$ at horizontal midline	56
Figure 5-14 Temperature profiles in the cavity at $Ri = 0.1$ and $B = 1/4$ at vertical midline	56
Figure 5-15 Domain setup for the 1D solidification problem.....	57
Figure 5-16 Interface location for 1D solidification problem.....	58
Figure 5-17 Non-dimensional interface location comparison for an infinite corner at 0.025 sec	60
Figure 5-18 Non-dimensional interface location for an infinite corner at 0.025 sec for three mesh refinements.....	61
Figure 5-19 Velocity contours for flow over a cylinder	63
Figure 5-20 Velocity norm at midline for flow over a cylinder	64
Figure 5-21 Maximum velocity in a thermal cavity with natural convection.....	65
Figure 5-22 Interface location of tin melting at $t=200$ s, $t=400$ s, and $t=750$ s	66
Figure 5-23 Temperature of tin melting at centerline at $t=200$ s	67
Figure 5-24 Temperature of tin melting at centerline at $t=400$ s	67
Figure 5-25 Temperature of tin melting at centerline at $t=750$ s	68
Figure 5-26 Interface shape and position of melting cylinder in high Re flow	69
Figure 5-27 Velocity contours (in m/s) of melting cylinder in high Re flow, at $t = 1$ sec.....	69
Figure 5-28 Velocity contours (in m/s) of melting cylinder in high Re flow, at $t = 10$ sec.....	70
Figure 5-29 Velocity contours (in m/s) of melting cylinder in high Re flow, at $t = 40$ sec.....	70
Figure 5-30 Velocity contours (in m/s) of melting cylinder in high Re flow, at $t = 70$ sec.....	71
Figure 5-31 Velocity contours (in m/s) of melting cylinder in high Re flow, at $t = 100$ sec.....	71
Figure 5-32 Temperature contours (in K) of melting cylinder in high Re flow, at $t = 1$ sec.....	72
Figure 5-33 Temperature contours (in K) of melting cylinder in high Re flow, at $t = 10$ sec.....	72
Figure 5-34 Temperature contours (in K) of melting cylinder in high Re flow, at $t = 40$ sec.....	73
Figure 5-35 Temperature contours (in K) of melting cylinder in high Re flow, at $t = 70$ sec.....	73
Figure 5-36 Temperature contours (in K) of melting cylinder in high Re flow, at $t = 100$ sec....	74

List of Tables

Table 5-1 Circular obstruction, no convection mesh size	46
Table 5-2 Comparison of the vortices center positions	48
Table 5-3 No obstruction, forced convection mesh size	50
Table 5-4 Square obstruction, forced convection mesh size.....	52
Table 5-5 Circle obstruction, forced convection.....	53
Table 5-6 Frank sphere convergence	62

Table of Contents

<i>Abstract</i>	<i>II</i>
<i>Résumé</i>	<i>III</i>
<i>Acknowledgements</i>	<i>V</i>
<i>Nomenclature</i>	<i>VI</i>
Abbreviations	VI
Greek Letters	VII
Symbols.....	VIII
<i>List of Figures</i>	<i>XI</i>
<i>List of Tables</i>	<i>XIII</i>
<i>Table of Contents</i>	<i>XIV</i>
1 Introduction	1
1.1 Research Motivation	1
1.2 Thesis Outline and Contributions	3
2 Background and Literature Review	4
2.1 Solidification Phenomena in SLD	4
2.2 Body-Conforming versus IBM	8
2.2.1 Continuous Forcing.....	9
Elastic Boundaries IBM	9
Rigid Boundaries IBM	9
Distributed Lagrangian Multiplier.....	10
2.2.2 Direct Forcing	10
Ghost-Cell Method	11
Ghost-Fluid Method	11
Cut-Cell Methods	12
2.3 XFEM	12
2.3.1 Partition of Unity	12
2.3.2 XFEM Formulation.....	13
2.4 Heat Transfer Problems - Solidification/Melting	15

2.4.1	Common Methods of Solving Stefan Problem	16
	Moving Mesh / Mesh-Deformation Methods	16
	Enthalpy Methods	16
	XFEM.....	16
3	<i>Mathematical Models</i>.....	17
3.1	Heat Transfer.....	17
3.1.1	Heat Flux Jump Evaluation.....	18
3.2	Hydrodynamics.....	18
3.3	Interface Capture	19
3.3.1	Level Set Function and Advection.....	19
3.3.2	Interface Speed Extension	19
4	<i>Numerical Modeling</i>.....	20
4.1	FSI.....	20
4.1.1	Arbitrary Lagrangian-Eulerian Method	20
4.1.2	Fictitious Domain	21
4.1.3	Lagrange Multiplier	21
4.1.4	Brinkman Penalization/Penalty Method	21
4.2	INS Equations	22
4.2.1	Galerkin Least Squares	22
	GLS for INS Equations	23
4.2.2	Streamwise Upwind Petrov Galerkin.....	24
	SUPG for INS Equations.....	24
4.2.3	Variational Multiscale.....	25
	VMS for INS Equations	25
4.3	Static Condensation.....	26
4.4	Temperature-Based Energy Equation.....	27
4.5	XFEM	28
4.6	Splitting Approaches with XFEM.....	30
4.6.1	Geometric Splitting.....	30
4.6.2	Equal Splitting	31
4.6.3	Computational Procedure for Fluid-Structure Implementation	32
4.7	Stefan Problem.....	33

4.7.1	Interface Speed	34
4.7.2	Extension of Interface Speed	35
4.7.3	Advection of Level Set with Interface Velocity	36
4.7.4	Conservation of Energy	37
4.8	LSM	38
4.8.1	SDF	38
4.8.2	Level Set Advection.....	39
4.8.3	Level Set Advection with Second-Order Taylor-Galerkin Variational Multiscale Stabilization.....	39
4.8.4	Level Set Reinitialization by Geometric Reconstruction	41
4.9	Thermodynamics Coupled with Hydrodynamics for Multiphase Flows.....	42
4.9.1	Heat Transfer Coupled with Hydrodynamics	43
4.9.2	Computational Procedure for Phase Change Implementation	44
5	Results.....	45
5.1	FSI Validation.....	45
5.1.1	Circular Obstruction, No Convection	46
5.1.2	No Obstruction, Forced Convection	50
5.1.3	Square and Circular Obstruction, Forced Convection	52
5.2	Stefan Problem Validation.....	57
5.2.1	1D Solidification.....	57
5.2.2	Infinite Corner Solidification.....	59
5.2.3	Frank Sphere.....	61
5.3	Coupled Stefan and Hydrodynamics Validation	63
5.3.1	Flow over Cylinder	63
5.3.2	Solidification with Natural Convection	64
5.3.3	Tin Melting with Non-constant Density	65
5.3.4	Ice Cylinder Melting in High Re Flow.....	68
6	Conclusion.....	74
6.1	Future Work	75
7	References	77

1 Introduction

1.1 Research Motivation

As of the late 20th century, the modeling of supercooled large droplets (SLD) has become a vital part of ensuring that modern-day airplanes and helicopters are safe to fly in frigid conditions. SLD are droplets of diameters ranging from 50-1000 μm , which are much larger than droplets previously considered in Appendix C [1] of the Federal Aviation Administration (FAA). This has led to the introduction of Appendix O [2] explicitly addressing SLD for aircraft certification. SLD are particularly dangerous as their large size leads to break-up or coalescence before impact, spreading and splashing during impact, and rebounding after impact [3], causing ice to possibly accrete past the ice protection systems extent [4]. This may result in the aircraft experiencing a decrease in lift, unfavorable stall characteristics or roll control problems [5].

The reproduction of SLD in horizontal icing tunnels can be challenging, as they may break up or settle before the test section [6]. While vertical wind tunnels are preferable since they can eliminate droplets settling at their base [6], some have test sections mounted on rotating flywheels, leading to additional Coriolis and centrifugal effects not present in flight [7]. Moreover, surface impingement is difficult to measure in a non-invasive manner, making the numerical simulation of SLD impingement a more feasible approach [8]. Furthermore, unlike experiments, numerical SLD modeling has no scaling issues.

FENSAP-ICE [9] and LEWICE [10] are two commercial codes that are able to simulate SLD effects. The numerical modeling in these solvers is macroscopic and treats an ensemble of droplets, which still relies on some empirical data and correlations. Therefore, taking a microscopic approach and accurately simulating the physics of individual droplets can lead to higher fidelity models when replacing empirical data. Physically and geometrically modeling a single droplet's phase change and the fluid-structure interaction (FSI) at the water-ice interface is complex and normally tackled with either meshless methods or immersed boundary (IB). Meshless techniques such as smooth particle hydrodynamics (SPH) [11] are Lagrangian approaches, as opposed to IB Eulerian approaches such as XFEM [12]. Both methods avoid the need for a body-conforming mesh, which would be computationally prohibitive when modeling SLD.

For mesh-based approaches, it is important to distinguish between body-conforming and immersed boundary methods (IBM). The former requires *a priori* knowledge of the phase change interface in order to keep it aligned with the element edges. Furthermore, while the governing equations could be solved separately in such body-conforming mesh approaches, they would require re-meshing or mesh deformation with an ensuing interpolation that may cause a loss of accuracy. Alternately, IBMs can handle large topological changes and complex boundaries [13] through the application of appropriate forcing on a regular Cartesian mesh. IBMs include direct forcing [14], virtual boundary [15], ghost-cell and cut-cell methods [16], as well as XFEM [17]. These will be discussed in more detail within the thesis to justify the selection of an XFEM implementation for the multiphase flow solver.

An important requirement from an IBM is that it must be able to handle discontinuities within the velocity, pressure and temperature fields. The inability to deal with jumps in properties in elements causes difficulty in the Finite Element Method (FEM) [18, 19]. The need to solve this dilemma has led to the development of XFEM [17], which, combined with LSM, can be used to simulate free boundaries. This thesis will apply such XFEM-LSM to model phase change and impose special enrichment functions to account for discontinuities.

Simulation of the solidification/melting part of the present problem can be done by several approaches, such as the phase field [20], effective heat capacity [21], and enthalpy methods [22]. The latter is often used because it accounts for latent heat absorption or release and requires no interface tracking or capture. However, by not requiring the imposition of the strong discontinuity due to the thermal interface condition, the enthalpy method creates a mushy zone for the phase change at the interface [22]. It is thus proposed in this thesis that a XFEM-LSM combination may be a better alternative, as LSM can capture a sharp interface by constructing enrichment functions.

XFEM methods have been used to model FSI problems and phase change flows. For example, Gerstenberger *et al.* [23] formulated a Lagrange-multiplier approach that utilized an extended Eulerian field for the fluid domain and a Lagrangian field for the structure to simulate thin and bulky solids [24]. His method of coupling the fluid and structural fields was further developed in [25] to solve heat conduction between concentric cylinder surfaces. The XFEM-LSM combined framework was at first limited to solving the Stefan problem [26] until coupled with

hydrodynamics and accounting for the subsequent melt flow on dendritic solidification [27]. Zabaras *et al.* [27] further introduced a volume-averaged continuity and momentum equations but disregarded the density differences between phases as well as the buoyancy effects induced by the temperature gradient. Stapor [28] considered the density difference in driving the melt flow but made no hydrodynamic calculation. The final addition of the hydrodynamic calculation with buoyancy was applied in Martin *et al.* [29, 30], but the methodology made no enrichment in the approximation of the velocity and pressure fields. It was not until Li *et al.* [31] that XFEM with LSM coupled the Stefan and hydrodynamic problems and considered non-constant density phase changes and buoyancy effects. However, to the author's knowledge, there is no full Navier-Stokes implementation of the coupled problem that is able to simulate phase change at high Reynolds numbers.

1.2 Thesis Outline and Contributions

The goal of this research is to introduce FSI and solidification into a multiphase solver for the purpose of modeling individual SLD impingement and freezing. Due to the proprietary nature of SLD experiments, there is insufficient information regarding SLD impingement and solidification and experimental data available in the open literature is scarce. The objective is then to model SLD hitting a cold surface and freezing, by first developing a methodology that can handle FSI. The present framework focuses on simulating fluid-fluid and solid-fluid interfaces. It also aims to model the planar solidification of SLD by solving the Stefan problem and then loosely-coupling the hydrodynamics and thermodynamics to simulate fluid melt. Thus, the present thesis can be seen as a numerical experiment to extract more physics-based models for SLD simulations and replace empirical ones.

A comprehensive literature review detailed in the next chapter discusses the process of solidification in droplets and the differences between approaches used in the Stefan problem and FSI. Chapter 3 goes over the mathematics behind the present methodology while chapter 4 covers the techniques that have been employed in implementing FSI and solidification into the multiphase flow solver. Case studies that cover validation and convergence results are presented in chapter 5. The thesis conclusion and recommendations for further exploration are in chapter 6.

In summary, the present thesis presents a comprehensive way of solving high Reynolds phase change problems, by:

1. Proposing a mathematical framework for modeling FSI and solidification for a multiphase flow solver using XFEM with LSM;
2. Using XFEM-LSM with penalization to model FSI as well as fluid-fluid interactions, and the Stefan condition to account for planar solidification;
3. Assessing the methodology using analytical and numerical validation test cases.

2 Background and Literature Review

2.1 Solidification Phenomena in SLD

Ice accretion results from the impact of water droplets on a subfreezing temperature surface which rapidly cools the water drop and freezes it to the surface. However, if the liquid is already supercooled, then the freezing process that results is unstable and consists of ice nucleation followed by a propagation of dendrites throughout the drop. Lastly, the remaining liquid in the drop undergoes slower solidification, characterized by the planar Stefan problem. The typical freezing profile of water with supercooling is shown in Figure 2-1.

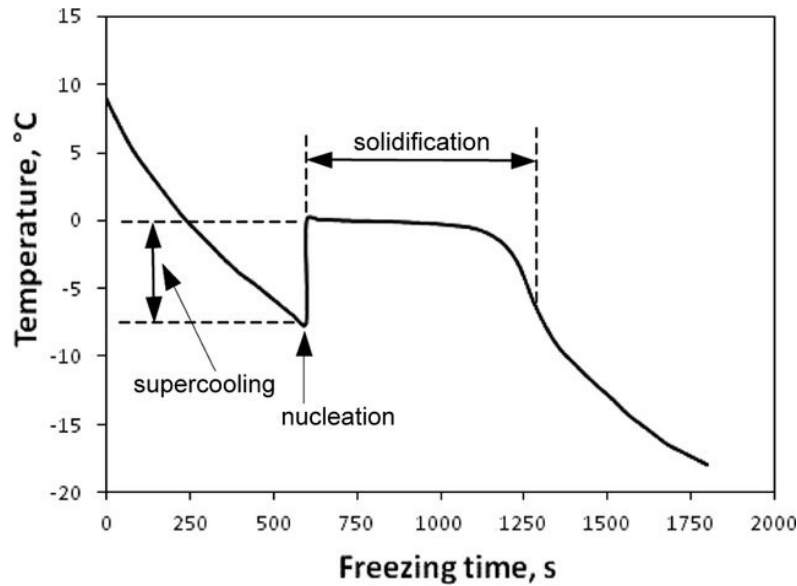


Figure 2-1 Freezing profile of water as a function of freezing time [32]

Nucleation and dendrite propagation are physical mechanisms that are complex to model numerically. Nucleation is a spontaneous phenomenon that occurs in SLD when they surpass a critical size. Moreover, it is dependent on the spatial and temporal variations of the liquid phase temperature and density [33], which makes it a stochastic process. The effect of drop impact on the nucleation rate and the delay in freezing is not yet understood, unlike the spreading kinetics of a drop on a non-freezing surface.

The first stage of solidification is the heterogeneous nucleation and spreading of a thin ice layer. The random nature of nucleation was presented in [34] where numerous impact experiments showed that the nucleation process was heterogeneous. Furthermore, the experiment revealed that the moment of nucleation and subsequent freezing determines the final iced area. Figure 2-2 shows a schematic of the three kinds of freezing processes as a result of three different nucleation times [35].

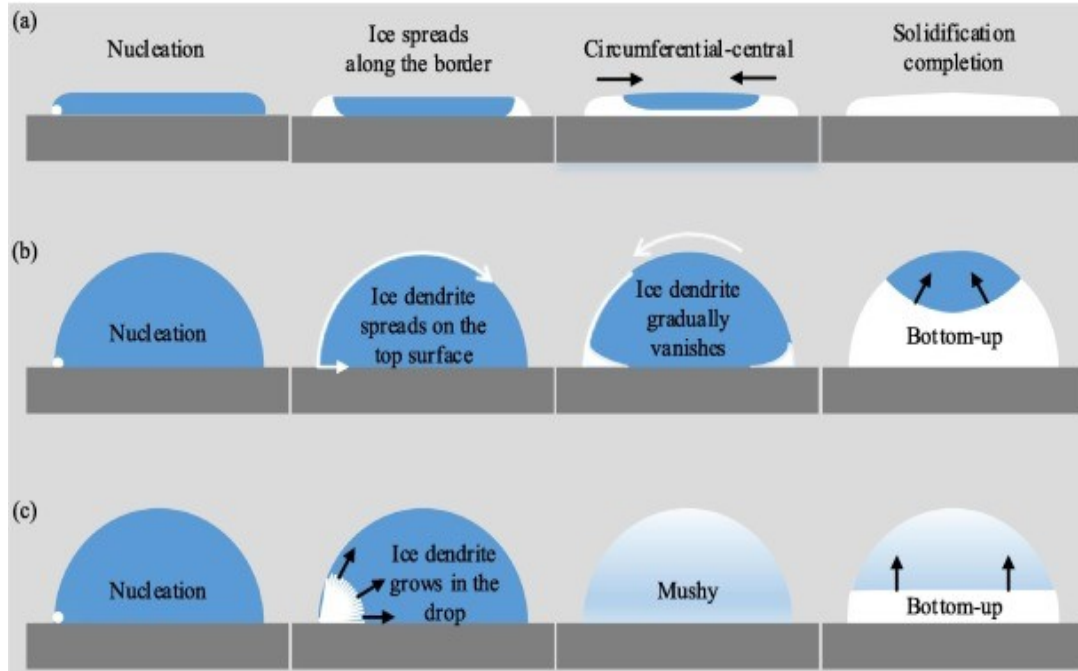


Figure 2-2 Schematic diagram for water droplet freezing on impact. (a) $t_{nuc} < 30 \text{ ms}$, (b) $30 \text{ ms} \leq t_{nuc} \leq 600 \text{ ms}$, (c) $t_{nuc} > 600 \text{ ms}$ which is similar to supercooled water nucleation time [35]

Additionally, the surface temperature implicitly influences the freezing rate of the drop, leading to an increase in the contact area and time. Consequently, SLD have a higher number of nucleation sites per unit area than any other water drops that experience solidification. Nucleation is seen in Figure 2-3 for a droplet at -15.6°C .

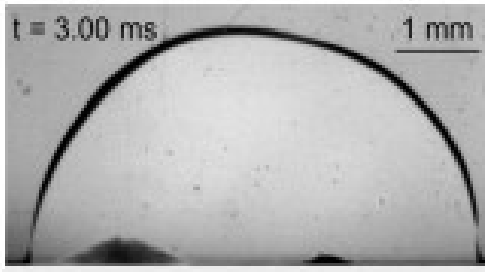


Figure 2-3 Nucleation in a water drop [36]

The spreading of the thin ice layer is rapid and tangential to the substrate, beginning from the nucleation sites. This spreading speed is determined by the supercooling present as the water drop hits the subcooled surface. The temperature drop experienced by the liquid or gas below its freezing point without it becoming a solid, known as supercooling, is characterized by the material

properties of the solid phase [37]. A temperature variation of 2.6 K in [37] and 4.7 K in [34] was found to be the supercooling threshold, also known as the point where the surface of the ice layer becomes unstable and dendrites start forming into the bulk liquid. This initiates dendrite propagation, the second stage of solidification, for which the higher the supercooling, the closer the ice layer tip is to the position of the first instability in the ice layer. However, if the supercooling threshold is not met, then planar solidification begins without dendrite formation.

The second stage of solidification consists of the appearance of dendrites within the freezing water droplet. The density of these dendrites increases with increasing supercooling until the droplet consists of a lattice of dendrites. Dendrite formation can be seen in Figure 2-4. Throughout this process, latent heat has been released to the point where the water/ice mixture has reached thermodynamic equilibrium at melting temperature. Further removal of heat results in the stable freezing of the remaining water and begins the last stage of solidification.

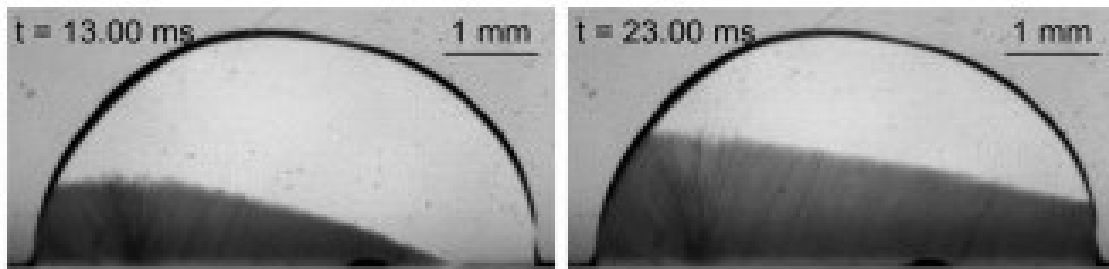


Figure 2-4 Dendritic freezing in a water drop [36]

The final stage is the slower solidification of the bulk liquid at the melting temperature. This stage is known as planar solidification where the stable freezing front moves in the opposite direction from that of the applied heat flux. The thesis will focus on modeling planar solidification since it is the type of solidification observed in both non-SLD and SLD water droplets and has the longest duration in SLD. Planar solidification is shown in Figure 2-5.

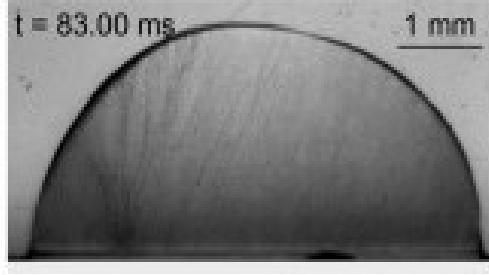


Figure 2-5 Planar solidification in a water drop [36]

Another difficulty that arises when modeling SLD is the influence the impact surface has on the SLD freezing response time. For example, solidification would occur instantaneously if the impact surface was covered in ice, whereas a delay would be observed on a dry or wetted surface [34]. An investigation of the impact and solidification of water drops on the iced surface at room temperature has been carried out in [38]. However, no experiments were designed to investigate the behavior of a single SLD on an iced surface. In [34], the authors found that only ice causes immediate freezing when brought into contact with SLD. They believe that it is due to the fact that the water molecules attach to the existing surface pass into the stable state, and they note that this ability to trigger solidification is independent of liquid temperature [34].

Before one can model planar solidification, the ability to model multi-phase flow with FSI must be considered. Modeling multiphase flows, especially for droplets that can become complex geometric shapes, must be done in a computationally inexpensive way while also providing accurate results. This is explored in the subsequent section.

2.2 Body-Conforming versus IBM

IBM was developed Charles Peskin developed to simulate FSI for heart physiological applications [14]. The distinctiveness of IBM is its treatment of fluid(s) and structures/solids by Eulerian and Lagrangian coordinates, respectively. A variety of approaches were based on Peskin's IBM after its aptitude in simulating flow over complicated immersed bodies was demonstrated. These approaches include the virtual boundary method [15], the ghost-cell method [39] and the cut-cell method [16]. They can be classified as belonging to one of the two following categories based on the implementation of the force term: continuous forcing and discrete forcing methods [40].

Proceeding with this classification, several IBMs are briefly introduced in the following paragraphs.

2.2.1 Continuous Forcing

In the continuous forcing approaches, the Navier-Stokes (NS) equations are augmented with a force term before discretization. This leads to a diffused interface, approximating the free boundary not as a sharp line but as a small region. Continuous forcing approaches are relatively easy to implement in the NS equations. However, a sharp representation of the boundary cannot be obtained due to the smoothing of the forcing function. They are thus not used for high Reynolds (Re) number flows [40]. Another limitation is that they require the solution of the governing equations throughout the entire domain, which is also inside the immersed body. Hence, as Re is increased, more grid points are required, and this is detrimental to the computational performance of the method. Continuous forcing IBMs include the elastic boundaries IBM, rigid boundaries IBM and distributed Lagrange multiplier IBM [40] which are briefly introduced in the following paragraphs.

Elastic Boundaries IBM

The original IBM developed by Peskin [14] to simulate flow patterns around heart valves, has become known as elastic boundaries IBM. It is a mixed Eulerian-Lagrangian finite difference method consisting of an IB that is defined using massless elastic fibers with tracking done by a collection of massless points [14]. This later became known as elastic boundaries IBM due to the definition of an elastic boundary through the massless points. Peskin first defined a force density using a Dirac delta function. However, the Dirac delta formulation resulted in fibers that did not coincide with the Cartesian grid, which increased the computational complexity. Peskin later replaced the Dirac delta function by a smooth distribution function as the latter is more suitable for discrete meshes. Further improvements have been made to the original IBM formulation, see [41].

Rigid Boundaries IBM

Rigid boundaries IBM includes the virtual boundary method developed by Goldstein *et al.* [42] and the penalty method by Khadra *et al.* [43]. The virtual boundary method uses a boundary which

applies a force on the fluid so that the fluid is stationary at the interface. However, since the body force is not known beforehand, it must be computed and fed back into the system repeatedly, in a feedback loop. This feedback force formulation is capable of handling solid boundaries and moving boundaries. Unfortunately, the feedback force is generally multiplied by a Gaussian distribution that produces smearing of the surface boundary. Defining user-specified parameters is an added limitation when working with rigid boundaries versus elastic boundaries. Furthermore, feedback forcing can induce spurious oscillations and restrict the computational time step due to numerical stability [44]. This is addressed by Saiki *et al.* [15] by using an area-weighted average function.

On the other hand, the penalty method by Khadra *et al.* [43] assumes a porous medium and uses the Navier-Stokes-Brinkman equations to solve for the IB. The penalty term is the permeability of the medium which is zero for the fluid and infinity for the solid. This allows the velocity field to be effectively zero in the solid [43]. However, the addition of another term, referred to as the Darcy drag, into the governing equations increases the problem complexity. Furthermore, as was the case in continuous forcing methods, mass conservation is not explicitly enforced.

Distributed Lagrangian Multiplier

The distributed Lagrange multiplier IBM was proposed by Glowinski *et al.* [45]. The idea was to use a predictor-corrector approach and have the fluid velocity approximated using the momentum equations. This would then correct the velocity using the incompressibility condition with Lagrange multipliers to satisfy the no-slip condition. An advantage of this method is the ability to simulate moving boundaries whereas the other continuous forcing methods do not. The other continuous forcing methods also have more severe time step restrictions. Nevertheless, like continuous forcing methods, the method is more suited to low *Re* applications [40].

2.2.2 Direct Forcing

Direct forcing methods use a forcing term that acts as a velocity corrector for grid points inside the IB. In comparison to continuous forcing methods, direct forcing depend heavily on the discretization since the equation is first discretized and then the force term is added. However, this allows for control over numerical accuracy, stability and conservation properties making direct

forcing more favorable than continuous forcing methods. Additionally, direct forcing methods are limited by a finite error which results from the method not enforcing velocity for the interface cells [40]. The ghost-cell, ghost-fluid, and cut-cell methods are extensions on the direct forcing method and their approaches are detailed in the following paragraphs.

Ghost-Cell Method

In the ghost-cell method developed by Tseng [39], the boundary condition on the IB is implicitly set by using an interpolation scheme that is linear in the tangential direction and quadratic in the normal direction. This approach attempts to achieve a higher-order representation of the IB than the other methods by using a ghost zone inside the body. However, the ghost-cell method introduces a fictitious velocity field in the continuity equation which leads to a slower convergence rate over the boundary. Moreover, this method requires additional storage since it uses a staggered grid, though this additional storage would be small if the IB is of a lower-dimensional than the rest of the domain [40]. Another major limitation of the ghost-cell method is that large negative weighting coefficients arise when the boundary point is close to the fluid nodes [39]. Since these coefficients are used in extrapolation, they cause numerical instability.

A few approaches can be used to improve the numerical stability of the ghost-cell method. One of these approaches uses the image of the ghost node inside the flow domain to get positive weighting coefficients [46]. The other approach consists in modifying the piecewise linear boundary [47].

Ghost-Fluid Method

The ghost-fluid method uses a ghost (artificial) fluid to capture the interface. Interface-capturing methods were developed for free-surface and two-fluid flows, and do not require mesh deformation as interface-tracking methods do. The ghost-fluid method is commonly used in surface flows. Each grid point in the method contains double the information as it contains the mass, momentum, and energy for the real fluid as well as ghost quantities for the artificial fluid [48]. However, unlike the ghost-cell method, the ghost-fluid method uses interpolation along the tangential direction. Therefore, imposing Neumann boundary conditions becomes difficult, since the normal component usually contains the boundary information that is important to translate the IB [48].

Cut-Cell Methods

Cut-cell IBM does not use momentum forcing; instead, the cells “cut” by the IB are reshaped by removing the volumes that are inside the solid [16]. Generally, cut-cell methods utilize cell-merging to improve the quality of the mesh near the interface. However, this gives rise to several issues including an increase in complexity while computing fluxes, the formation of complex polyhedral cells in 3D, and large condition numbers [40]. To overcome these limitations, cell-linking can be used. It uses a "master/worker" pair where each cell remains a distinct entity, thus avoiding the issues of cell-merging [40]. Overall, the cut-cell method generally increases the complexity of calculation, since it requires the computation of fluxes between adjacent cells. Furthermore, small cell/control volumes often arise, resulting in stability problems and slow convergence.

2.3 XFEM

Originally developed for the simulation of cracks and discontinuities in structures by Belytschko *et al.* [12], XFEM was later extended in [49] to two-phase flow problems and Stokes flow with rigid particle interactions. It is a technique that is based on the generalized finite element method (GEM), also known simply as FEM, and the partition of unity method (PUM). The principle behind XFEM is to use enriched finite elements in the approximation space to reproduce challenging features, such as discontinuities. When comparing XFEM with the FEM approach, XFEM does not require a body-conforming mesh, thus avoiding the need to update the computational mesh. The following section will elaborate on PUM, as well as outlining the properties of XFEM.

2.3.1 Partition of Unity

The Partition of Unity Method (PUM) uses special enrichment functions that allow for arbitrary discontinuities to be treated on a fixed mesh. The essential component of using PUM is extrinsically enriching the mesh. The difference between “intrinsic” enrichment and “extrinsic” enrichment is that intrinsic enrichment enriches the basic vector while extrinsic enrichment enriches the approximation.

PUM uses a collection of global functions, $f_i(x)$, whose value sums to unity at each point in the solution domain. The finite element (FE) approximation of the enriched domain is then [50]:

$$u(x) = \sum_{i=1}^N N_i(x) \bar{u}_i + \sum_{i=1}^N N_i(x) \sum_{j=1}^M p_j \bar{a}_{ij} \quad (2.1)$$

where \bar{u}_i is the standard nodal DOF related to the basis $N_i(x)$, \bar{a}_{ij} is the enhanced DOF related to the basis $p_j(x)$, and M is the number of enrichment functions for node i . The first term is the “standard” FE formulation while the second term refers to the “enriched” formulation. XFEM uses the same FE extrinsic enrichment but only enriches regions close to the interface, thus reducing required storage and computational time when compared to PUM which enriches the entire domain.

2.3.2 XFEM Formulation

In XFEM, special functions that depend on the discontinuity are introduced in the FE space “extending” the FE formulation to be able to resolve the discontinuities. These are called enrichment functions and can be signed distance, level-set, branch, or Heaviside jump functions [50]. In general, ramp functions with a signed distance component are used for weak discontinuities, a common case being in bi-materials or two-phase flow. Conversely, Heaviside jump functions are used for strong discontinuities, such as cracks in materials. XFEM enriches elements “cut” by an interface, as shown in Figure 1. XFEM may also require “blending” or “partially enriched” elements, elements that no longer satisfy the Partition of Unity (PU). This is a side effect of node sharing between elements in XFEM. Due to the “partially enriched” elements, the definition of completeness for PUM cannot be satisfied since [50]:

$$\sum N_j(x) \neq 1 \rightarrow \text{PU condition not met} \quad (2.2)$$

$$\sum N_j(x) \varphi(x_j) \neq \varphi(x) \rightarrow \varphi(x) \text{ cannot be recovered} \quad (2.3)$$

where the enriched shape function is N_j and the enrichment function is $\varphi(x)$.

Blending elements can introduce spurious terms and increase the interpolation error. This can only be corrected if the standard element shape function is of greater or equal order to the enriched shape function [50].

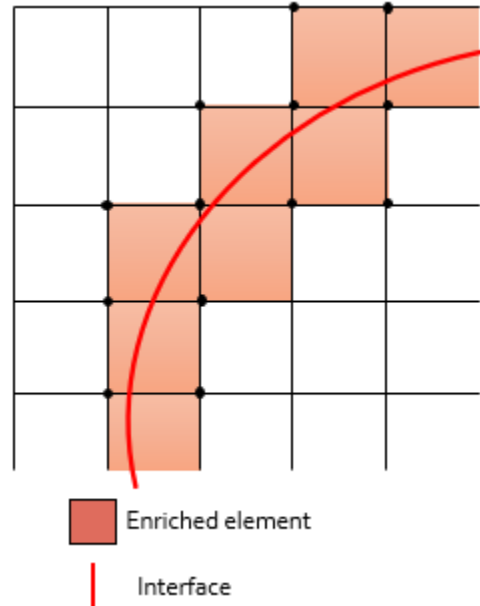


Figure 2-6 Enriched elements

Blending elements also have the disadvantage of resulting in lower convergence rates in XFEM. For the case of weak discontinuities or bi-material discontinuities, interpolation results in an increase in the computational error from $O(h^2)$ to $O(h)$ [50]. In the case of higher-order polynomials, the interpolation error is even greater. The advantage of the Heaviside enrichment function is that it has values that vanish in the blending elements, thereby the error of interpolation remains the same as the original FEM formulation.

Several remedies have been proposed to address issues arising from blending elements around weak discontinuities. Chessa [49] recommended hierarchal shape functions to compensate for parasitic terms. These hierarchal shape functions are simply shape functions of different order polynomials than the standard and enriched elements, with the order of the standard shape function of a higher order than that of the enriched. Fries [51] modified the enrichment functions in the standard elements, leaving unchanged those that are fully enriched while varying the enrichment functions continuously in the elements. Gracie [52] used a discontinuous Galerkin decomposition

of the domain with continuity between the enriched and unenriched parts done with patches, which used an internal penalty parameter to enforce them. Another limitation arises from using non-smooth enriched shape functions which prevents the use of standard Gauss quadrature rules in elements crossed by a discontinuity. These elements are thus split into conforming triangular/quadrilateral sub-elements or non-conforming rectangular sub-grid partitions [50]. Triangular partitioning is more accurate than rectangular sub-grid partitioning because triangles lead to smooth subdomains.

In the area of FSI, Gerstenberger *et al.* [24] simulated the deformation of thin and bulky structures. The paper found that XFEM would be able to reproduce the key features required in modeling such large deformations. They [24] also studied the flow field around a flexible rotating cylinder, a problem similar to the two-phase flow problem of a water droplet moving in air. Later the findings were extended to 3D and used to simulate heat conduction in FSI [25]. Sauerland *et al.* [53] used XFEM to conduct a systematic study of two-phase flows with the author extrapolating results to free flows. Additionally, the research also considered surface tension effects in two-phase flows. In the following section, the review will look at literature that focuses on heat transfer with phase change done with XFEM.

2.4 Heat Transfer Problems - Solidification/Melting

In the 1890s, Josef Stefan introduced a Boundary Value Problem (BVP) to investigate heat transfer with phase change [54]. The Stefan problem solves the heat equation with a boundary condition, called the Stefan condition, which allows for the underlying partial differential equation (PDE) to be valid at phase change interfaces. The Stefan condition, which provides closure for the BVP, can be rearranged to solve for the normal speed of the boundary.

The extension of the multiphase flow solver will aim to simulate solidification using the Stefan condition to model phase change as well as heat transfer by solving the temperature-based energy equation. The Stefan problem will thus be used to validate the phase change model implementation within the current flow solver.

2.4.1 Common Methods of Solving Stefan Problem

There are several methods used in literature to solve the Stefan problem, including moving mesh methods, enthalpy method, XFEM, phase field method, and effective heat capacity. The first three will be presented in the subsequent paragraphs.

Moving Mesh / Mesh-Deformation Methods

Moving mesh / mesh-deformation methods involves updating the mesh so it conforms to the interface. The two phases are then solved separately with the energy equation and the melting temperature being imposed at the interface. This method is quite costly when it comes to dealing with an interface with a complex shape.

Enthalpy Methods

The enthalpy method [22] is a simple and robust method that is commonly used to solve Stefan problems. It uses an effective heat capacitance to account for the latent heat absorption/release at the interface. By doing so, it removes the complexity arising when explicitly enforcing the interface temperature boundary condition. The enthalpy method also allows for the position of the interface to not be tracked explicitly since the energy equation is the same for both phases. However, this means that there is a “mushy” zone because the interface temperature is not strictly enforced, and a special treatment is required to minimize oscillations in temperature.

XFEM

XFEM is a numerical method that enables a local enrichment of approximation spaces using PUM. It allows for the retention of the desirable aspects of both the mesh deforming method and the enthalpy method since it does not require re-meshing nor discontinuous material parameters. XFEM allows for a sharp interface since the enrichment function used will prevent the “mushy” zone generally present with the enthalpy method. Thus, XFEM will be used to implement the Stefan condition and simulate the phase change problem for planar solidification.

3 Mathematical Models

This section outlines the mathematical models that are used: LSM, INS equations, temperature-based energy equation, and Stefan problem. In the present study, the phase change process of melting/solidification will be confined to a computational domain Ω that is divided by a sharp interface Γ_I into a liquid region Ω_l and a solid region Ω_s . The subscripts s and l will denote the solid and liquid side, respectively.

3.1 Heat Transfer

The temperature-based energy equation, with both convection and conduction terms, is defined as:

$$\rho c_p \frac{\partial T}{\partial t} + \rho c_p u_i \frac{\partial T}{\partial x_j} - \frac{\partial}{\partial x_j} \left(k \left(\frac{\partial T}{\partial x_j} + \frac{\partial T}{\partial x_i} \right) \right) = 0; \vec{x} \in \Omega \quad (3.1)$$

$$T = T_m; \vec{x} \in \Gamma \quad (3.2)$$

where ρ is the density, c_p is the specific heat, u_i is the velocity field, k is the thermal conductivity, and T_m is the melting temperature. The velocity field in the solid is zero, so u_i only applies to the fluid domain.

In the case of the Stefan problem, the advection term is absent from the temperature-based energy equation and the latter can be written as:

$$\rho c_p \frac{\partial T}{\partial t} - \frac{\partial}{\partial x_j} \left(k \left(\frac{\partial T}{\partial x_j} + \frac{\partial T}{\partial x_i} \right) \right) = 0; \vec{x} \in \Omega \quad (3.3)$$

$$T = T_m; \vec{x} \in \Gamma \quad (3.4)$$

The phase change can be expressed by the Stefan condition since phase change comes with either absorption or release of latent heat at the interface.

$$[[q]] = \rho_s L V_I; \vec{x} \in \Gamma \quad (3.5)$$

$$[[q]] = k_s \left(\frac{\partial T}{\partial n} \right)_s - k_l \left(\frac{\partial T}{\partial n} \right)_l; \vec{x} \in \Gamma \quad (3.6)$$

where L represents the latent heat, V_I is the speed of the interface and $[[q]]$ is the heat flux jump. The latter serves as the driving force that moves the interface as phase change occurs. The accurate evaluation of the heat flux jump is important in obtaining a correct evaluation of the interface profile.

3.1.1 Heat Flux Jump Evaluation

The heat flux jump evaluation is a crucial part of the solidification model developed in this thesis. An incorrect heat flux evaluation would result in an incorrect interface speed, thus the progression of the phase change expressed in the motion of the free-boundary interface would be wrong as well.

The appropriate evaluation of the heat flux also means avoiding small numerical oscillations in the temperature field that leads to the wrong interface profile [55]. The present method uses an evaluation done by using the slope of a line built from two sample points on either side of the interface, in the vicinity of the interface, to approximate the temperature at the interface. The heat flux evaluation will be explained in more detail in the Numerical Modeling section.

3.2 Hydrodynamics

As phase change takes place, the melting/freezing will cause motion in the fluid driven by one of two forces: the density jump at the interface or the buoyancy force due to the temperature gradients. The fluid motion can be described by the INS equations with the Boussinesq approximation written in the primitive form as:

$$\frac{\partial u_i}{\partial x_i} = 0; \vec{x} \in \Omega \quad (3.7)$$

$$\rho \frac{\partial u_i}{\partial t} + \rho u_j \frac{\partial u_i}{\partial x_j} - \frac{\partial}{\partial x_j} \left(\mu \left(\frac{\partial u_i}{\partial x_j} + \frac{\partial u_j}{\partial x_i} \right) \right) + \frac{\partial P}{\partial x_i} - \rho \alpha (T - T_{ref}) g_i; \vec{x} \in \Omega \quad (3.8)$$

where μ is the fluid dynamic viscosity, P is the pressure, T is the temperature, T_{ref} is the reference temperature, g_i is the gravitational acceleration, and α is the thermal expansion coefficient.

On the phase change interface, the following condition applies:

$$u_i = u_l = \left(1 - \frac{\rho_s}{\rho_l}\right) V_l \vec{n}_\Gamma; \vec{x} \in \Gamma \quad (3.9)$$

Stating that melt/solidification velocity is present at the interface, with a no-slip boundary condition. The mass conservation law implies that $u_l = \left(1 - \frac{\rho_s}{\rho_l}\right) V_l \vec{n}_\Gamma$, otherwise, if there was no density jump then the interface velocity would be zero.

3.3 Interface Capture

The method that has been employed is a fixed mesh Eulerian approach necessitating an interface capturing method. Interface tracking methods require the mesh to be updated as the flow moves through the domain, while interface capturing methods use the resolution of the finite element mesh to compute the location of the interface, thereby “capturing” its location.

3.3.1 Level Set Function and Advection

The LSM function is initially defined as the signed distance function (SDF) shown below [56]:

$$\phi = \text{sign}((\vec{x} - \vec{x}_l) \cdot \vec{n}_\Gamma) \text{Min}\|\vec{x} - \vec{x}_l\|; \vec{x} \in \Omega \quad (3.10)$$

The LSM advection equation that governs the update of ϕ is defined as:

$$\frac{\partial \phi}{\partial t} + F\|\nabla \phi\| = \frac{\partial \phi}{\partial t} + u_i \cdot \nabla \phi = 0; \vec{x} \in \Omega \quad (3.11)$$

This is because $F = u_i \cdot \vec{n}_\Gamma = u_i \cdot \frac{\nabla \phi}{\|\nabla \phi\|}$.

3.3.2 Interface Speed Extension

The interface speed extension $F(x)$ can be defined by spreading the interface speed over Ω with the partial differential below:

$$\text{sign}(\phi)\nabla\phi \cdot \nabla F = 0; \vec{x} \in \Omega \quad (3.12)$$

$$F(x) = V_I; \vec{x} \in \Gamma \quad (3.13)$$

4 Numerical Modeling

The following section outlines the numerical modeling used: the hybrid Taylor-Galerkin Variational Multiscale stabilization for the level set advection and XFEM stabilized by Galerkin Least-Squares for FSI and phase change. The chapter addresses the discretization that has been used for the INS equations and the temperature-based energy equation, as well as the procedure that has been utilized to simulate solidification/melting.

4.1 FSI

There are two main approaches that can be employed to implement FSI within a flow solver: a monolithic or a partitioned approach. The former involves solving the governing equations of the flow and the structure's displacement simultaneously, within one solver. The latter uses two solvers, one handling the flow while the other dealing with the displacement of the solid/structure. Some of the common methods of capturing the interaction between fluid and structure are the Arbitrary Lagrangian-Eulerian, fictitious domain, Lagrange multiplier, and Brinkman penalization methods.

4.1.1 Arbitrary Lagrangian-Eulerian Method

The Arbitrary Lagrangian-Eulerian (ALE) method allows for random motion of grid points with respect to their frame of reference according to the convection of the flow. This approach is easy to implement and has a relatively low computational cost. However, for large translations and rotations, the fluid elements can become ill-shaped and decrease the accuracy of the solution. The solution would thus require remeshing and the subsequent interpolation would result in a loss of accuracy.

4.1.2 Fictitious Domain

The fictitious domain method uses a distributed Lagrange multiplier to constrain the fluid and structure at the interface and extending the influence of the multiplier to the rest of the domain. This is slightly different than the IBM used by Peskin where the solid boundary interacts with the fluid via body forces applied to the interface points. These body forces impose a constraint so that the velocity at each of the interface points is coupled to the fluid velocity. The fictitious domain method permits the use of structured meshes on a simple auxiliary/fictitious domain that similarly contains the actual domain, allowing for use of fast solvers on complex geometry problems [43].

4.1.3 Lagrange Multiplier

The Lagrange multiplier method can also simulate a fluid/structure boundary with the addition of a second variable, Λ , as the interface constraint. This technique requires more computational effort than ALE, fictitious domain and penalty method. In addition, the use of the wrong Lagrangian multiplier space can lead to oscillations in flux values as well as a degeneration of the solution.

The Lagrange multiplier method, when applied to the steady-state diffusion equation, is expressed as:

$$\int_{\Omega} \nabla \delta u \nabla u \, d\Omega - \int_{\Omega} \delta u \Lambda \, d\Omega = 0 \quad (4.1)$$

$$\int_{\Omega} \Delta \lambda (u - \bar{U}) \, d\Omega = 0 \quad (4.2)$$

4.1.4 Brinkman Penalization/Penalty Method

The penalty method works by applying the interface boundary condition, i.e., the imposed condition between the solid and fluid, using the multiplication of the residual form of the constraint with a large penalization parameter β . This residual expression is then placed into the weak form of the finite element formulation. The penalty method is expressed as:

$$f_{pen} = \int_{\Omega} \delta u \beta(u - \bar{u}) d\Omega \quad (4.3)$$

This approach is accurate and easy to implement in comparison to the other approaches mentioned. The penalty method was implemented into the INS and temperature-based energy equations.

4.2 INS Equations

The XFEM solver uses the INS equations written as:

$$\frac{\partial u_i}{\partial x_i} = 0 \quad (4.4)$$

$$\rho \frac{\partial u_i}{\partial t} + \rho u_j \left(\frac{\partial u_i}{\partial x_j} \right) - \mu \frac{\partial}{\partial x_j} \left(\frac{\partial u_i}{\partial x_j} + \frac{\partial u_j}{\partial x_i} \right) + \frac{\partial P}{\partial x_i} - \rho F_i = 0 \quad (4.5)$$

The weak Galerkin form of the INS equations is:

$$\sum_{e=1}^{n_{elem}} \int_{\Omega_e} q \left(\frac{\partial u_i}{\partial x_i} \right) d\Omega_e = 0 \quad (4.6)$$

$$\sum_{e=1}^{n_{elem}} \int_{\Omega_e} w \left(\rho \frac{\partial u_i}{\partial t} + \rho u_j \left(\frac{\partial u_i}{\partial x_j} \right) - \mu \frac{\partial}{\partial x_j} \left(\frac{\partial u_i}{\partial x_j} + \frac{\partial u_j}{\partial x_i} \right) + \frac{\partial P}{\partial x_i} - \rho F_i \right) d\Omega_e = 0 \quad (4.7)$$

The nonlinear advection term $\rho u_j \left(\frac{\partial u_i}{\partial x_j} \right)$ is linearized using a fixed-point iteration method such that:

$$\rho u_j \left(\frac{\partial u_i}{\partial x_j} \right) \sim \rho a_j \left(\frac{\partial u_i}{\partial x_j} \right) \quad (4.8)$$

4.2.1 Galerkin Least Squares

The Galerkin Least Squares (GLS) method uses a mesh-dependent term obtained from the least-squares form of the gradient of the Euler-Lagrange equation in addition to the standard Galerkin method. The additional term helps with the stability issues that the standard finite element approach has in advection-dominated problems resulting from the resemblance to a central

differencing scheme. The addition of the least-square form enhances stability without decreasing the accuracy or consistency. This method is used in the discretization of the INS equations and the temperature-based energy equation.

GLS for INS Equations

The final form of the GLS stabilized INS equations with penalization is as follows:

$$\sum_{e=1}^{n_{elem}} \int_{\Omega_e} \left(w \frac{\partial u_i}{\partial x_i} + \frac{\partial w}{\partial x_i} [\tau \mathbf{g}(x_i)] \right) d\Omega_e = 0 \quad (4.9)$$

$$\begin{aligned} & \sum_{e=1}^{n_{elem}} \int_{\Omega_e} w_i \left(\rho \frac{\partial u_i}{\partial t} + \rho a_j \frac{\partial u_i}{\partial x_j} - \frac{\partial}{\partial x_j} \left(\mu \left(\frac{\partial u_i}{\partial x_j} + \frac{\partial u_j}{\partial x_i} \right) \right) \right) d\Omega_e \\ & + \sum_{e=1}^{n_{elem}} \int_{\Omega_e} w_i \left(\frac{\partial P}{\partial x_i} + \boldsymbol{\beta}_u \chi_s (\mathbf{u}_i - \mathbf{u}_I) \right) d\Omega_e \end{aligned} \quad (4.10)$$

$$+ \sum_{e=1}^{n_{elem}} \int_{\Omega_e} \left[\rho a_j \frac{\partial w_i}{\partial x_j} - \frac{\partial}{\partial x_j} \left(\mu \left(\frac{\partial w_i}{\partial x_j} + \frac{\partial w_j}{\partial x_i} \right) \right) \right] [\tau \mathbf{g}(x_i)] d\Omega_e = 0$$

where

$$\mathbf{g}(x_i) = \left(\frac{\partial u_i}{\partial t} + a_j \frac{\partial u_i}{\partial x_j} - \frac{\partial}{\partial x_j} \left(\nu \left(\frac{\partial u_i}{\partial x_j} + \frac{\partial u_j}{\partial x_i} \right) \right) + \frac{\partial P}{\partial x_i} + \boldsymbol{\beta}_u \chi_s (\mathbf{u}_i - \mathbf{u}_I) \right)$$

The bold term, $\boldsymbol{\beta}_u \chi_s (\mathbf{u}_i - \mathbf{u}_I)$, is the penalization term that forces the velocity to zero at the fluid-solid interface and ν is the fluid kinematic viscosity. The stabilization term, as derived by [57], is defined as:

$$\tau = \left(\frac{1}{\tau_1^2} + \frac{1}{\tau_2^2} + \frac{1}{\tau_3^2} \right)^{-\frac{1}{2}} \quad (4.11)$$

$$\tau_1 = \frac{h_{cl}}{2 \|a_i\|_2}, \tau_2 = \frac{\Delta t}{2}, \tau_3 = \frac{h_{cl}^2}{4\nu} \quad (4.12)$$

4.2.2 Streamwise Upwind Petrov Galerkin

The Petrov-Galerkin method is a mathematical approach used to obtain solutions for PDEs with terms of odd order. The Streamwise Upwind Petrov Galerkin (SUPG) method introduces artificial diffusion in the streamwise direction only. This requires that the test function of the advection terms be modified and that this modified test function is applied to all terms of the weak form.

SUPG for INS Equations

The final form of the SUPG stabilized INS equations is as follows:

$$\sum_{e=1}^{n_{elem}} \int_{\Omega_e} \left(w \frac{\partial u_i}{\partial x_i} + \frac{\partial w}{\partial x_i} [\tau \mathbf{g}(x_i)] \right) d\Omega_e = 0 \quad (4.13)$$

$$\begin{aligned} \sum_{e=1}^{n_{elem}} \int_{\Omega_e} w \left(\rho \frac{\partial u_i}{\partial t} + \rho a_j \left(\frac{\partial u_i}{\partial x_j} \right) - \mu \frac{\partial}{\partial x_j} \left(\frac{\partial u_i}{\partial x_j} + \frac{\partial u_j}{\partial x_i} \right) + \frac{\partial P}{\partial x_i} - \rho F_i \right) d\Omega_e \\ + \sum_{e=1}^{n_{elem}} \int_{\Omega_e} (-(\delta^h + \epsilon^h)(\mathbf{g}(x_i))) d\Omega_e = 0 \end{aligned} \quad (4.14)$$

where

$$\mathbf{g}(x_i) = \left(\frac{\partial u_i}{\partial t} + a_j \frac{\partial u_i}{\partial x_j} - \frac{\partial}{\partial x_j} \left(\nu \left(\frac{\partial u_i}{\partial x_j} + \frac{\partial u_j}{\partial x_i} \right) \right) + \frac{1}{\rho} \frac{\partial P}{\partial x_i} - F_i \right)$$

The Petrov-Galerkin functions δ^h and ϵ^h are defined as:

$$\delta^h = \tau_{SUPG} \left(a_j \left(\frac{\partial w_i}{\partial x_j} \right) \right) \quad (4.15)$$

$$\epsilon^h = \tau_{PSPG} \left(\frac{1}{\rho} \frac{\partial w_i}{\partial x_j} \right) \quad (4.16)$$

where the SUPG and the pressure-stabilizing/Petrov-Galerkin (PSPG) terms are:

$$\tau_{SUPG} = \frac{h_{cl}}{2\|a_j\|} z(Re_a) \quad (4.17)$$

$$\tau_{PSPG} = \frac{h_{cl}}{2\|U\|} z(Re_U) \quad (4.18)$$

in which Re_a and Re_U are element Re numbers based on the local velocity a_j and the global scaling velocity U , respectively.

$$Re_a = \frac{\|a_j\| h_{cl}}{2\nu} \quad (4.19)$$

$$Re_U = \frac{\|U\| h_{cl}}{2\nu} \quad (4.20)$$

The function $z(Re)$ is expressed as:

$$z(Re) = \begin{cases} Re/3, & 0 \leq Re \leq 3 \\ 1, & 3 \leq Re \end{cases} \quad (4.21)$$

4.2.3 Variational Multiscale

Variational Multiscale (VMS) is a method that can be used to improve the spatial accuracy by applying a sub-grid. For this method, the solution variable is decomposed into two parts: a coarse and a fine-scale. The coarse-scale solution is solved on the mesh while the fine-scale is evaluated analytically and is local to each element. This method is used in the hybrid Taylor-Galerkin (TG) VMS stabilization scheme for level set advection.

VMS for INS Equations

For the INS equations, only the velocity term is decomposed into coarse and fine scales because the pressure term does not contribute to the advection or the diffusion terms in the momentum equations.

The final form of the VMS stabilized INS equations is as follows:

$$\sum_{e=1}^{n_{elem}} \int_{\Omega_e} \left(w \frac{\partial u_i}{\partial x_i} + \frac{\partial w}{\partial x_i} [\tau \mathbf{g}(x_i)] \right) d\Omega_e = 0 \quad (4.22)$$

$$\begin{aligned} & \sum_{e=1}^{n_{elem}} \int_{\Omega_e} w \left(\rho \frac{\partial u_i}{\partial t} + \rho a_j \left(\frac{\partial u_i}{\partial x_j} \right) - \mu \frac{\partial}{\partial x_j} \left(\frac{\partial u_i}{\partial x_j} + \frac{\partial u_j}{\partial x_i} \right) + \frac{\partial P}{\partial x_i} - \rho F_i \right) d\Omega_e \\ & + \sum_{e=1}^{n_{elem}} \int_{\Omega_e} \left(-\rho a_j \frac{\partial w}{\partial x_j} - \mu \frac{\partial^2 w}{\partial x_j^2} \right) (-\tau_e \mathbf{g}(x_i)) d\Omega_e \\ & + \sum_{e=1}^{n_{elem}} \int_{\Omega_e} \left(-\mu \frac{\partial^2 w}{\partial x_j \partial x_i} \right) (-\tau_e (\mathbf{g}(x_i))) d\Omega_e = 0 \end{aligned} \quad (4.23)$$

where

$$\mathbf{g}(x_i) = \left(\frac{\partial u_i}{\partial t} + a_j \frac{\partial u_i}{\partial x_j} - \frac{\partial}{\partial x_j} \left(v \left(\frac{\partial u_i}{\partial x_j} + \frac{\partial u_j}{\partial x_i} \right) \right) + \frac{1}{\rho} \frac{\partial P}{\partial x_i} - F_i \right)$$

The matrix of stabilization parameters, τ_e , is replaced by a stabilization term, τ , that can be written as:

$$\tau = \left(\frac{1}{\tau_1^2} + \frac{1}{\tau_2^2} + \frac{1}{\tau_3^2} \right)^{-\frac{1}{2}} \quad (4.24)$$

$$\tau_1 = \frac{h_{cl}}{2\|a_i\|_2}, \tau_2 = \frac{\Delta t}{2}, \tau_3 = \frac{h_{cl}^2}{4\nu} \quad (4.25)$$

4.3 Static Condensation

Static condensation is used for the enriched INS equations to ensure that the number of DOFs remains constant in order to avoid complications that are known to arise from a variable size system. The static condensation process can be used to eliminate the enriched DOF while still accounting for their effects.

The process can be summarized as follows beginning with a matrix formed with enriched and nonenriched components.

$$\begin{bmatrix} A & B \\ B^T & D \end{bmatrix} \begin{bmatrix} V \\ V^{enr} \end{bmatrix} = \begin{bmatrix} F \\ F^{enr} \end{bmatrix} \quad (4.26)$$

where V is the original vector containing the nodal velocity u_i and pressure P , V^{enr} is the enriched vector containing the enriched pressure P^{enr} , and A is a matrix containing the coefficients of the original DOF. B is a matrix containing the coefficients of the enriched pressure enrichment terms, B^T contains the coefficients of the original stabilized DOF, and C is comprised of the coefficients of the stabilized enriched pressure enrichment terms. F and F^{enr} are the body force vectors in the original DOF and enriched DOF, respectively.

Expanding the system of equations into:

$$AV + BV^{enr} = F \quad (4.27)$$

$$B^T V + DV^{enr} = F^{enr} \quad (4.28)$$

The enriched DOF vector V^{enr} can be written as:

$$V^{enr} = D^{-1}F^{enr} - D^{-1}B^T V \quad (4.29)$$

Substitution the enriched DOF vector V^{enr} into the system of equation is written as:

$$AV - BD^{-1}B^T V = F - BD^{-1}F^{enr} \quad (4.30)$$

$$A_c V = F_c \quad (4.31)$$

Solving $A_c V = F_c$ keeps the number of DOFs constant and accounts for the effects of the enriched terms.

4.4 Temperature-Based Energy Equation

The XFEM solver uses the temperature-based energy equation written as:

$$\rho c_p \frac{\partial T}{\partial t} + \rho c_p u_j \frac{\partial T}{\partial x_j} - \frac{\partial}{\partial x_j} \left(k \left(\frac{\partial T}{\partial x_j} + \frac{\partial T}{\partial x_i} \right) \right) = 0 \quad (4.32)$$

The weak Galerkin form of the temperature-based energy equation is:

$$\sum_{e=1}^{n_{elem}} \int_{\Omega_e} w_i \left(\rho c_p \frac{\partial T}{\partial t} + \rho c_p u_j \frac{\partial T}{\partial x_j} - \frac{\partial}{\partial x_j} \left(k \left(\frac{\partial T}{\partial x_j} + \frac{\partial T}{\partial x_i} \right) \right) \right) d\Omega_e = 0 \quad (4.33)$$

The stabilized GLS form of the temperature-based energy equation, with penalization forcing the interface to the user-defined temperature T_n , is expressed as:

$$\begin{aligned} \sum_{e=1}^{n_{elem}} \int_{\Omega_e} w_i \left(\rho c_p \frac{\partial T}{\partial t} + \rho c_p a_j \frac{\partial T}{\partial x_j} - \frac{\partial}{\partial x_j} \left(k \left(\frac{\partial T}{\partial x_j} + \frac{\partial T}{\partial x_i} \right) \right) + \beta_T \chi_s(T - T_n) \right) d\Omega_e \\ + \sum_{e=1}^{n_{elem}} \int_{\Omega_e} \left[\rho c_p a_j \frac{\partial w_i}{\partial x_j} - \frac{\partial}{\partial x_j} \left(k \left(\frac{\partial w_i}{\partial x_j} + \frac{\partial w_i}{\partial x_i} \right) \right) \right] [\tau_{enrg} \mathbf{h}(x_i)] d\Omega_e = 0 \end{aligned} \quad (4.34)$$

where

$$\mathbf{h}(x_i) = \left(\frac{\partial T}{\partial t} + a_j \frac{\partial T}{\partial x_j} - \frac{1}{\rho c_p} \frac{\partial}{\partial x_j} \left(k \left(\frac{\partial T}{\partial x_j} + \frac{\partial T}{\partial x_i} \right) \right) + \beta_T \chi_s(T - T_n) \right)$$

The penalization term, $\beta_T \chi_s(T - T_n)$, forces the temperature to melting temperature at the fluid-solid interface. The stabilization term τ_{enrg} is defined as:

$$\tau_{enrg} = \left(\frac{1}{\tau_1^2} + \frac{1}{\tau_2^2} + \frac{1}{\tau_3^2} \right)^{-\frac{1}{2}} \quad (4.35)$$

where

$$\tau_1 = \frac{h_{cl}}{2\|\mathbf{a}_i\|}, \tau_2 = \frac{\Delta t}{2}, \text{ and } \tau_3 = \frac{h_{cl}^2}{4 \left(\frac{k}{\rho c_p} \right)}$$

4.5 XFEM

XFEM allows for additional shape functions to be incorporated within the standard shape functions to help represent a discontinuous field. The variables are approximated as:

$$v(x_i) = \sum_{e=1}^{nne} (N^e(x_i)v^e + M^e(x_i)v^{e,enr}) \quad (4.36)$$

The enrichment shape function $M^e(x_i)$ is chosen so that the enrichment term vanishes at the element nodes. This avoids complications when applying boundary conditions and simplifies the calculation of the variable values at the element nodes.

The definition of the enrichment shape functions should also keep the Kronecker- δ property over the enriched element. This can be done with the following definition:

$$M^e(x_i) = N^e(x_i)(\zeta(x_i) - \zeta(x_i^e)) \quad (4.37)$$

The choice of $\zeta(x_i)$ depends on the discontinuity that is present. A signed Heaviside function is used for strong discontinuities while a signed ramp function is used for weak discontinuities. A choice made to reduce the computational cost is to have partial enrichment where only elements that are “cut” by the interface are enriched.

This enrichment strategy leads to three types of elements in the domain. Enriched elements have all nodes enriched while regular elements have no nodes enriched. The elements with only some, but not all, nodes enriched are called blending elements. Parasitic terms arising in these blending elements may cause issues with convergence. Another issue is that partial enrichment results in a changing number of DOFs, which may lead to difficulties when solving the system of equations.

The enrichment shape function for the INS equations is a signed Heaviside function since pressure is a strong discontinuity across the fluid-structure interface [58]. The pressure field is enriched, as suggested in [59], such that:

$$P(x) = P_i + P_i^{enrich} = \sum_{i=1}^{N_{elem}} N_i(x) P_i + M_i(x) P_i^{enrich} \quad (4.38)$$

where for the pressure, the sign-enrichment scheme is applied:

$$M_i(x) = \left(\text{sign}(\phi(x, t)) - \text{sign}(\phi_i(t)) \right) N_i \quad (4.39)$$

The weakly discontinuous temperature, on the other hand, uses a modified abs-enrichment scheme that eliminates the need for a ramp function in blending elements.

The temperature is also enriched such that:

$$T(x) = T_i + T_i^{enrich} = \sum_{i=1}^{N_{elem}} N_i(x) T_i + M_i(x) T_i^{enrich} \quad (4.40)$$

where for the temperature, the modified abs-enrichment scheme is used:

$$M_i(x) = (|\varphi_i|N_i(x) - |\varphi_i N_i(x)|)^{1.4} \quad (4.41)$$

The current XFEM flow solver uses static condensation for the INS enriched equations.

4.6 Splitting Approaches with XFEM

Regular Gaussian integration rules in elements differ when the elements are “cut” by the interface since the basis functions are not continuous over the element. This results in the XFEM elements needing to be divided into non-overlapping sub-elements where the Gaussian integration rules are valid. There are two different splitting approaches, implemented in [60], that can be utilized: geometric splitting and equal splitting. If there are enough sub-elements, both splitting approaches should yield similar results. After the splitting approach is used, Gaussian integration rules are applied to each sub-element, as they are for the non-XFEM elements.

4.6.1 Geometric Splitting

Geometric splitting involves sub-elements that are aligned with the interface. This requires that the approach locate and then conform the splitting to the interface, which adds a layer of complexity that is not necessary for the equal splitting approach. However, unlike equal splitting, fewer sub-elements can be used for correct results since the interface is already located. For both splitting approaches, triangular (2D) or tetra (3D) sub-elements are required to preserve the exact numerical integration properties of the Gaussian integration. An example of geometric splitting is shown in Figure 4-1.

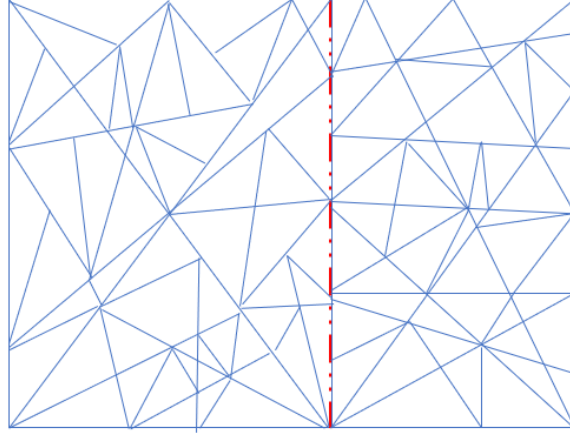


Figure 4-1 Geometric splitting of domain with red dashed line as the interface

The geometric splitting procedure locates the intersection points between the interface and the element edges and then connects these interface points with segments into lines. The level set value at the midpoint of the segments is evaluated and used to identify the correct locations of the interface “cuts” with that element. After the interface lines have been correctly identified, Delaunay triangulation within the element is used in creating the interface-conforming sub-elements.

Given the complexity of the geometric splitting approach and the likelihood that it would become computationally intractable for large 3D problems, the adoption of the equal splitting approach is chosen for the rest of the thesis work. The results obtained in the Results section were performed with equal splitting.

4.6.2 Equal Splitting

Equal splitting involves sub-elements of equal size that are not aligned with the interface. In general, it requires a larger number of sub-elements in comparison to geometric splitting because enough sub-elements on both sides of the “cut” element are needed for correct results. However, equal splitting does not require locating the interface and conforming the sub-element to that interface, thus the complexity of implementing this approach is less than that for implementing geometric splitting. An example of equal splitting is shown in Figure 4-2.

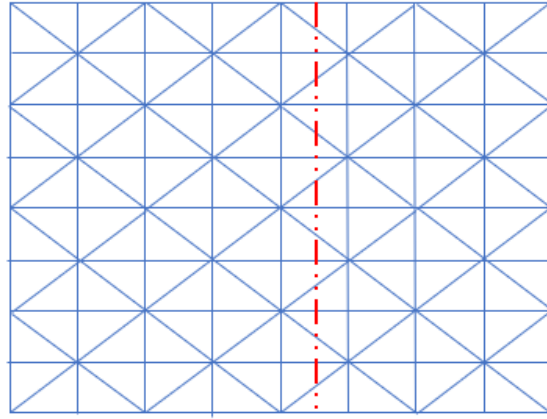


Figure 4-2 Equal splitting of domain with red dashed line as the interface

The implementation selects an element, and given the restriction imposed as to the area and maximum interior angle, the element is subdivided equally into sub-elements. A setting with a maximum angle of 30 degrees and a non-dimensional area of 0.005 produces around 1000 sub-elements which are sufficient to obtain accurate results with Gaussian integration rules.

4.6.3 Computational Procedure for Fluid-Structure Implementation

The methodology to model the FSI with/without convection is summarized in the computational procedure below.

- 1) Identify the computational domain and location of the interface
- 2) Initialize ϕ , T , u_i , and p
- 3) Loosely-couple the heat transfer and hydrodynamics
 - a) Solve consecutively until both converge
 - i) Loop over all elements
 - ii) Check all element if cut; if cut, enrich the element nodes
 - iii) Assemble the discrete system and solve
 - b) Update u_i and p while assuming T until nonlinear system for the INS equations converge, then use u_i and p to update T
- 4) Repeat step 3 when unsteady

4.7 Stefan Problem

The Stefan problem is a BVP that consists of the temperature distribution in a homogeneous medium undergoing a phase change and a phase boundary that is moving in time. It solves the heat equation by setting an initial temperature distribution in the whole domain and then imposes a Stefan condition on the moving free-boundary between the two phases. The schematic of a solidification domain is shown in Figure 4-3, with Ω_s and Ω_l representing the solid and fluid domains, respectively, and Γ denoting the phase change interface.

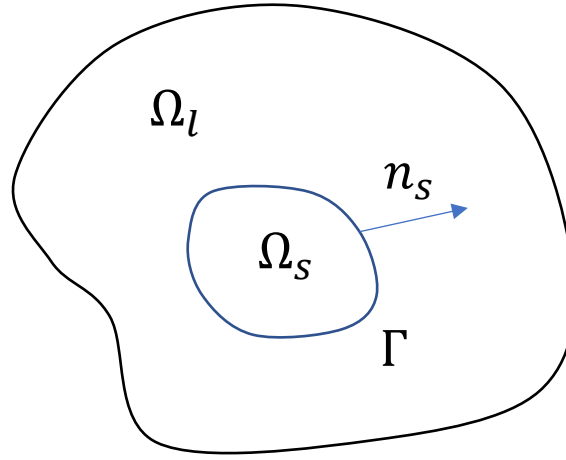


Figure 4-3 Schematic representation of solidification domain

The Stefan condition describes the local velocity of the moving boundary as a function of quantities evaluated at both sides of the phase boundary. In the case of heat transfer with phase change, the physical constraint is the conservation of energy, so the velocity of the interface is due to the heat flux discontinuity at the interface between the two phases.

XFEM with LSM can be used to solve the Stefan problem by a) calculating the interface speed of the phase change, b) extending that speed throughout the domain, c) using that extended velocity to advect the level set and then d) deriving the temperature distribution in the domain from the conservation of energy. The following subsections will discuss each step of this process in detail.

4.7.1 Interface Speed

Before determining the interface speed, the Stefan problem must be recalled. Considering a domain composed of a solid and a fluid region, the fluid/solid interface is defined by the SDF, which follows the sign convention:

$$\phi(x_i, t) \begin{cases} > 0, & x \in \Omega_f \\ = 0, & x \in \Gamma_I \\ < 0, & x \in \Omega_s \end{cases} \quad (4.42)$$

Both phases must satisfy the energy conservation equation in the domain:

$$\rho \frac{\partial}{\partial t} (c_p T) = \nabla \cdot (k \nabla T) \quad (4.43)$$

The assumption is that density is the same for both phases, which means that material transport due to expansion or shrinkage from phase change and buoyancy effects can be neglected. The boundary conditions on the interface are:

$$T_s = T_f = T_m \quad (4.44)$$

$$q = (k_f \nabla T_f - k_s \nabla T_s) \cdot n_s = -\rho L v \quad (4.45)$$

The initial conditions are:

$$T(x, t = 0) = T(x) \quad (4.46)$$

$$\phi(x, t = 0) = \phi(x) \quad (4.47)$$

Given the boundary conditions, the interface speed can be determined as:

$$v = \frac{(k_s \nabla T_s - k_f \nabla T_f) \cdot n_s}{\rho L} \quad (4.48)$$

which requires that ∇T_s and ∇T_f be accurately computed from the temperature distribution in the domain. The heat flux evaluation has been performed by using the slope of a line built from two sample points on either side of the interface to approximate the interface temperature. These points

have been set at 2δ distance away from the interface, as seen in Figure 4-4, which corresponds to approximately ten percent of the characteristic element length.

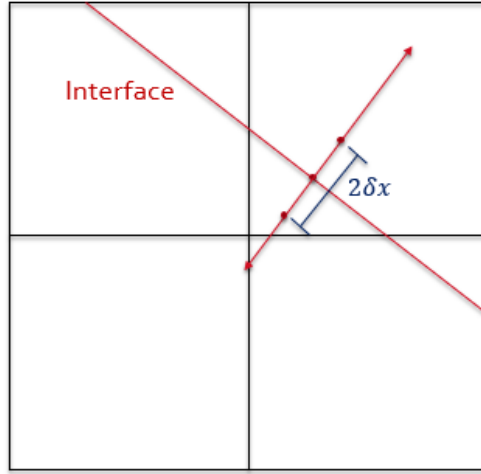


Figure 4-4 Element interface calculation

4.7.2 Extension of Interface Speed

Once the interface speed is computed, the extension/spreading of the interface speed throughout the whole domain can be done using a PDE. Since the interface speed is only known on the interface, a velocity field on the domain must be constructed from the interface normal speed prior to the level set advection. To achieve this, a convention that the interface speed is orthogonal to ϕ is used. The PDE that must be solved is defined as follows:

$$\text{Sign}(\phi)\nabla F \cdot \nabla \phi = 0 \quad (4.49)$$

with the boundary condition that:

$$F(x, t) = v \text{ on } \Gamma \quad (4.50)$$

The partial differential equation chosen allows for the spreading of the interface speed to be extended along the characteristic lines. This is shown in Figure 4-5.

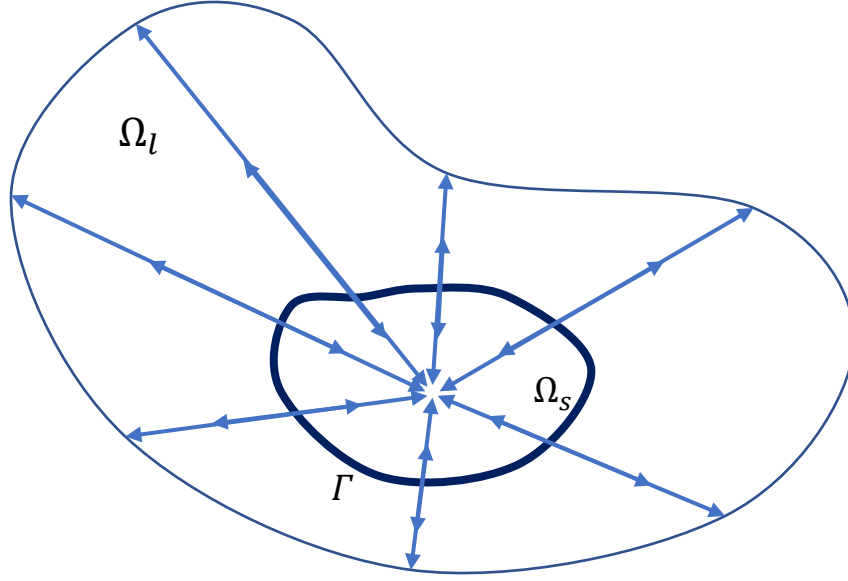


Figure 4-5 Characteristic lines showing the extension of interface speed

This can be solved with XFEM using the GLS stabilized weak form:

$$\int_{\Omega} \delta F \text{sign}(\phi) \nabla F \cdot \nabla \phi d\Omega + \sum_e \int_{\Omega} (\nabla \delta F \cdot \nabla \phi) \tau^e (\nabla \phi \cdot \nabla F) d\Omega = 0 \quad (4.51)$$

where the stabilization term τ^e is defined as:

$$\tau^e = \frac{h_{cl}}{\|\nabla \phi\|} \quad (4.52)$$

4.7.3 Advection of Level Set with Interface Velocity

With the extended interface speed now having been computed for the entire domain, the level set can be advected with that velocity. The level set advection equation is defined as:

$$\partial \phi / \partial t + v \cdot \nabla \phi \equiv \partial \phi / \partial t + F \|\nabla \phi\| = 0 \quad (4.53)$$

Now F is a scalar velocity field, calculated in the extension of interface speed section above, is defined as:

$$F = n \cdot v = \frac{\nabla \phi}{\|\nabla \phi\|} \cdot v \quad (4.54)$$

By re-writing v in terms of F , the 2TGVMS level set advection equation discretization can be used to advect the level set serving as the phase change boundary and solve the Stefan problem.

4.7.4 Conservation of Energy

After the interface speed and the level sets have been calculated, the energy equation is solved to establish the temperature distribution in the domain. The weak form of the energy equation, using the backward distance formula, is expressed as:

$$\frac{1}{\Delta t} \int_{\Omega} w \rho \left((c_p T)^{n+1} - (c_p T)^n \right) d\Omega + \int_{\Omega} \nabla w \cdot (k \nabla T)^{n+1} d\Omega = 0 \quad (4.55)$$

For the elements that are “cut” by the interface between the two phases, the energy equation requires that the interface temperature condition be enforced. This is done by a penalty method that uses a parameter which is of the order of 10^6 or higher to enforce the temperature at the interface.

The weak form of the energy equation, with the penalty method, is expressed as follows:

$$\begin{aligned} & \frac{1}{\Delta t} \int_{\Omega} w \rho c_p (T^{n+1} - T^n) d\Omega \\ & + \int_{\Omega} \nabla w \cdot (k \nabla T)^{n+1} d\Omega + \int_{\Omega} w \beta_T X (T - T_m) d\Omega = 0 \end{aligned} \quad (4.56)$$

No stabilization is necessary for the conservation of energy equation above since there is no advection component. When the Stefan problem is coupled to the hydrodynamics problem, then stabilization will be necessary since the fluid is no longer assumed stationary. An advection term will be present and will link the motion of the fluid melt to the heat transfer present in the domain. This implementation modification is discussed in the subsequent section.

4.8 LSM

LSM, Volume of Fluid (VOF) and Phase Field are three Eulerian interface capturing methods. The latter is seldom used in realistic two-phase problems and has been found to be less accurate than VOF [61]. The main difference between LSM and VOF is that the latter involves explicit reconstruction of the interface based on the transport of the local volume fraction of the liquid, whereas the former does not. Since LSM provides a continuous interface representation, it can be more accurate than VOF at determining surface tension forces [60]. Additionally, LSM avoids problems that arise from the need to track the individual particles; hence it is more robust than a Lagrangian approach. Given that it is an interface capturing method and not an interface tracking method like body-conforming methods, the interface information can be stored in a scalar function.

4.8.1 SDF

One commonly used scalar functions in LSM is the SDF, which denotes the minimum distance between a node and the interface. The distance function is defined as:

$$d(x_i) = \text{Min}(|x_i - x_{i,int}|) \quad (4.57)$$

The SDF is defined as:

$$\phi(x_i) = \begin{cases} +d(x_i), & \text{liquid} \\ 0, & \text{interface} \\ -d(x_i), & \text{solid} \end{cases} \quad (4.58)$$

A special property of the SDF defines the surface normal and curvature as:

$$n_i = \frac{\frac{\partial \phi}{\partial x_i}}{\left\| \frac{\partial \phi}{\partial x_i} \right\|_2} \quad (4.59)$$

$$\kappa_i = \frac{\partial}{\partial x_i} \left(\frac{\frac{\partial \phi}{\partial x_i}}{\left\| \frac{\partial \phi}{\partial x_i} \right\|_2} \right) \quad (4.60)$$

4.8.2 Level Set Advection

The level set is advected using the advection equation:

$$\frac{\partial \phi}{\partial t} + u_i \frac{\partial \phi}{\partial x_i} = 0 \quad (4.61)$$

It is important to be aware that the level set has two important properties when the scalar function is an SDF: the definition of the surface normal and the surface curvature. When the interface is advected in time, ϕ may become irregular and lose its SDF properties, since the velocity field u_i does not necessarily transport all the level sets with the same velocity. This can result in the incorrect motion of the interface and can increase the mass loss by the LSM. To mitigate this problem, a geometric reconstruction re-initialization scheme has been implemented after the fast-marching method developed by J.A Sethian [62].

4.8.3 Level Set Advection with Second-Order Taylor-Galerkin Variational Multiscale Stabilization

The LSM approach has a mass conservation issue which is common for interface capturing techniques, but for LSM there are several approaches that can reduce the mass loss. A conservative form of the level set, a higher-order spatial and temporal discretization, a combination of LSM with another interface capturing approach like VOF, and a seeding of particles on the level set interface are four ways to alleviate the mass non-conservative property of the scheme. The FE implementation of LSM has been achieved in the literature with SUPG, GLS, TG, and VMS. The second-order Taylor-Galerkin Variational Multiscale (2TGVMS) is a hybrid stabilization method developed in [63], that uses a higher-order discretization and combines the TG method with VMS, will be used to advect the level set.

The TG discretization of the level set equations begins with the implicit Taylor series expansion in time:

$$\phi^n = \phi^{n+1} + \sum_{i=1}^j \frac{(t^n - t^{n+1})^i}{i!} \frac{\partial^i \phi}{\partial t^i} \quad (4.62)$$

2TGVMS uses a 2nd order expansion:

$$\frac{\partial \phi^{n+1}}{\partial t} = \frac{\phi^{n+1} - \phi^n}{\Delta t} + \frac{\Delta t}{2} \frac{\partial^2 \phi^{n+1}}{\partial t^2} \quad (4.63)$$

The weak-Galerkin form of the level set equation can be written as:

$$\sum_{e=1}^{n_{elem}} \int_{\Omega_e} w^e \left(\frac{\partial \phi}{\partial t} + u^e_i \cdot \frac{\partial \phi^e}{\partial x_i} \right) d\Omega_e = 0 \quad (4.64)$$

When the 2nd order temporal expansion is introduced, the weak-Galerkin form becomes:

$$\sum_{e=1}^{n_{elem}} \int_{\Omega_e} w^e \left(\frac{\phi^{e,n+1} - \phi^{e,n}}{\Delta t} + \frac{\Delta t}{2} \frac{\partial^2 \phi}{\partial t^2} + u^{e,n+1}_i \cdot \frac{\partial \phi^{e,n+1}}{\partial x_i} \right) d\Omega_e = 0 \quad (4.65)$$

The TG weak form of the level set advection equation using a 2nd order expansion for the temporal term can be rewritten as:

$$\sum_{e=1}^{n_{elem}} \int_{\Omega_e} w^e \left(\frac{\phi - \phi^n}{\Delta t} + \frac{\Delta t}{2} u_i \frac{\partial}{\partial x_i} \left(u_j \frac{\partial \phi}{\partial x_j} \right) + u^a_i \cdot \frac{\partial \phi}{\partial x_i} \right) d\Omega_e = 0 \quad (4.66)$$

This formulation is then coupled with a sub-grid method called VMS to improve the spatial accuracy of the LSM.

The second-order Taylor-Galerkin VMS weak formulation, modified in the present methodology from that outlined in [63], is expressed as:

$$\begin{aligned} & \sum_{e=1}^{n_{elem}} \int_{\Omega_e} w_i \left(\frac{\partial \phi}{\partial t} \right) d\Omega_e + \sum_{e=1}^{n_{elem}} \int_{\Omega_e} w_i \left(u_i \cdot \frac{\partial \phi}{\partial x_i} + \frac{\Delta t}{2} u_i \cdot \frac{\partial}{\partial x_i} \left(u_j \cdot \frac{\partial \phi}{\partial x_j} \right) \right) d\Omega_e \\ & + \sum_{e=1}^{n_{elem}} \int_{\Omega_e} \left[\frac{w}{\Delta t} - u_i \cdot \frac{\partial w}{\partial x_i} + \frac{\Delta t}{2} u_i \cdot \frac{\partial}{\partial x_i} \left(u_j \cdot \frac{\partial w}{\partial x_j} \right) \right] [\tau_e \mathbf{j}(x_i)] d\Omega_e = 0 \end{aligned} \quad (4.67)$$

where $\mathbf{j}(x_i)$ is:

$$j(x_i) = \frac{\partial \phi}{\partial t} - u_i \cdot \frac{\partial \phi}{\partial x_i} + \frac{\Delta t}{2} u_i \cdot \frac{\partial}{\partial x_i} \left(u_j \cdot \frac{\partial \phi}{\partial x_j} \right)$$

The stabilization term τ_e takes the form:

$$\tau_e = \left(\frac{1}{\tau_1^2} + \frac{1}{\tau_2^2} \right)^{-\frac{1}{2}} \quad (4.68)$$

where

$$\tau_1 = \frac{h_{cl}}{2\|\mathbf{u}_i\|}, \tau_2 = \frac{\Delta t}{2}$$

4.8.4 Level Set Reinitialization by Geometric Reconstruction

Geometric reconstruction begins at the interface and then propagates the information outward to every node. The fast marching method is a numerical method developed in [62] for solving BVPs. Specifically, the fast marching method solves the BVP of the Eikonal equation.

The Eikonal equation is defined as:

$$|\nabla u(x)| = 1/f(x) \text{ for } x \in \Omega \quad (4.69)$$

$$u(x) = 0 \text{ for } x \in \partial\Omega \quad (4.70)$$

which describes the minimum amount of time/distance it would take to reach $\partial\Omega$ from the location x .

The fast-marching method algorithm begins by discretizing the domain into a mesh, where each node has a given value $u(x_i)$. The nodes are labeled as Known, Trial, and Far. Known are the nodes with prescribed solutions, while Trial are the unknown nodes adjacent to the Known nodes, and Far are the remaining nodes. All nodes are initialized to infinity and Trial nodes are inserted into a min-heap. A binary tree in which the value of each parent node is smaller than or equal to the values of the children is known as a min-heap and shown in Figure 4-6.

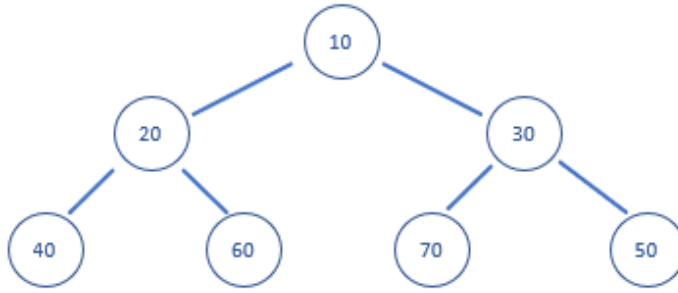


Figure 4-6 Min-Heap data structure

While there are still nodes labeled as Trial, the root of the min-heap is identified as node A. Below is the step-by-step procedure to geometrically reinitialize the LS:

- Add node A to Known while subsequently removing node A from Trial and perform a down-heap.
- If the value assigned to node B, the neighbor of node A, is infinity then add node B to Trial, perform an up-heap and solve the Eikonal update formula.
- Repeat this while there are still neighbors of node A, and nodes remain within the Trial group.

The fast-marching method is used because the algorithm is stable and computationally efficient, as well as to maintain the SDF properties of the level set through geometric reconstruction.

4.9 Thermodynamics Coupled with Hydrodynamics for Multiphase Flows

By implementing two-way coupling, the thermodynamics problem is solved iteratively with the hydrodynamics problem. This allows for the solidification/melting process to affect the flow, as well as having the flow affect the phase change.

The interface capture procedure, the extension of the normal interface speed, and the advection of the level set remain the same. However, the discretization of the INS and the temperature-based energy will be modified since some of the previous assumptions will no longer be used. For example, the assumption that the fluid is stagnant and that the density of the fluid and solid is constant as the fluid changes phase will be removed. The addition of the Boussinesq assumption

means that the current implementation will ignore density differences within the fluid but consider their effects with respect to gravity, hence now accounting for buoyancy-driven flow.

4.9.1 Heat Transfer Coupled with Hydrodynamics

The stabilized GLS form of the INS equations are expressed as:

$$\sum_{e=1}^{n_{elem}} \int_{\Omega_e} \left(w \frac{\partial u_i}{\partial x_i} + \frac{\partial w}{\partial x_i} [\tau \mathbf{g}(x_i)] \right) d\Omega_e = 0 \quad (4.71)$$

$$\begin{aligned} & \sum_{e=1}^{n_{elem}} \int_{\Omega_e} w_i \left(\rho \frac{\partial u_i}{\partial t} + \rho a_j \frac{\partial u_i}{\partial x_j} - \frac{\partial}{\partial x_j} \left(\mu \left(\frac{\partial u_i}{\partial x_j} + \frac{\partial u_j}{\partial x_i} \right) \right) \right) d\Omega_e \\ & + \sum_{e=1}^{n_{elem}} \int_{\Omega_e} w_i \left(\frac{\partial P}{\partial x_i} - \boldsymbol{\rho \alpha}(\mathbf{T} - \mathbf{T}_{ref}) \mathbf{g}_i + \beta_u \chi_s (u_i - u_l) \right) d\Omega_e \end{aligned} \quad (4.72)$$

$$\sum_{e=1}^{n_{elem}} \int_{\Omega_e} \left[\rho a_j \frac{\partial w_i}{\partial x_j} - \frac{\partial}{\partial x_j} \left(\mu \left(\frac{\partial w_i}{\partial x_j} + \frac{\partial w_j}{\partial x_i} \right) \right) \right] [\tau \mathbf{g}(x_i)] d\Omega_e = 0$$

where

$$\mathbf{g}(x_i) = \left(\frac{\partial u_i}{\partial t} + a_j \frac{\partial u_i}{\partial x_j} - \frac{\partial}{\partial x_j} \left(\nu \left(\frac{\partial u_i}{\partial x_j} + \frac{\partial u_j}{\partial x_i} \right) \right) + \frac{\partial P}{\partial x_i} - \boldsymbol{\rho \alpha}(\mathbf{T} - \mathbf{T}_{ref}) \mathbf{g}_i + \beta_u \chi_s (u_i - u_l) \right)$$

The bold $\boldsymbol{\rho \alpha}(\mathbf{T} - \mathbf{T}_{ref}) \mathbf{g}_i$ term is the Boussinesq approximation which will provide a coupling to the energy equation, as T_{ref} will be the melting temperature at the interface.

Additionally, since the INS equations are valid only in the liquid phase, the following velocity and pressure field interpolation scheme, proposed in [23], was added:

$$\mathbf{v}(x, t) = \sum_{i \in I} N_i^v(x) \psi(x, t) \mathbf{v}_i(t) \quad (4.73)$$

$$p(x, t) = \sum_{i \in I} N_i^p(x) \psi(x, t) p_i(t) \quad (4.74)$$

where

$$\psi(x, t) = \begin{cases} 1 & \text{if } \phi(x, t) > 0 \\ 0 & \text{otherwise} \end{cases}$$

The interpolation scheme was chosen so that the solid part of the domain is neglected and only the velocity and pressure DOF within the fluid domain are assembled in the system of equations.

Due to the presence of convection and conduction, the conservation of energy equation must be stabilized for the finite element formulation to get accurate results. The stabilized GLS form of the temperature-based energy equation is expressed as:

$$\begin{aligned} & \sum_{e=1}^{n_{elem}} \int_{\Omega_e} w_i \left(\rho c_p \frac{\partial T}{\partial t} + \rho \mathbf{c}_p \mathbf{a}_j \frac{\partial T}{\partial x_j} - \frac{\partial}{\partial x_j} \left(k \left(\frac{\partial T}{\partial x_j} + \frac{\partial T}{\partial x_i} \right) \right) + \beta_T \chi_s (T - T_m) \right) d\Omega_e \\ & + \sum_{e=1}^{n_{elem}} \int_{\Omega_e} \left[\rho \mathbf{c}_p \mathbf{a}_j \frac{\partial w_i}{\partial x_j} - \frac{\partial}{\partial x_j} \left(k \left(\frac{\partial w_i}{\partial x_j} + \frac{\partial w_i}{\partial x_i} \right) \right) \right] [\tau_{enrg} \mathbf{h}(x_i)] d\Omega_e = 0 \end{aligned} \quad (4.75)$$

where

$$\mathbf{h}(x_i) = \left(\frac{\partial T}{\partial t} + \mathbf{a}_j \frac{\partial T}{\partial x_j} - \frac{1}{\rho c_p} \frac{\partial}{\partial x_j} \left(k \left(\frac{\partial T}{\partial x_j} + \frac{\partial T}{\partial x_i} \right) \right) + \beta_T \chi_s (T - T_m) \right)$$

The $\rho \mathbf{c}_p \mathbf{a}_j \frac{\partial T}{\partial x_j}$ is an advection term that couples the energy equation with the fluid flow motion computed from the INS equations. The computational procedure for the Stefan problem and the coupled Stefan-hydrodynamics problem is explained in the subsequent section.

4.9.2 Computational Procedure for Phase Change Implementation

The methodology to model the phase change process with/without the influence of melt flow is summarized in the computational procedure below.

1. Identify the computational domain and initial location of the interface
2. Initialize ϕ, T, u_i , and p
3. Evaluate interface speed V_I
4. Obtain F by solving equation (4.51)
5. Using F , advect the level set using equation (4.67)
6. If hydrodynamics is required go to step 8); if not, go to step 7)
7. Solve heat transfer (no update for u_i and p since INS is not solved)
 - a. Loop over all elements
 - b. Check all elements; if cut, enrich the element
 - c. Assemble the discrete system and solve
 - d. Update T and go to step 9)
8. Loosely-couple the heat transfer and hydrodynamics
 - a. Solve consecutively until both converge
 - i. Loop over all elements
 - ii. Check all elements; if cut, enrich the element nodes
 - iii. Assemble the discrete system and solve
 - b. Update T while using u_i and then update u_i and p while using the calculated T until nonlinear system converges
9. Repeat steps 3-6 when unsteady

5 Results

5.1 FSI Validation

The developed numerical framework using Brinkman penalization is validated using a lid-driven cavity with an embedded cylinder. XFEM results are compared to those given by the FEM solver using a body-conforming mesh and those obtained by Cai *et al.* [64] using a modified implicit IB technique [63] and a direct forcing method. Two convection cases are simulated to validate the temperature-based energy implementation and subsequently the loose-coupling with the INS equations.

5.1.1 Circular Obstruction, No Convection

The penalization method is applied to the simulation of a lid-driven cavity flow with an embedded cylinder. All variables are non-dimensionalized by the characteristic length, L , of the cavity and free-stream conditions. The cylinder of diameter $D = 0.4L$ is fixed at the center of the cavity. No-slip boundary conditions are prescribed on all walls excluding the top wall that is moving at $u_\infty = 1$. The other boundary conditions are shown in Figure 5-1 and the mesh sizes are presented in Table 5-1.

Table 5-1 Circular obstruction, no convection mesh size

Method	Nodes	Quadrilateral Elements
XFEM	251,001	250,000
Body – Conforming	252,544	251,072

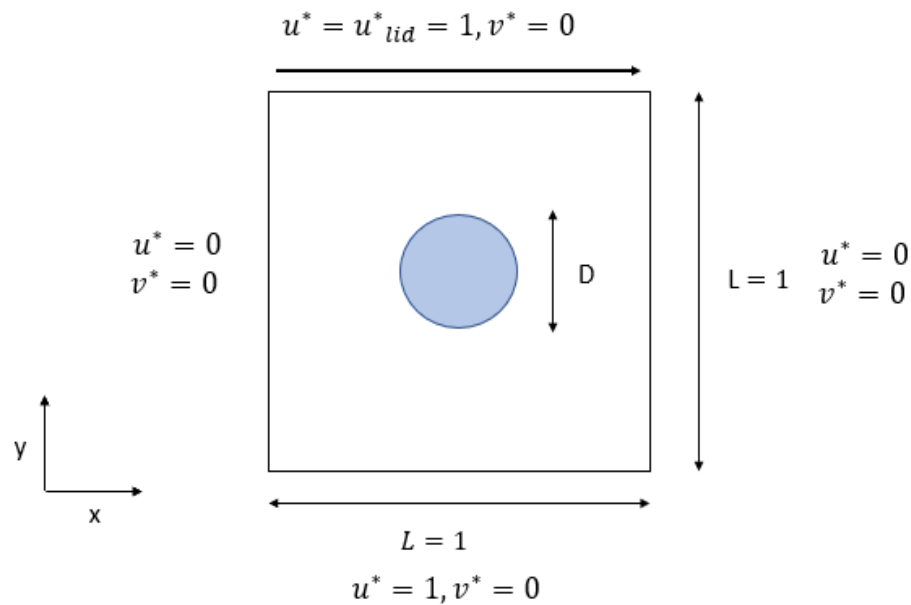


Figure 5-1 Lid-driven cavity with embedded cylinder boundary conditions

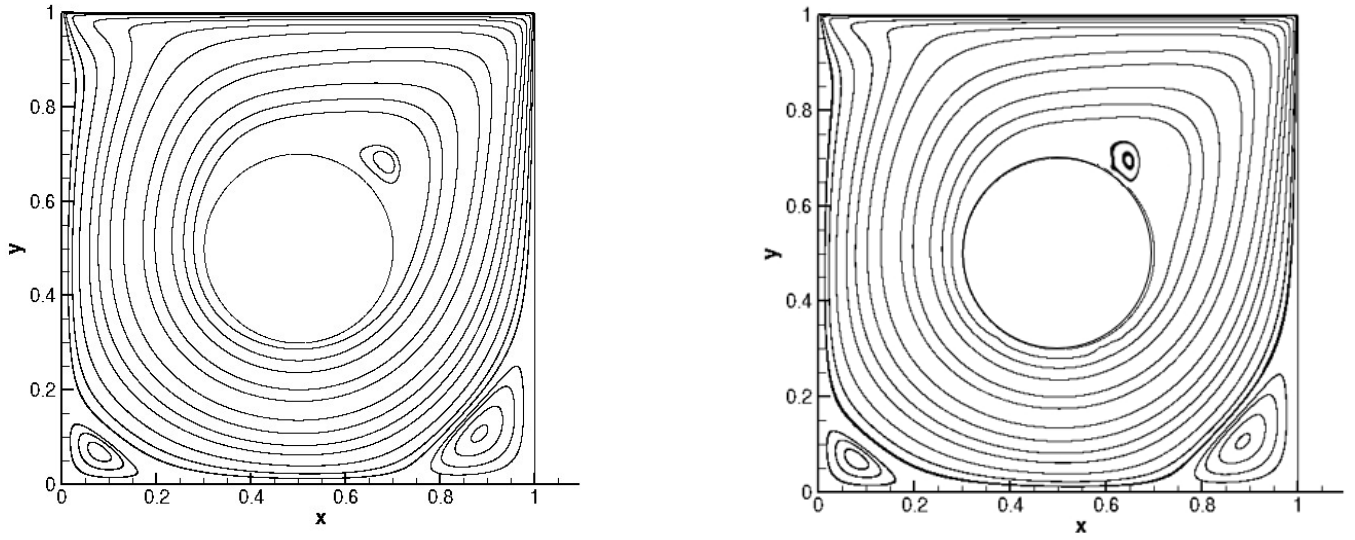


Figure 5-2 Streamlines for the lid-driven cavity flow with an embedded cylinder (left) with the body-conforming mesh, (right) with XFEM

Figure 5-2 shows the streamlines for a Re equal to 1000 for both the XFEM method with penalization and the body-conforming mesh simulations. The slight discrepancies observed in Figure 5-2 may be attributed to the differences between the meshes used in the XFEM and the body-conforming mesh. The body-conforming mesh was refined around the cylinder, while a uniform mesh was used for the XFEM approach. The results are in good agreement with those obtained by Cai *et al.* [64]. The lid-driven cavity flow with embedded cylinder gives rise to three distinct vortices, as depicted in and their locations are given in Figure 5-2. Both the body-conforming mesh FEM and the structured mesh XFEM solutions by the present solver showed close accordance with the “traditional method” (Cai’s body-conforming mesh run) and the IBM used by Cai. A maximum error of 2.75% is noticed between the methods. A good concurrence is also found in Figure 5-3 between the XFEM and body-conforming mesh simulations.

Table 5-2 Comparison of the vortices center positions

	Upper Right Vertex	Lower Left Vertex	Lower Right Vertex
Cai-Traditional Method [64]	(0.6946, 0.6872)	(0.0790, 0.0721)	(0.8856, 0.1061)
Body-Conforming Method	(0.6834, 0.6843)	(0.0771, 0.6994)	(0.8826, 0.1081)
Cai-IBM [64]	(0.6906, 0.6872)	(0.0791, 0.0721)	(0.8849, 0.1063)
XFEM	(0.7096, 0.6547)	(0.0773, 0.7037)	(0.8845, 0.1079)

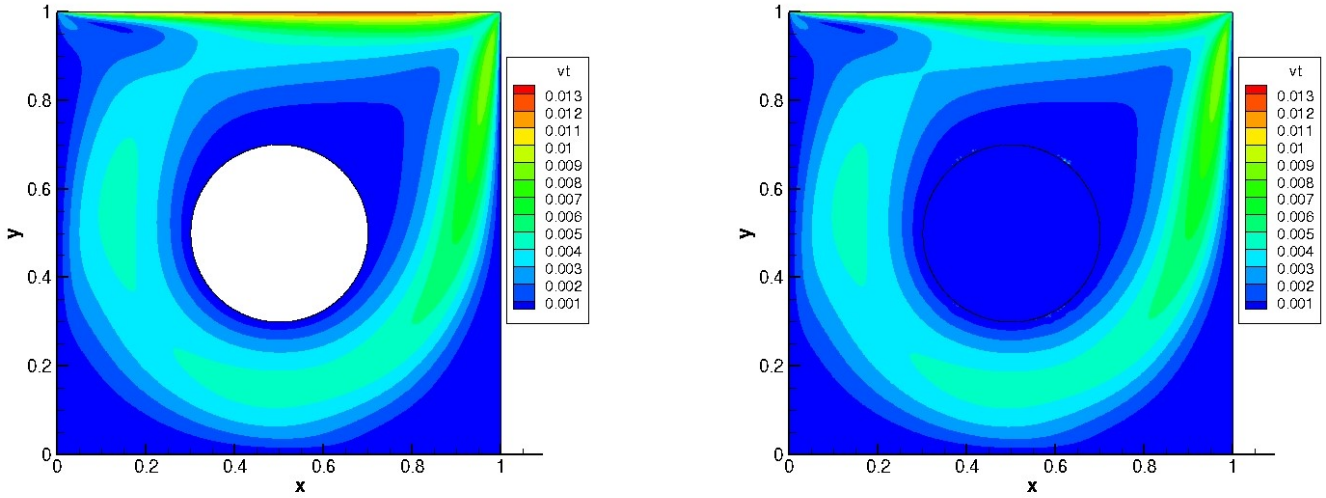


Figure 5-3 Velocity contours for the lid-driven cavity flow with an embedded cylinder
(left) with body-conforming mesh, (right) with XFEM

Figure 5-4 and Figure 5-5 show the profiles of the u and v components of the velocity vector for $y = 0.5$ and $x = 0.5$, respectively. Since the penalization method correctly imposed the no-slip

boundary condition at the interface, the velocity at the interface is zero and the velocity profiles are in good accordance.

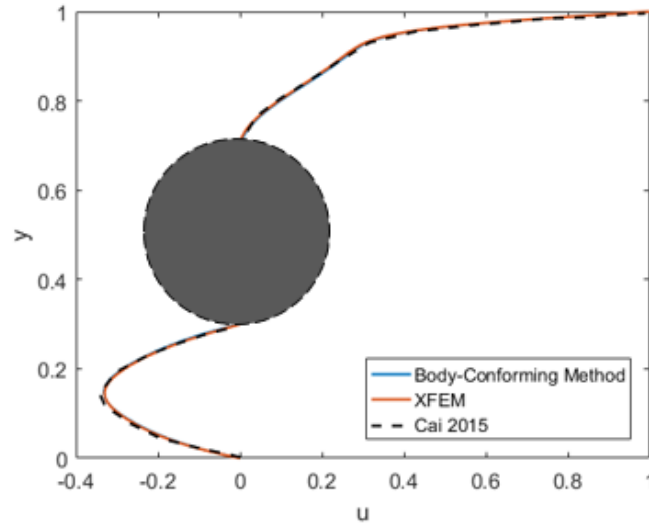


Figure 5-4 Velocity profiles for the lid-driven cavity flow with an embedded cylinder: distribution of velocity component u along the vertical midline

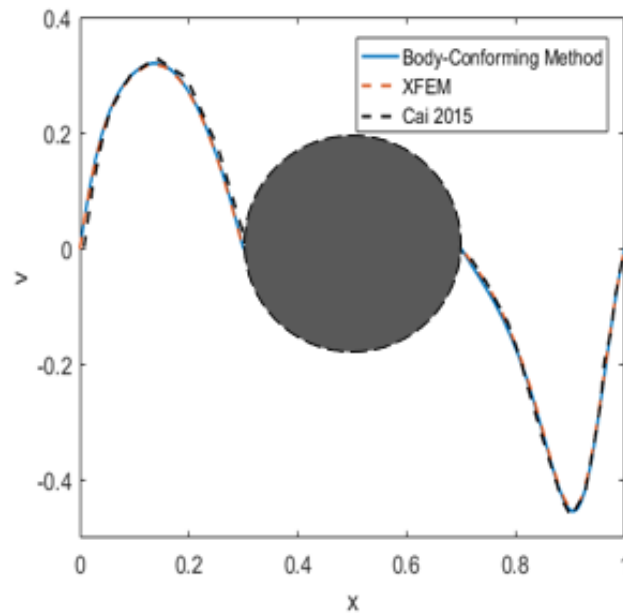


Figure 5-5 Velocity profiles for the lid-driven cavity flow with an embedded cylinder: distribution of velocity component v along the horizontal midline

5.1.2 No Obstruction, Forced Convection

The implementation of the decoupled energy equation was validated using two test cases. The first examined was a forced convection lid-driven cavity flow and the present methodology compared to that of dos Santos *et al.* [65]. The boundary conditions imposed upon the domain are illustrated in Figure 5-6 and the mesh size characteristics are in Table 5-3.

Table 5-3 No obstruction, forced convection mesh size

Method	Nodes	Quadrilateral Elements
XFEM	58,081	57,600
Body – Conforming	58,144	57,482

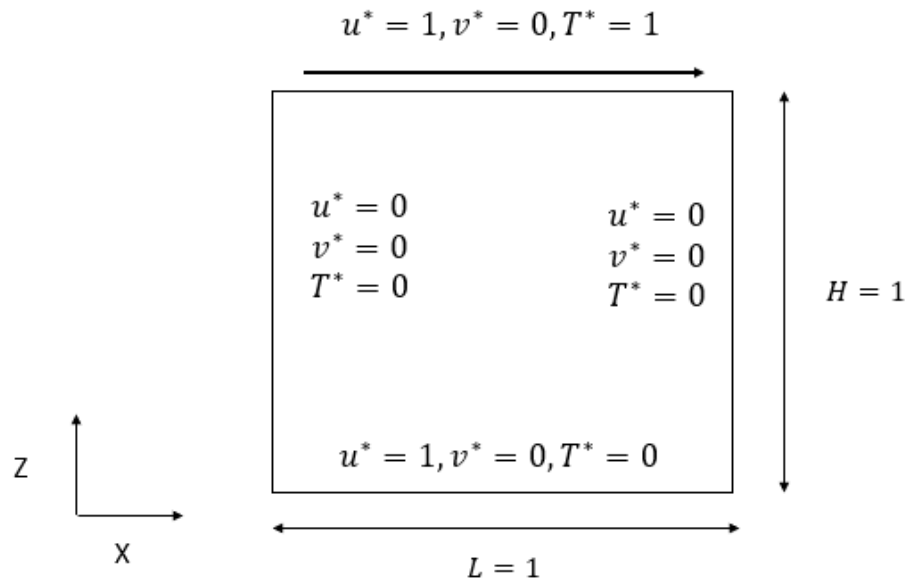


Figure 5-6 Forced convection with no obstruction: cavity flow domain and boundary conditions

Using the notation from [65], the non-dimensional terms are defined as:

$$X = \frac{x}{L}, Z = \frac{z}{H} \quad (5.1)$$

$$u_i^* = \frac{u_i}{u_{1\max}} \quad (5.2)$$

$$T^* = \frac{(T - T_{\min})}{(T_{\max} - T_{\min})} \quad (5.3)$$

where T_{\max} and T_{\min} are the largest and smallest values of temperature in the cavity, $u_{1\max}$ is the velocity of the top surface of the cavity, L is the length and H is the height of the cavity.

Figure 5-7 and Figure 5-8 show the temperature profiles at $Re = 1000$ and Prandtl number (Pr) = 1.0 at steady-state. The results are in close agreement with those obtained by dos Santos [65] and ANSYS Fluent [66]. In Figure 5-7, the results under-predict the temperature along the vertical midline by 1% in comparison to Fluent. In Figure 5-8, along the horizontal midline, the results obtained slightly over-predict the temperature in comparison to both Fluent [66] and dos Santos [65] however, the trends are captured. It should be mentioned that dos Santos uses Large Eddy Simulation (LES) and hexahedral eight-node FEM and that Fluent uses second-order central differencing for diffusive flow and second-order upwinding for advection-dominated flow. The higher-order discretization employed by dos Santos [65] and Fluent may have resulted in the discrepancies seen in Figure 5-7.

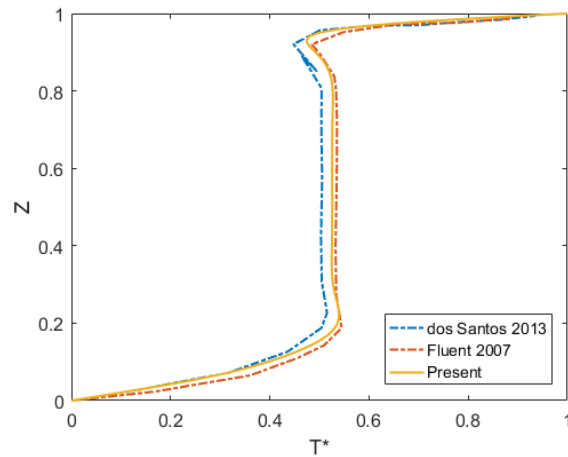


Figure 5-7 Temperature profiles for flow with $Re = 1000$ and $Pr = 1.0$ at steady-state: distribution of temperature along the vertical midline

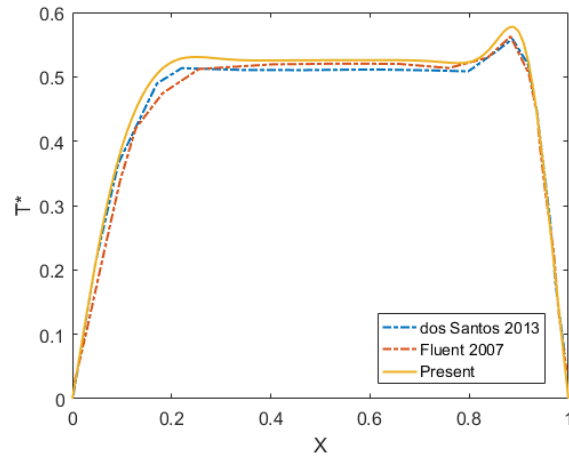


Figure 5-8 Temperature profiles for flow with $Re = 1000$ and $Pr = 1.0$ at steady-state: distribution of temperature along the horizontal midline

5.1.3 Square and Circular Obstruction, Forced Convection

The second case focuses on mixed convection in a lid-driven square cavity with an isothermally heated square blockage. The XFEM with penalization results are compared with the results from [67] using Fluent [66]. The blockage is placed centrally in the cavity with air as the working fluid ($Pr = 0.71$). Convection in the cavity is caused by the temperature gradient between the outer and inner squares and the moving lid. Using a Richardson number (Ri) of 0.1, a forced convection regime is present inside the cavity. The flow conditions are described in Figure 5-9 and the mesh size characteristics are in Table 5-4.

Table 5-4 Square obstruction, forced convection mesh size

Method	Nodes	Quadrilateral Elements
XFEM	58,081	57,600
Body – Conforming	57,602	57,121

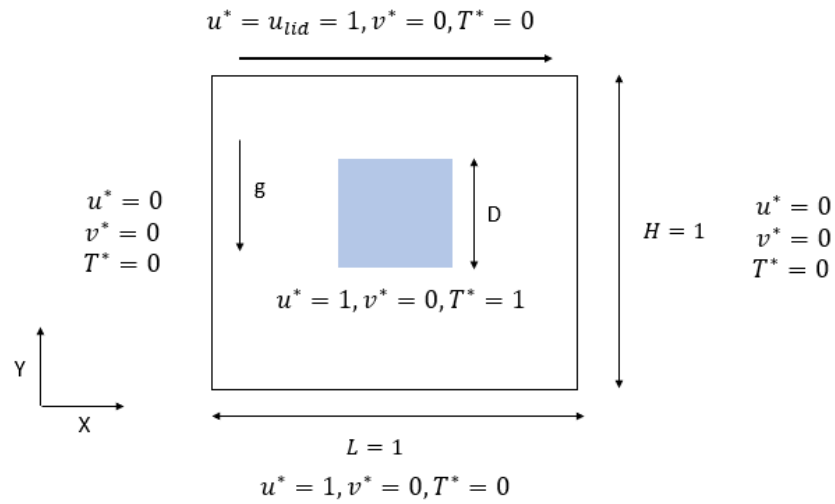


Figure 5-9 Square obstruction with forced convection: flow configuration and boundary conditions

The non-dimensional terms are defined as they were in equations (15-17), with the exception that now:

$$Y = \frac{y}{H} \quad (5.4)$$

The temperature difference $T_{max} - T_{min}$, thermal expansion coefficient α , specific heat at constant pressure c_p , reference length L , reference velocity U_{lid} and reference density ρ are non-dimensional and set to 1. In [67], the viscosity was chosen to be $\frac{1}{Re}$ And the thermal conductivity was set to $\frac{1}{Re Pr}$. The gravitational acceleration in the y-direction was chosen to be Ri . The blockage is defined by $B = \frac{D}{L}$. The mesh size characteristics are in Table 5-5.

Table 5-5 Circle obstruction, forced convection

Method	Nodes	Quadrilateral Elements
XFEM	58,081	57,600
Body – Conforming	58,144	57,482

Figure 5-10 shows the isotherms in the cavity. The flow moves clockwise, with a shift towards the right corner. This is caused by the stronger convective force, while a weaker convective force is present in the bottom two corners of the cavity. There is close accordance between the isotherms obtained with the body-conforming mesh and the isotherms obtained by [67].

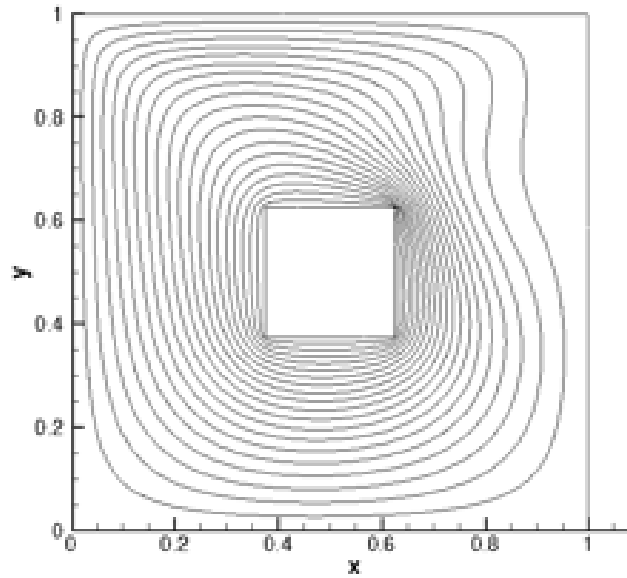


Figure 5-10 Isotherms in the cavity with central blockage placement at $Ri = 0.1$ and $B = 0.25$

With this validation, the test case was modified, making the blockage circular. The boundary conditions are identical to the ones above, the only change being the geometry now being a circle with the diameter D instead of the square length D . Figure 5-11 and Figure 5-12 show that streamlines and isotherms for body-conforming mesh match those obtained using XFEM with the penalization term.

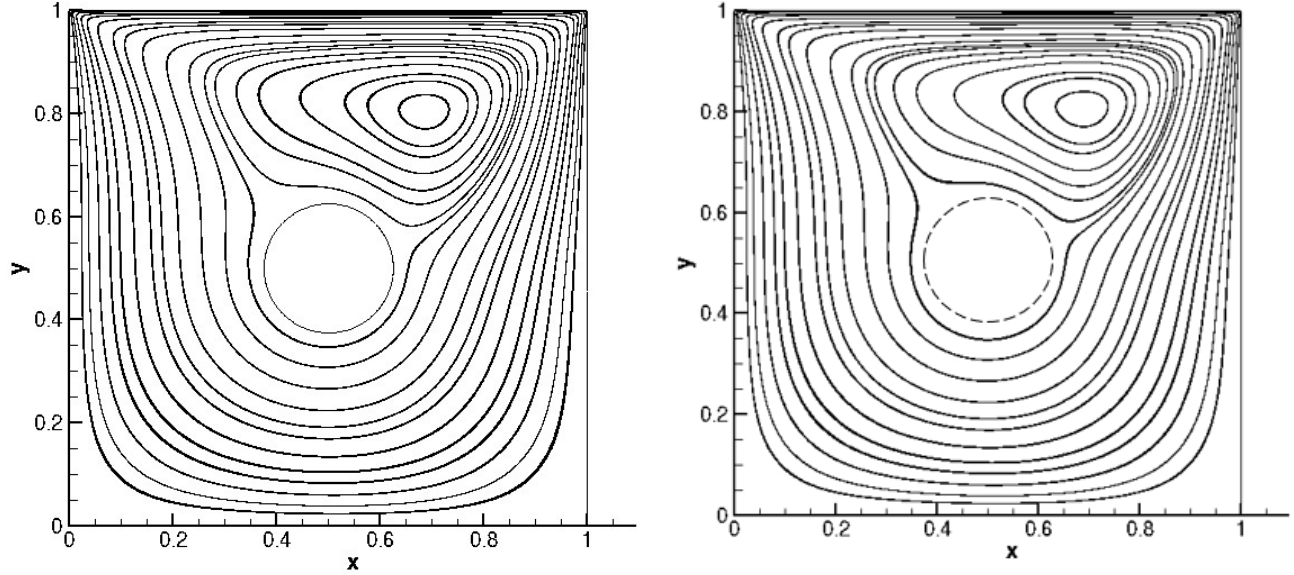


Figure 5-11 Streamlines in the cavity with central blockage placement at $Ri = 0.1$ and $B = 0.25$ with (left) body-conforming mesh (right) embedded blockage

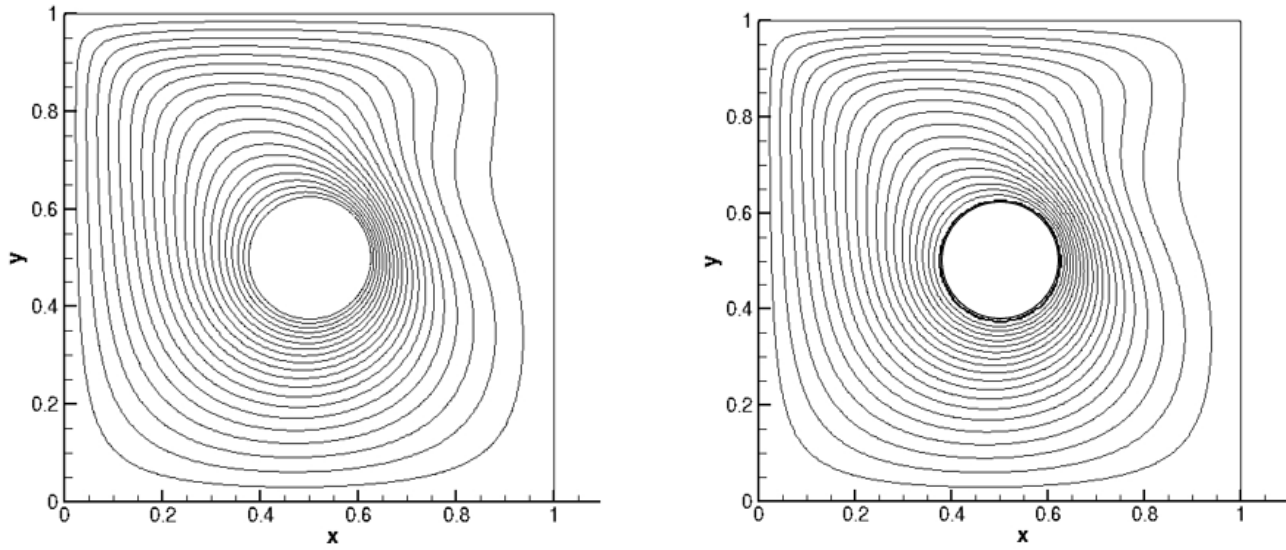


Figure 5-12 Isotherms in the cavity with central blockage placement at $Ri = 0.1$ and $B = 1/4$ with (left) body-conforming mesh (right) embedded blockage

Figure 5-13 and Figure 5-14 show the temperature profiles at the horizontal and vertical midlines. The latter figures show that the temperatures along the two midlines are identical for the body-conforming mesh and the uniform mesh with XFEM and penalization.

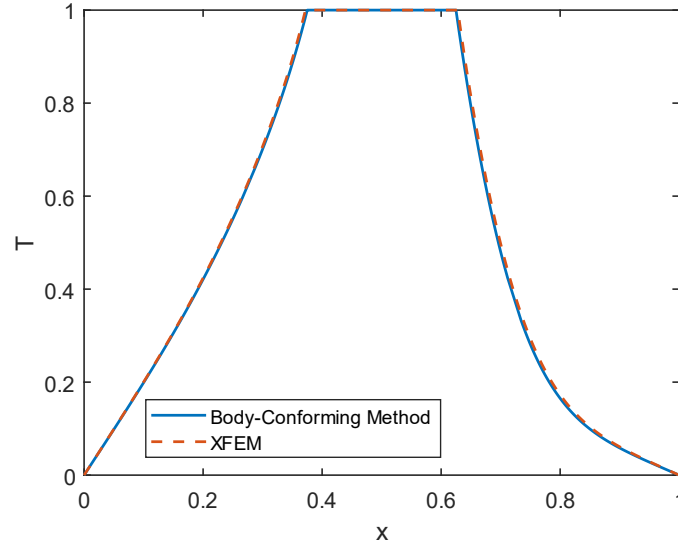


Figure 5-13 Temperature profiles in the cavity at $Ri = 0.1$ and $B = 1/4$ at horizontal midline

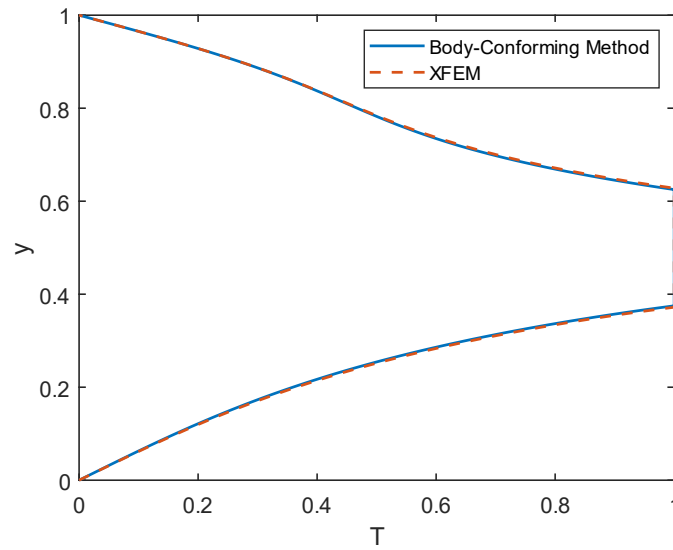


Figure 5-14 Temperature profiles in the cavity at $Ri = 0.1$ and $B = 1/4$ at vertical midline

5.2 Stefan Problem Validation

5.2.1 1D Solidification

The 1D solidification test case is a benchmark problem that simulates the Stefan problem in a semi-infinite domain. The rectangular domain is 0.1 m by 0.025 m with the solid-liquid interface 2 mm away from the left boundary, as shown in Figure 5-15. The initial temperature in the domain is 277 K and at $t = 0$ the temperature on the left boundary is lowered to 263 K. The right boundary is maintained at 277 K and the top and bottom are adiabatic (Neumann conditions).

The thermal properties are as follows: density is constant for both phases as $1000 \text{ kg}\cdot\text{m}^{-3}$, the latent heat is $8.03\cdot 10^4 \text{ J}\cdot\text{kg}^{-1}$, melting temperature of 273 K, thermal conductivity of $4.02 \text{ W}\cdot\text{m}^{-1}\cdot\text{K}^{-1}$ for the solid and $2.89 \text{ W}\cdot\text{m}^{-1}\cdot\text{K}^{-1}$ for the liquid, and a specific heat of $2.05\cdot 10^3 \text{ J}\cdot\text{m}^{-3}\cdot\text{K}^{-1}$ for the solid and $2.59\cdot 10^3 \text{ J}\cdot\text{m}^{-3}\cdot\text{K}^{-1}$ for the liquid. The nonlinear convergence criterion is set to 10^{-8} and $\beta_T = 10^7$.

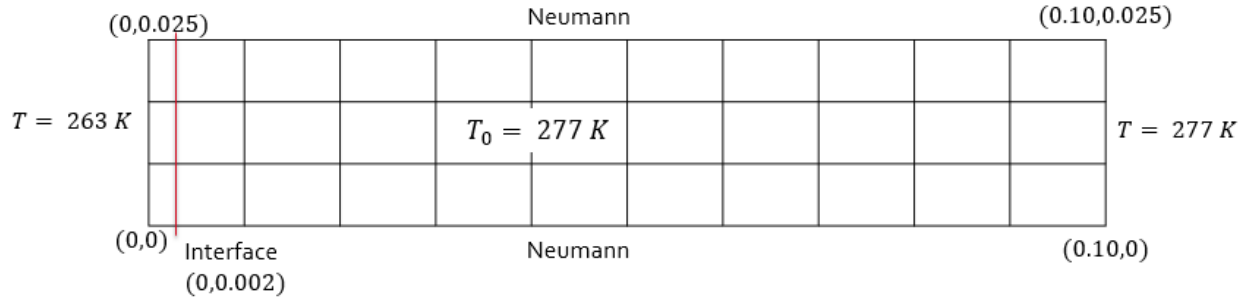


Figure 5-15 Domain setup for the 1D solidification problem

The analytical solution of the 1D solidification problem is given by:

$$x_f = 2 \lambda \sqrt{\frac{k}{(\rho c_p)_s} t} \quad (5.5)$$

The constant λ is determined by the transcendental equation:

$$\frac{e^{-\lambda^2}}{\text{erf}(\lambda)} = \frac{\frac{k_2}{k_1}(\sqrt{\eta}(T_2 - T_m)e^{-\eta\lambda^2})}{(T_m - T_1)\text{erfc}(\lambda\sqrt{\eta})} + \frac{\lambda L\sqrt{\pi}}{c_1(T_m - T_1)} \quad (5.6)$$

where $\eta = \frac{\alpha_s}{\alpha_l}$, and $\alpha_s = \frac{k_1}{c_1}$ is the thermal diffusivity of the solid phase and α_l is the thermal diffusivity of the liquid phase. T_1 is the temperature of the solid wall and T_2 is the temperature of the liquid wall. λ is found to be 0.3073.

The interface location is given in Figure 5-16, with a good comparison against Martin *et al.* [68] who used a constant per element Lagrange field in their XFEM implementation. The present results show an increase in accuracy that comes from using the modified enrichment scheme in comparison to the Lagrange multiplier scheme. They are in better agreement to the known analytical solution, especially at the beginning where the interface location closely matches the analytical solution. The deviation from the analytical interface position at the end is due to the influence of using a finite domain to approximate an infinite domain problem. Increasing the domain length should give results in closer accordance with the analytical for the last 2000 seconds of the simulation.

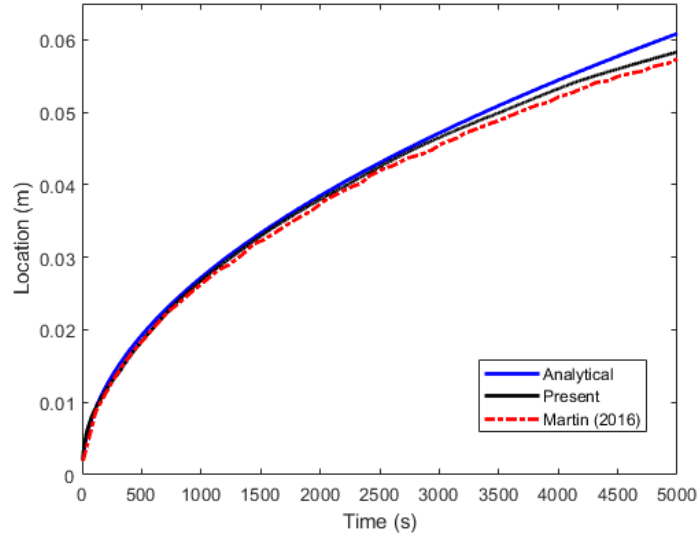


Figure 5-16 Interface location for 1D solidification problem

5.2.2 Infinite Corner Solidification

The infinite corner or the two-dimensional square corner problem is another benchmark test case used to validate the implementation of the Stefan condition. The 2 m by 2 m square domain has the interface initially at 0.035 m from the left and bottom boundaries. The domain is initially fully liquid with an initial temperature of 273.3 K. The left and bottom boundaries are then lowered at $t > 0$ to 272 K and the other two boundaries are adiabatic (Neumann conditions). The problem simulates a liquid domain solidifying as the left and bottom boundaries cool down the liquid causing it to change back into solid.

For the liquid and solid, the density is $1 \text{ kg}\cdot\text{m}^{-3}$, the thermal conductivity is $1 \text{ W}\cdot\text{m}^{-1}\cdot\text{K}^{-1}$ and the specific heat is 1 J/K . The latent heat is 0.25 J/kg and the melting temperature is 273 K . Given these material properties, the lambda coefficient for the analytical solution is calculated and found to be 0.70766. Equation (5.7) is then used to determine the analytical non-dimensional interface location. The nonlinear convergence criterion is set to 10^{-8} and $\beta_T = 10^7$. The non-dimensional interface position can be determined using $C = 0.159$, $m = 5.02$ and $\lambda = 0.70766$ and solved using the following relation:

$$Y(X) = \left(\lambda^m + \frac{C}{(x')^m - \lambda^m} \right)^{\frac{1}{m}} \quad (5.8)$$

$$X = \frac{x_\Gamma}{\sqrt{4\alpha t}} \quad (5.9)$$

$$Y = \frac{y_\Gamma}{\sqrt{4\alpha t}} \quad (5.10)$$

Figure 5-17 compares the interface position result with the analytical and the numerical results obtained by Martin *et al.* [68] using identical 28x28 grids. The present methodology is in close agreement with the analytical solution. The modified abs-enrichment scheme gives better accordance to the analytical than the Lagrange multiplier formulation used by Martin, with excellent concurrence on the interface location of the edges of the solidifying infinite square. The results show that a coarse mesh is sufficient to accurately capture the interface motion over time as the liquid freezes.

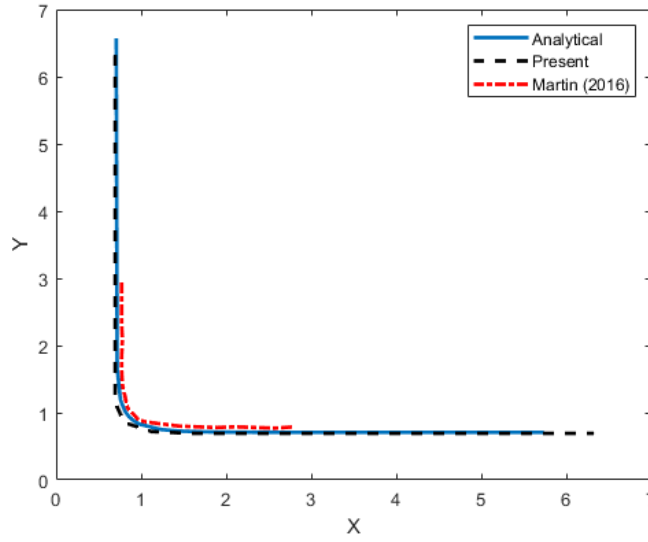


Figure 5-17 Non-dimensional interface location comparison for an infinite corner at 0.025 sec

The test case is also shown with three other mesh sizes. Again, the non-dimensional interface location is plotted in Figure 5-18, with the three chosen mesh sizes. The results show that even a coarse mesh of 20x20 gives good results, with an increase in accuracy obtained by refining the mesh, showing that XFEM formulation can produce highly accurate results without the need of body-conforming meshes or very fine meshes. An additional area of interest is the corner of the infinite square which becomes more curved as the cold temperature from the left and bottom walls freezes the square corner of liquid water. This is a region where heat flux variations could lead to erroneous solutions, as stated by Martin *et al.* [68], but the present methodology shows close agreement with the analytical position, even with the corner.

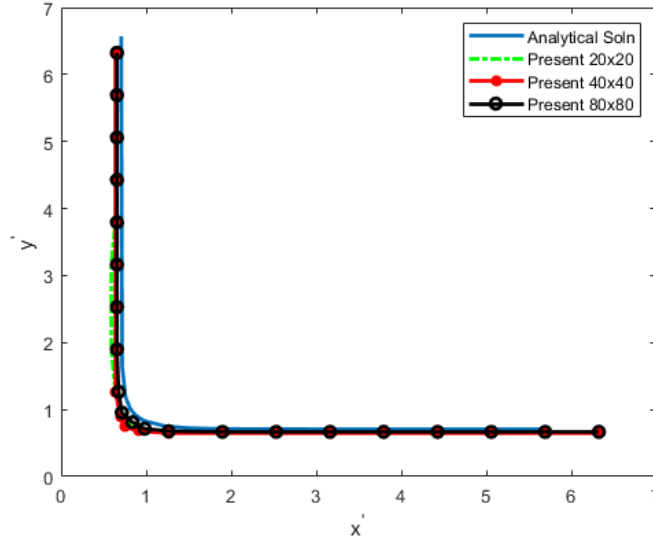


Figure 5-18 Non-dimensional interface location for an infinite corner at 0.025 sec for three mesh refinements

5.2.3 Frank Sphere

The Frank sphere test case was chosen to look at the convergence of the methodology, by examining the temperature of the domain. The solid region is, for a 2D case, a circle of radius $R = s_0 t^{\frac{1}{2}}$ where s_0 is the initial radius, and the temperature is given by:

$$T(r, t) = T(s) = \begin{cases} T_{\infty} \left(1 - \frac{F(s)}{F(s_0)} \right), & s > s_0 \\ 0, & s \leq s_0 \end{cases} \quad (5.11)$$

Here $r = \sqrt{x^2 + y^2}$, the similarity variable is $s = r/t^{\frac{1}{2}}$, and T_{∞} is a given undercooling. In the case above, the function $F(s)$ is a similarity solution of the heat equation and is defined as follows:

$$F(s) = E_1 \left(\frac{1}{4} s^2 \right) \quad (5.12)$$

The initial radius, s_0 was 0.25 and the given undercooling, T_{∞} was -0.05709187113307. The boundaries are adiabatic (Neumann conditions), and the material properties of the fluid and solid are the same. All material properties are non-dimensional, with a density, thermal conductivity and specific heat of 1. The exception is the latent heat which is 0.25 and a melting temperature of

0. Given these material properties, the lambda coefficient for the analytical solution can be calculated to be 0.125. The nonlinear convergence criterion is set to 10^{-8} and $\beta_T = 10^7$.

The convergence is monitored by comparing the L_2 norm of the residual of temperature, $\|R\|_{L_2}$, in the domain. This is computed as:

$$\|R\|_{L_2} = \sqrt{\sum_{k=1}^n |R_i|^2} \quad (5.13)$$

where R_i is the residual of temperature at each node. The convergence obtained from three increasingly fine meshes is found in Table 1, where h_{ele} is the mesh size and EOC is the order of convergence.

Table 5-6 Frank sphere convergence

Grid	h_{ele}	$\ R\ _{L_2}$	EOC
90x90	0.133	$2.14 \cdot 10^{-5}$	—
180x180	0.0666	$1.13 \cdot 10^{-5}$	0.926
360x360	0.0333	$5.82 \cdot 10^{-6}$	0.937

From the Frank sphere's convergence test, and the results in Table 1, the present methodology has an order of convergence of 1. Since the Stefan problem involves the calculation of a sharp heat flux jump which is first-order, the entire simulation is limited to an order of accuracy of 1. However, the results presented in this test case show that the XFEM-LSM is highly capable of dealing with free boundaries and giving accurate results without the need for highly refined meshes. This test case validated the Stefan condition implementation and demonstrated the order of convergence of the code.

5.3 Coupled Stefan and Hydrodynamics Validation

The developed framework is tested using several benchmark cases. The Stefan condition approach is verified using 1D solidification, infinite corner solidification, and Frank sphere. The Stefan problem with hydrodynamics is validated using flow over a cylinder and infinite corner solidification with non-constant density between phases.

5.3.1 Flow over Cylinder

The steady-state flow over a cylinder problem can be used to validate the INS formulation with penalization. The domain is 1 m by 0.5 m, with the cylinder centered at (0.4, 0.25) m with a radius of 0.05 m. The material properties are a density of $1000 \text{ kg}\cdot\text{m}^{-3}$ and a dynamic viscosity of $10 \text{ kg}\cdot\text{m}^{-1}\cdot\text{s}^{-1}$. The boundary conditions involve an open left boundary where the pressure is set to 0 Pa and the other three boundaries set to $u_i = (-0.1, 0) \text{ m/s}$. The nonlinear convergence criterion is set to 10^{-8} and $\beta_u = \beta_T = 10^7$.

Figure 5-19 shows a plot of the velocity contours in the domain, and Figure 5-20 shows the velocity magnitude at the midline and compares the results from the present methodology with those from Martin [69] and COMSOL, as done by Martin using the grid found in [69] of 2331 elements.

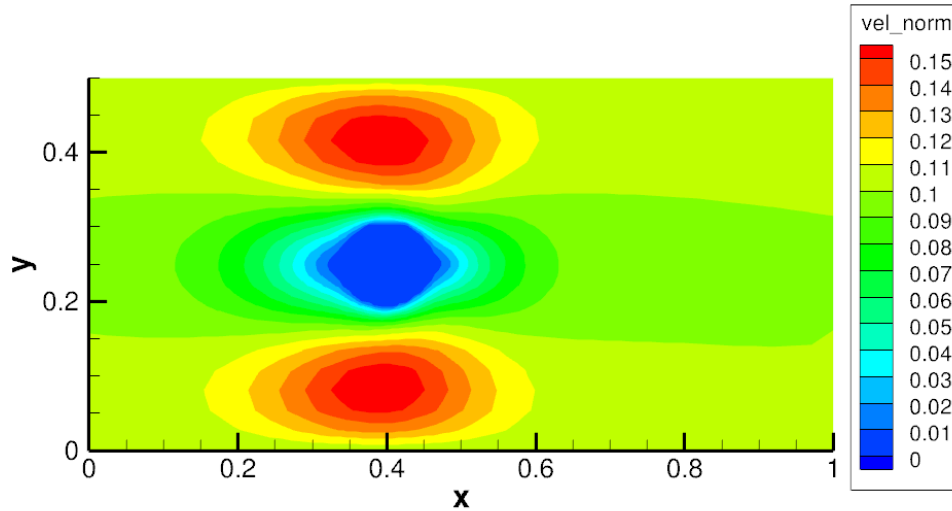


Figure 5-19 Velocity contours for flow over a cylinder

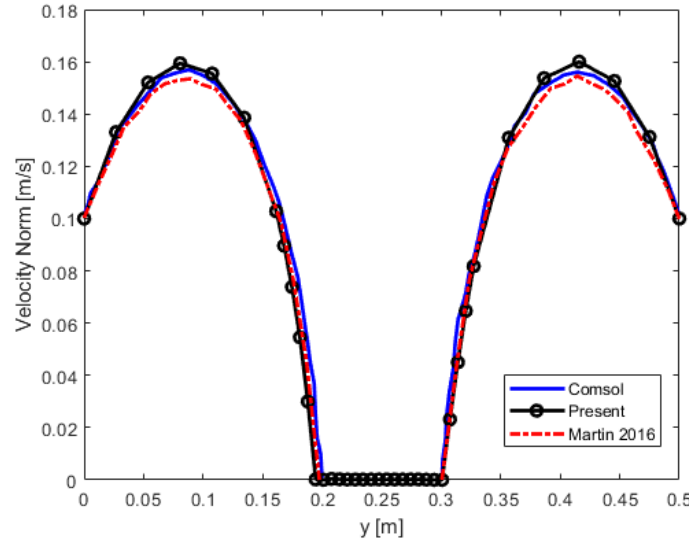


Figure 5-20 Velocity norm at midline for flow over a cylinder

Figure 5-20 shows that the present methodology is in excellent agreement with both Martin [69] and COMSOL [69], with a complete overlap for the majority of the midline. The XFEM implementation shows a closer concurrence to COMSOL which uses an adaptive mesh to follow the moving interface. Overall, the implementation correctly enforces the no-slip boundary condition.

5.3.2 Solidification with Natural Convection

This test case corresponds to a 0.05 m by 0.05 m cavity driven by natural convection leading to the solidification of an aluminum alloy in the cavity. The fluid is initially at rest and the temperature in the cavity is 710 °C. The left wall is set to 710 °C and the right wall to 610° C. The cavity walls are no-slip walls. The material properties are as follows: density $\rho = 2500 \text{ kg}\cdot\text{m}^{-3}$, dynamic viscosity $\mu = 0.025 \text{ kg}\cdot\text{m}^{-1}\cdot\text{s}^{-1}$, heat capacity $c = 1046 \text{ J}\cdot\text{kg}^{-1}\cdot\text{°C}^{-1}$, thermal conductivity $k = 104.6 \text{ W}\cdot\text{m}^{-1}\cdot\text{°C}^{-1}$, latent heat $L = 4\cdot 10^6 \text{ J}\cdot\text{kg}^{-1}$, coefficient of thermal expansion $\alpha = 4\cdot 10^{-5} \text{ °C}^{-1}$, and a gravitational acceleration $g = 9.81 \text{ m}\cdot\text{s}^{-2}$. The domain is a 20x20 grid, the time step is 0.01 s and the simulation is carried out for 920 s. The nonlinear convergence criterion is set to 10^{-8} and $\beta_u = \beta_T = 10^{10}$.

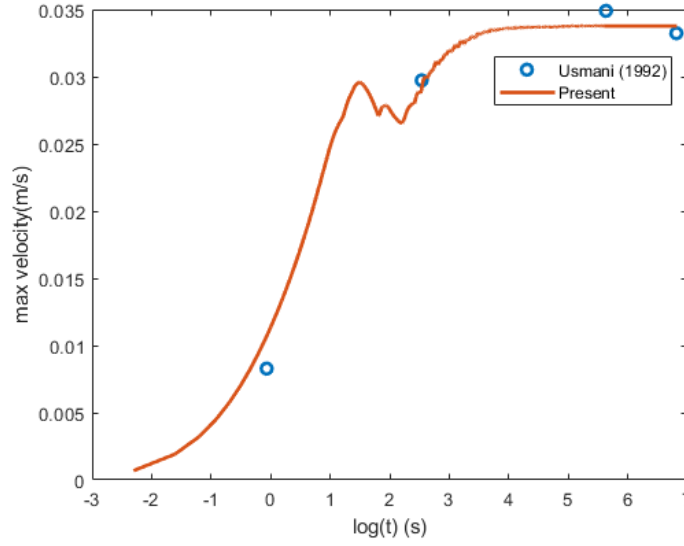


Figure 5-21 Maximum velocity in a thermal cavity with natural convection

The time history of the maximum velocity in the thermal cavity is compared with the results from Usmani *et al.* [70] in Figure 5-21. In order to model the isothermal phase change at the interface, he used a fictitious heat flow FE method that lumps the latent heat available at the nodes and releases it as an internal heat source. The present methodology is in good agreement, coming within 5% of the scarce data points of Usmani. This test case validates the XFEM implementation by showing that the two different techniques to model the phase change constraint are in close accordance with each other.

5.3.3 Tin Melting with Non-constant Density

The tin melting front problem describes the interaction between heat transfer and the influence of enforced flow due to the density jump between the liquid and solid phase tin. Due to the melting of the tin and the fact that liquid tin is incompressible, penetration must be allowed. Hence the top of the cavity is set to $P = 0$, an open boundary. The density difference between the phases means that additional liquid will flow into the liquid phase from the interface.

The domain is 0.1 m x 0.1 m with liquid tin on the left and solid tin on the right with the initial liquid-solid interface located at $x = 0.06$ m. The cavity has no-slip boundary conditions applied to the three remaining walls. The left wall is set to 530 °C and the right wall is set to 503 °C, with a melting temperature of 505 °C. The material properties of tin are as follows: density of the solid

phase $\rho_s = 7500 \text{ kg}\cdot\text{m}^{-3}$, density of the liquid phase $\rho_l = 7030 \text{ kg}\cdot\text{m}^{-3}$, dynamic viscosity $\mu = 6\cdot 10^{-3} \text{ kg}\cdot\text{m}^{-1}\cdot\text{s}^{-1}$, specific heat capacity $c_p = 200 \text{ J}\cdot\text{kg}^{-1}\cdot^\circ\text{C}^{-1}$, thermal conductivity $k = 60 \text{ W}\cdot\text{m}^{-1}\cdot^\circ\text{C}^{-1}$, latent heat of fusion $L = 6\cdot 10^4 \text{ J}\cdot\text{kg}^{-1}$, and a thermal expansion coefficient $\alpha = 2.67\cdot 10^{-4} \text{ }^\circ\text{C}^{-1}$. The nonlinear convergence criterion is set to 10^{-8} and $\beta_u = \beta_T = 10^{10}$.

The interface location is given at 200 seconds, 400 seconds and at the end at 750 seconds, as shown in Figure 5-22. The results from the present methodology are compared with those from Li *et al.* [31] who use a Stokes formulation for the fluid flow calculation that is limited to low Re . The interface location is identical for the three time instants, although the presented approach does have some slight wiggling at the bottom of the domain. This is seen more prominently at 400 seconds but is nearly fully corrected by the end at 750 seconds.

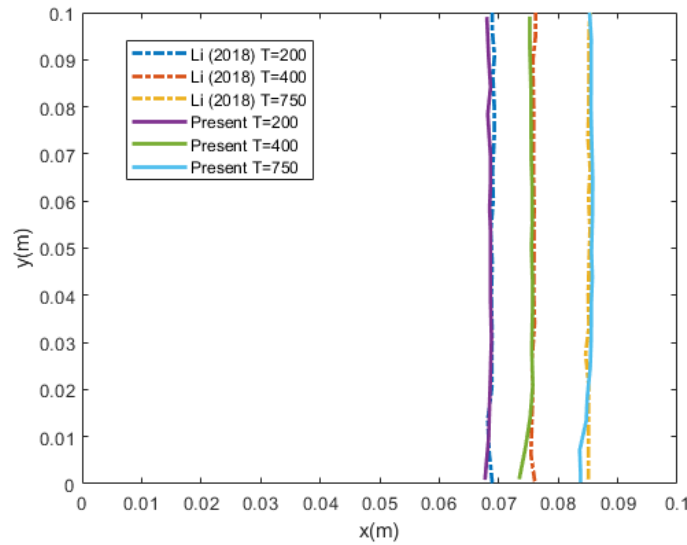


Figure 5-22 Interface location of tin melting at $t=200 \text{ s}$, $t=400 \text{ s}$, and $t=750 \text{ s}$

In Figure 5-23 through Figure 5-25, the centerline temperature in the domain is plotted and compared. Once more, the present methodology is in good concurrence with the results from Li *et al.* [31]. The temperature is monotonically decreasing in the domain since there is no natural convection in this problem, with only the density difference causing the motion of the interface as the material melts. Since the motion of the interface is near the order of 10^{-5} m/s , this weak flow has a negligible influence on the temperature distribution in the domain.

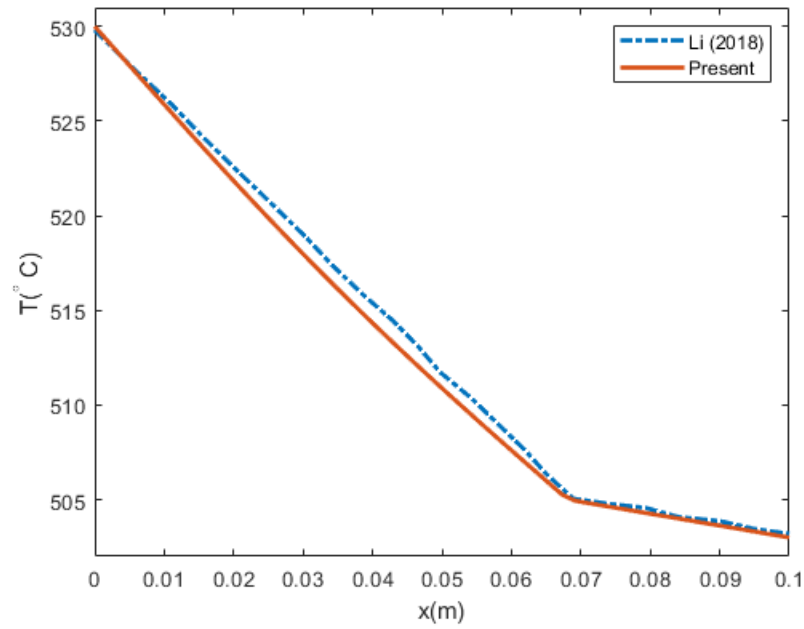


Figure 5-23 Temperature of tin melting at centerline at $t=200s$

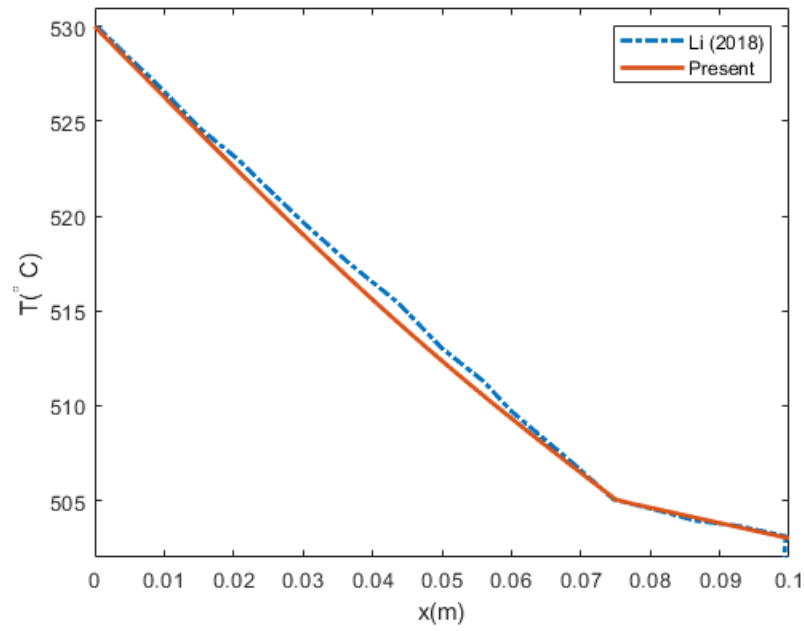


Figure 5-24 Temperature of tin melting at centerline at $t=400s$

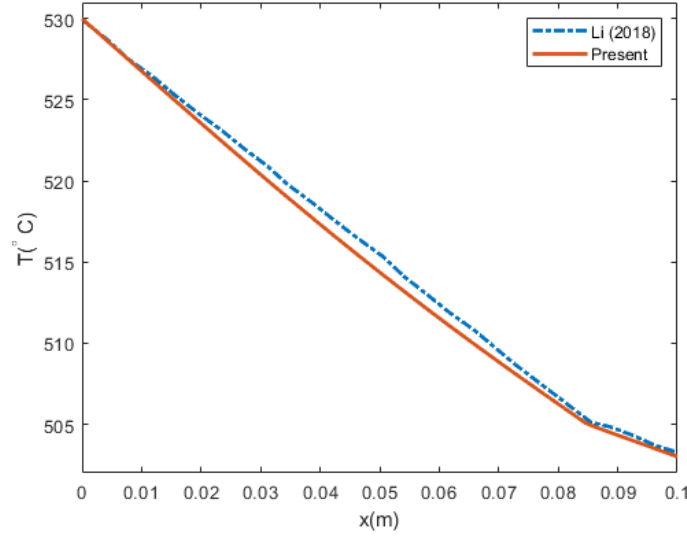


Figure 5-25 Temperature of tin melting at centerline at $t=750s$

5.3.4 Ice Cylinder Melting in High Re Flow

Having demonstrated the validity and accuracy of the present approach against benchmark test cases, the aim of the final case is to demonstrate its capabilities to model a practical phase change problem for a high Re flow. It involves the melting of an ice cylinder in a rectangular domain that is 0.1 m by 0.02 m with top and bottom boundaries set as no-slip adiabatic walls. The left boundary is heated to 283 K and a velocity of 0.005 m/s is prescribed in the x -direction, while the right boundary is adiabatic and an open boundary where pressure is set to 0 Pa.

An ice cylinder with a radius of 0.005 m is centered at (0.02, 0.1). The physical properties of the liquid are as follows: density of $999 \text{ kg}\cdot\text{m}^{-3}$, dynamic viscosity of $1.3975\cdot 10^{-3} \text{ kg}\cdot\text{m}^{-1}\cdot\text{s}^{-1}$, thermal conductivity of $0.5797 \text{ W}\cdot\text{m}^{-1}\cdot\text{K}^{-1}$, specific heat of $4.199\cdot 10^3 \text{ J}\cdot\text{kg}^{-1}\cdot\text{K}^{-1}$. The material properties of the solid are as follows: a density of $916.7 \text{ kg}\cdot\text{m}^{-3}$, dynamic viscosity of $1.793\cdot 10^{-3} \text{ kg}\cdot\text{m}^{-1}\cdot\text{s}^{-1}$, thermal conductivity of $2.18 \text{ W}\cdot\text{m}^{-1}\cdot\text{K}^{-1}$, and a specific heat of $2.093\cdot 10^3 \text{ J}\cdot\text{kg}^{-1}\cdot\text{K}^{-1}$. The melting temperature is 273 K and the latent heat of fusion is $3.44\cdot 10^5 \text{ J}\cdot\text{kg}^{-1}$. The nonlinear convergence criterion is set to 10^{-8} and $\beta_u = \beta_T = 10^{10}$.

Figure 5-26 shows the time history of the interface position and shape on a 108x52 grid. Subsequently, Figure 5-27 through Figure 5-31 show the evolution of the velocity magnitude and Figure 5-32 through Figure 5-36 show that of the temperature contours, as the ice melts.

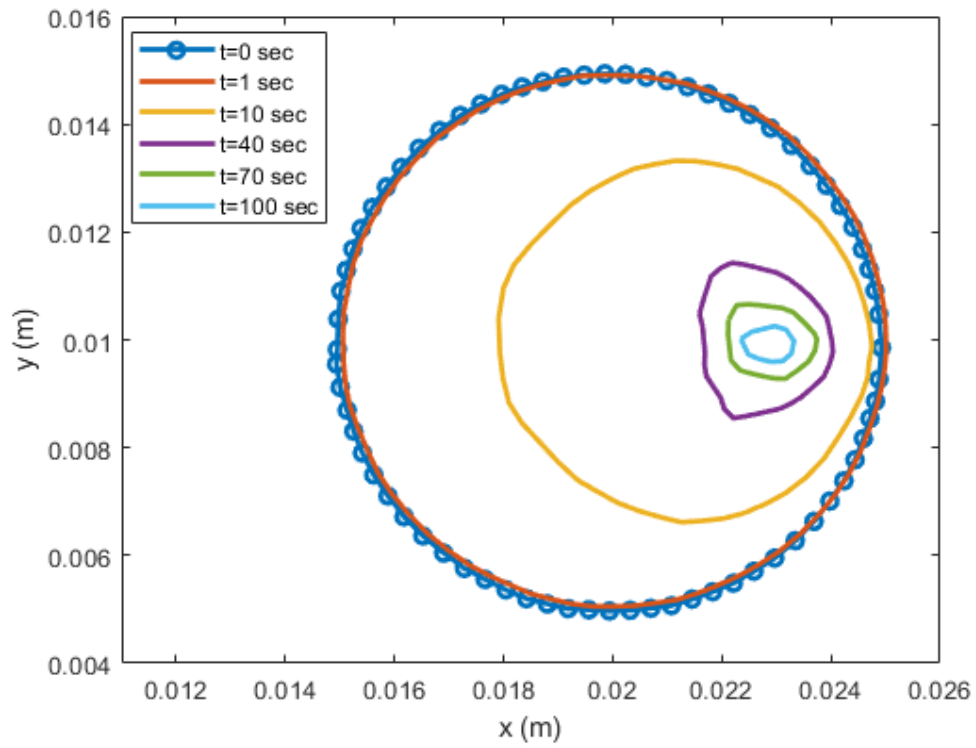


Figure 5-26 Interface shape and position of melting cylinder in high Re flow

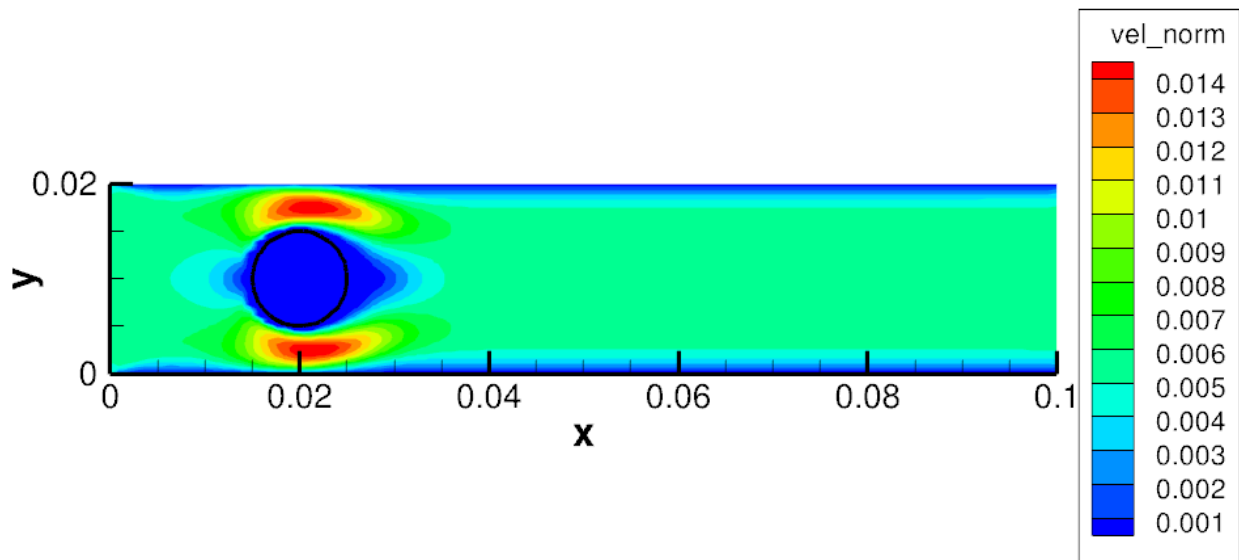


Figure 5-27 Velocity contours (in m/s) of melting cylinder in high Re flow, at $t = 1$ sec

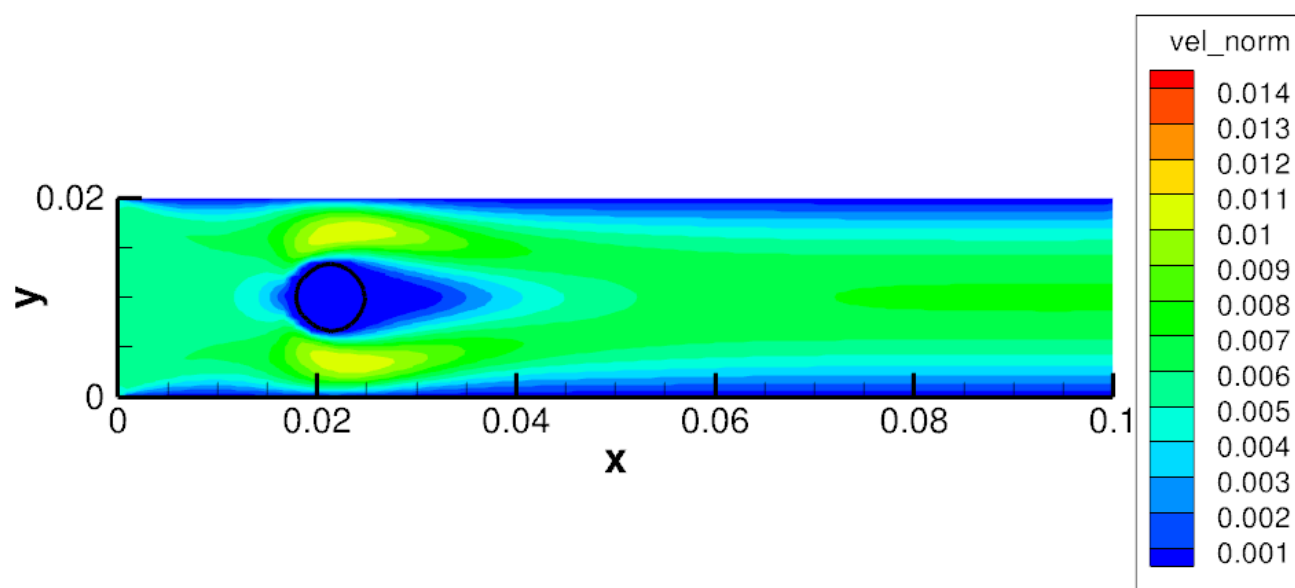


Figure 5-28 Velocity contours (in m/s) of melting cylinder in high Re flow, at $t = 10$ sec

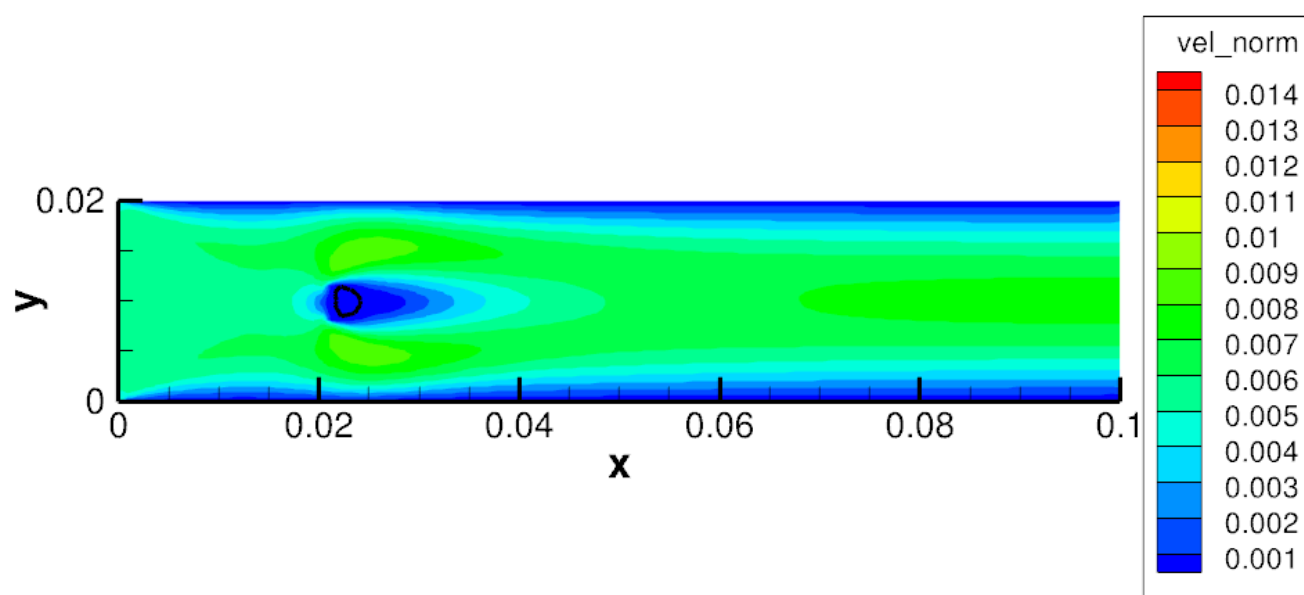


Figure 5-29 Velocity contours (in m/s) of melting cylinder in high Re flow, at $t = 40$ sec

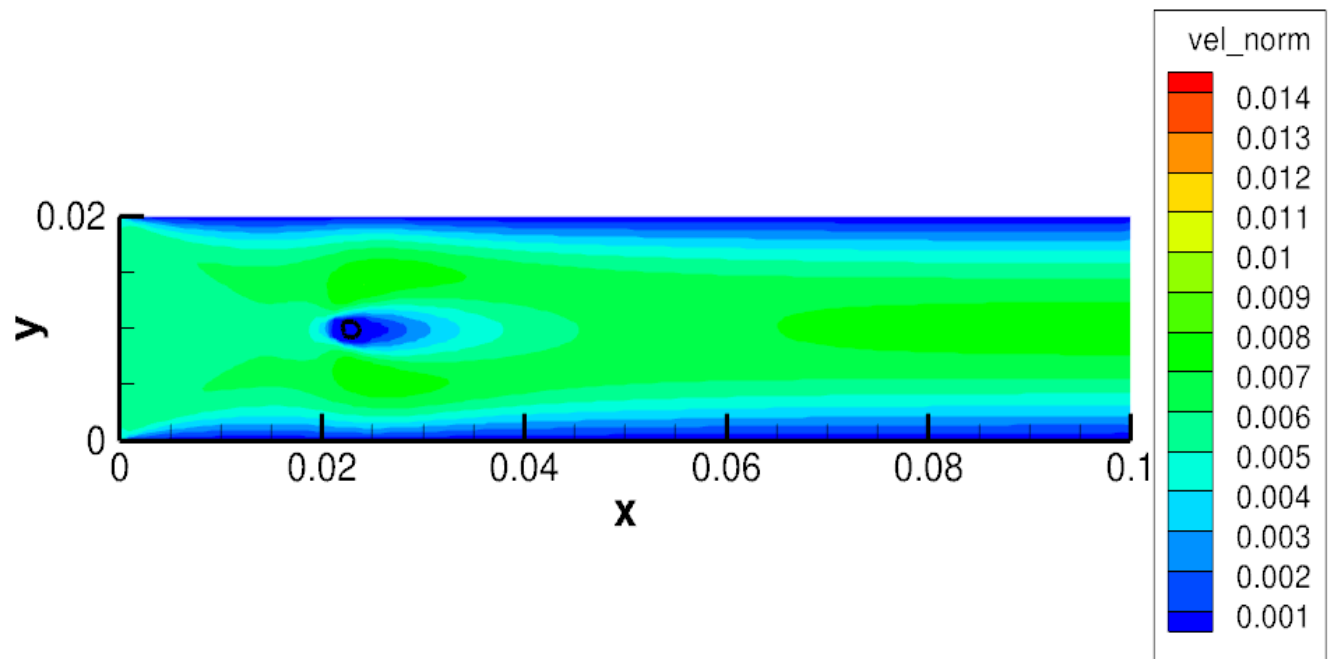


Figure 5-30 Velocity contours (in m/s) of melting cylinder in high Re flow, at $t = 70$ sec

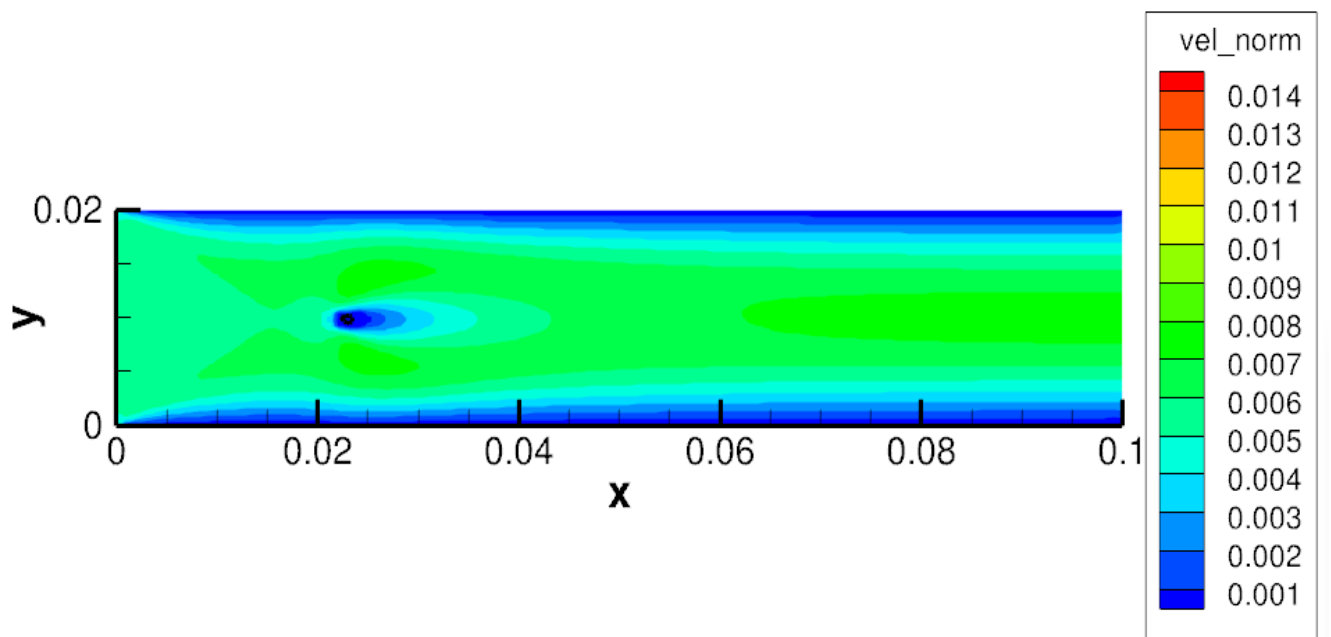


Figure 5-31 Velocity contours (in m/s) of melting cylinder in high Re flow, at $t = 100$ sec

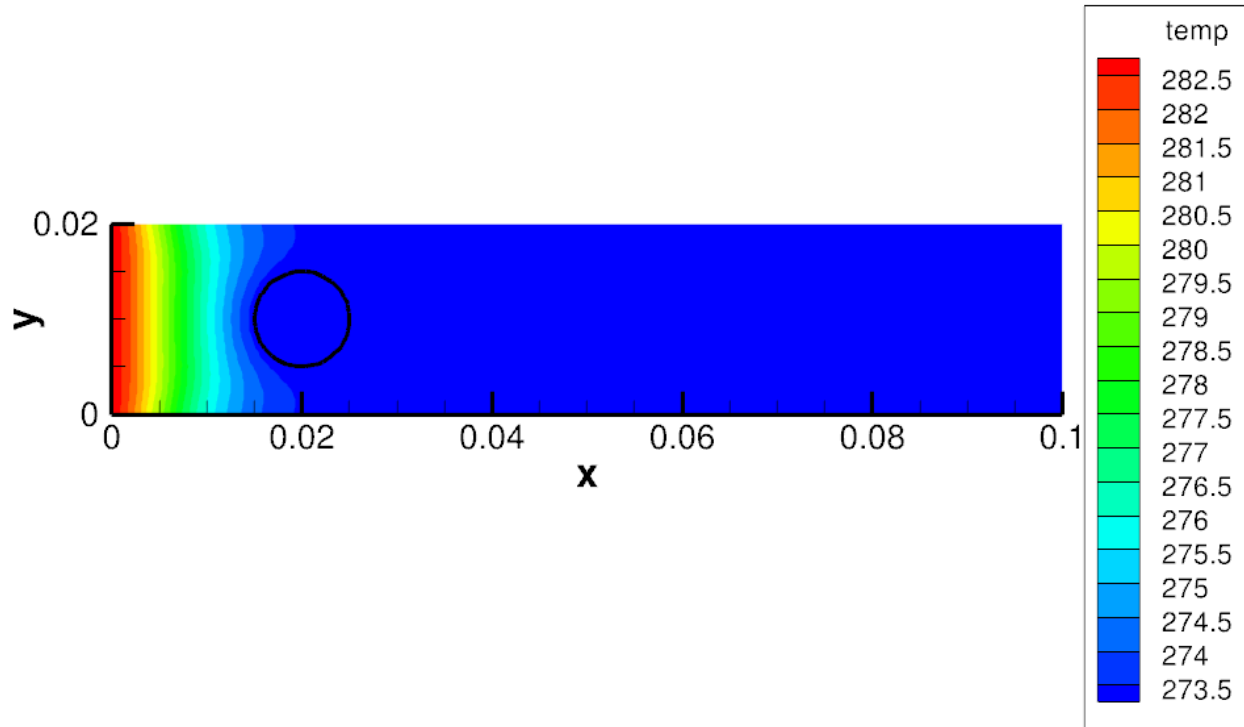


Figure 5-32 Temperature contours (in K) of melting cylinder in high Re flow, at $t = 1$ sec

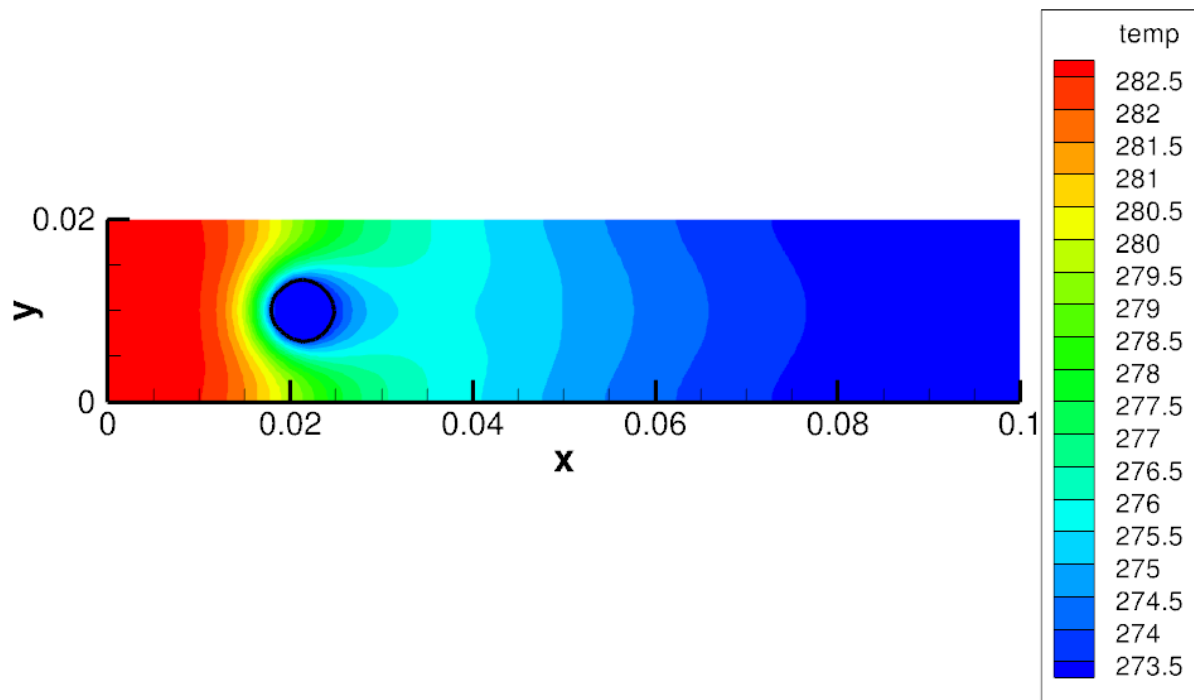


Figure 5-33 Temperature contours (in K) of melting cylinder in high Re flow, at $t = 10$ sec

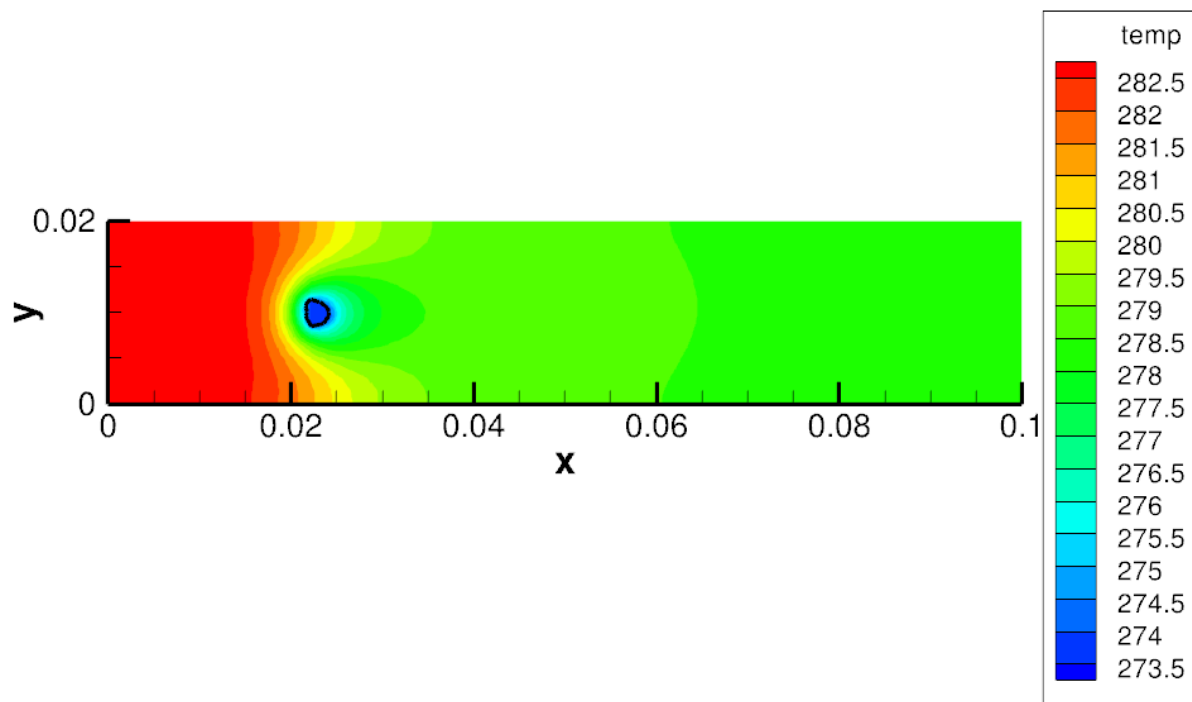


Figure 5-34 Temperature contours (in K) of melting cylinder in high Re flow, at $t = 40$ sec

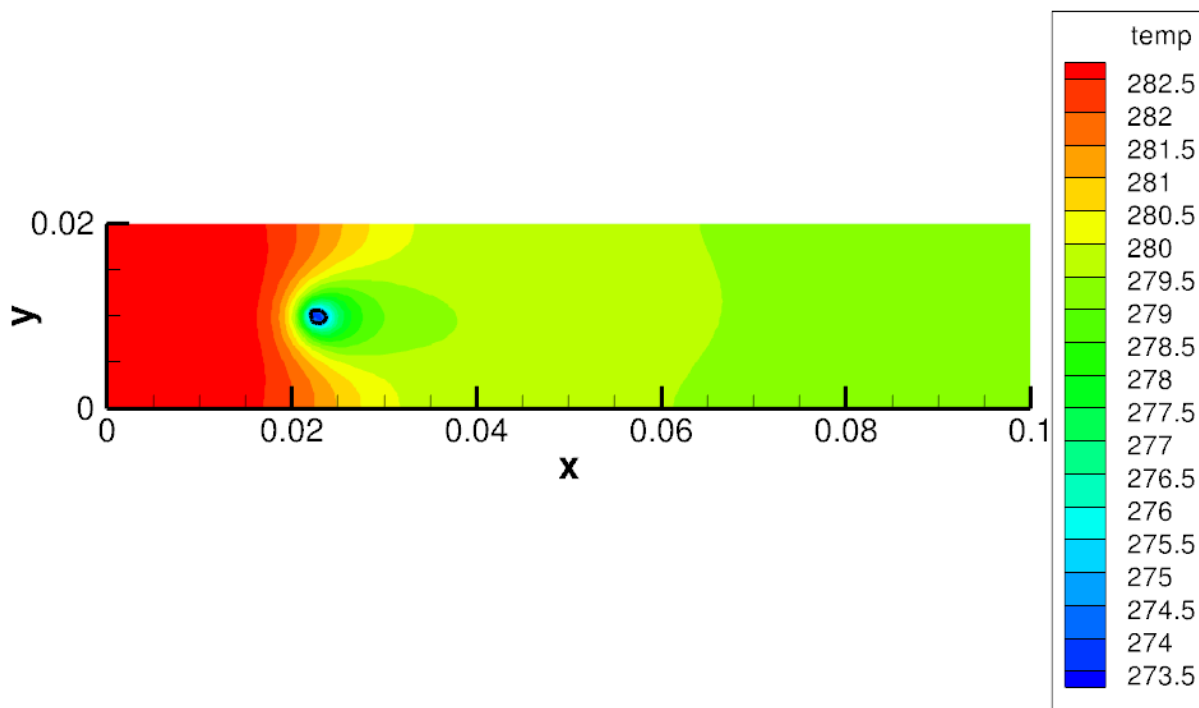


Figure 5-35 Temperature contours (in K) of melting cylinder in high Re flow, at $t = 70$ sec

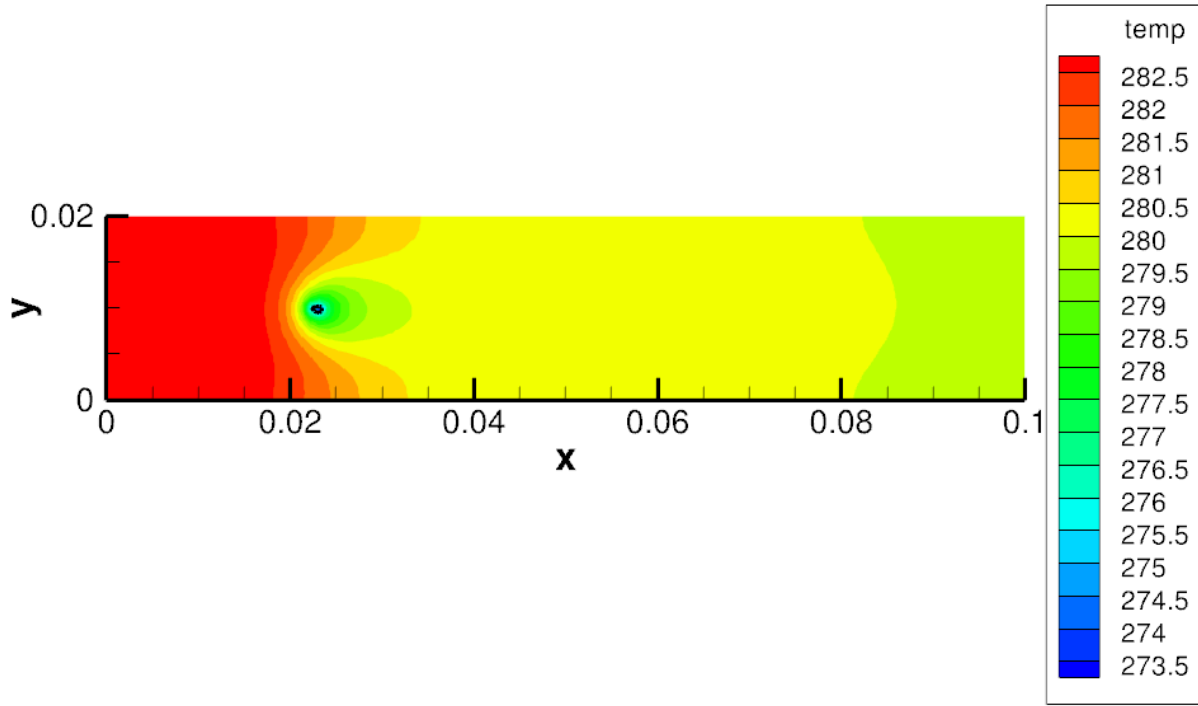


Figure 5-36 Temperature contours (in K) of melting cylinder in high Re flow, at $t = 100$ sec

The fluid/solid interface changes from a circular shape to an oval and the solid area is reduced 200-fold in 100 seconds. The fluid motion around the ice cylinder increases the heat flux at the interface and melting is first observed at the front of the cylinder and then at the top and bottom leading to the slightly oval shape seen for $t > 60$ sec in Figure 5-26. The melting cylinder results thus show the ability of the present methodology to handle high Re flows, concurrently with phase change.

6 Conclusion

Due to the current limitations in simulating in-flight icing with SLD that result from the use of empirical data to represent an ensemble of droplets, the thesis focuses on implementing a methodology that is leading to the study of droplet physics on a single droplet and providing high fidelity information to improve current commercial codes. The thesis does this by expanding on the current capabilities of a multiphase flow solver and allowing for FSI and solidification. The loosely-coupled framework for solving the hydrodynamics and thermodynamics equations has been presented. The Stefan problem can be simulated using the implemented heat flux evaluation

for the Stefan condition. The hydrodynamics are solved with Brinkman penalization in order to simulate the rigid body motion of the solid within a fluid domain. The loosely-coupled approach proves to be an efficient framework for the multiphase code.

It has been shown through several test cases that the present methodology is effective for the simulation of fluid-solid interaction as well as phase change. Firstly, the FSI implementation has been validated using several benchmark cases. No noticeable differences are seen between body-conforming mesh solutions and the XFEM penalization solutions. This demonstrates the ability of the Brinkman penalization to simulate the fluid-structure boundary, with and without convection. Subsequently, the implementation of the Stefan condition enables the simulation of solidification/melting test cases, which accurately model the interface progression as phase change occurs. XFEM allows the use of a coarse mesh that can capture the free boundary interface in the solidification or melting of materials. The enforcement of various physical constraints is effectively achieved by the penalty method.

The presented approach has led to contributions that have improved the capabilities of the multiphase solver. Firstly, the enrichment scheme is in better agreement with analytical solutions than FE methods, as has been demonstrated in the 1D and 2D solidification test cases. Secondly, the velocity boundary condition in the tin melting case with non-constant density shows the ability to capture density jump at the interface. Lastly, the final test case confirms that the XFEM code is robust in solving high Re flows. The ice cylinder melts in a domain with a Re of 700 in 100 seconds, illustrating the rapid phase change process that occurs due to heat conduction and convection. The current work has implemented planar solidification as present in SLD, but the simulation of full SLD impingement and solidification will further require the addition of the physics of nucleation and dendrite formation. The objective of expanding the capabilities of the multiphase solver to allow for FSI and phase change are shown and achieved in this thesis.

6.1 Future Work

The larger goal of the research would be to continue to develop the phase change component to allow for the simulation of nucleation points and dendrite formation. With the addition of these two stages of solidification, the necessary components, nucleation, dendrite formation, and planar solidification, would be present and allow for the accurate modeling of SLD solidification. This

would require a stochastic solver to account for the possible nucleation points and a more complex dendrite formation model. Implementation of the former could look at differences resulting from heterogeneous versus homogeneous nucleation and comparing the speed of solidification for SLD and non-SLD. The latter would make use of the Gibbs-Thompson relation for the temperature at the interface, which is now solved in addition to the Stefan condition, to give rise to dendrites. The relation is expressed as:

$$T = T_m - \epsilon_c \kappa - \epsilon_v V \quad (6.1)$$

where ϵ_c and ϵ_v are the surface tension coefficient and kinetic mobility coefficient, respectively, and κ is the curvature of the propagating interface. Both ϵ_c and ϵ_v signify the anisotropic strength which results in more dendrites when ϵ is large.

Another area of interest would be looking at the effects of aerodynamic shear flow on the process of solidification. When aircraft surfaces are cold, the SLD that are known to splash and bounce are also likely to have their final ice shape determined by the aerodynamic shear present during the solidification process. The instability of the shear-driven flow freeze could cause feathering and accretion models would need to be developed to accurately model such phenomena. Hence, exploring the effects of shear driven flow on dendrite formation and planar solidification should also be conducted through some high-speed impact and solidification test cases.

Ultimately, more experimental data would be necessary to make sure that the SLD model is accurate and a parametric study could provide the additional data for commercial and non-commercial CFD codes. The resulting work would cover multiphase flows that can handle FSI, the solid-liquid-gas triple-point, as well as SLD solidification and melting, at aeronautical speeds.

7 References

- [1] F.A.A, "Airworthiness standards: transport category airplanes, in Appendix C to Part 25, Title 14," Admt. 25-140, 79 FR 65528: 553-560, 2011.
- [2] F.A.A, "Airworthiness standards: transport category airplanes, in Appendix O to Part 25, Title 14," Amdt. 25-140, 79 FR 65528: 629-639, 2014.
- [3] R. Honsek, W. G. Habashi and M. S. Aubé, "Eulerian modeling of in-flight icing due to supercooled large droplets," *Journal of Aircraft*, vol. 45, no. 4, pp. 1290-1296, 2008.
- [4] D. Bilodeau, W. G. Habashi, M. Fossati and G. S. Baruzzi, "Eulerian modeling of supercooled large droplet splashing and bouncing," *Journal of Aircraft*, vol. 52, no. 2, pp. 1611-1624, 2015.
- [5] W. G. Habashi, "Recent advances in CFD for in-flight icing simulations," *Japan Society of Fluid Mechanics*, vol. 28, no. 2, pp. 99-118, 2009.
- [6] G. Luxford, "Experimental and modelling investigation of the deformation, drag and break-up of drizzle droplets subjected to strong aerodynamics forces in relation to SLD aircraft icing," PhD Thesis, Cranfield University, 2005.
- [7] N. Z. Mehdizadeh, S. Chandra and J. Mostaghimi, "Formation of fingers around the edges of a drop hitting a metal plate with high velocity," *Journal of Fluid Mechanics*, vol. 510, no. 1, pp. 353-373, 2004.
- [8] A. Pueyo and W. G. Habashi, "Ice detectors, probes and sensors," in *15th International Icing Course - Simulation Methods used for the Inflight Icing Certification of Aircraft, Rotorcraft and Jet Engines*, Montreal, 2017.
- [9] H. Beaugendre, F. Morency and W. G. Habashi, "FENSAP-ICE's three-dimensional in-flight ice accretion module: ICE3D," *Journal of Aircraft*, vol. 40, no. 2, pp. 239-247, 2003.
- [10] G. Ruff and B. M. Berkowitz, "Users manual for the NASA Lewis ice accretion prediction code (LEWICE)," NASA, 1990.
- [11] R. A. Gingold and J. J. Monaghan, "Smoothed particle hydrodynamics: theory and application to non-spherical starts," *Monthly Notices of the Royal Astronomical Society*, vol. 181, no. 3, pp. 375-389, 1977.
- [12] T. Belytschko, C. Parimi, N. Moës and N. S. Shuji Usui, "Structured extended finite element methods for solids defined by implicit surfaces," *International Journal for Numerical Methods in Engineering*, vol. 56, no. 4, pp. 609-635, 2003.
- [13] J. Favier, A. Revell and A. Pinelli, "A Lattice-Boltzmann-Immersed boundary method to simulate the fluid interaction with moving and slender flexible objects," *Journal of Computational Physics*, vol. 261, no. 1, pp. 145-161, 2014.
- [14] C. S. Peskin, "The immersed boundary method," *Acta Numerica*, vol. 11, no. 1, pp. 479-517, 2002.
- [15] E. M. Saiki and S. Biringen, "Numerical simulation of a cylinder in uniform flow: application of the virtual boundary method," *Journal of Computational Physics*, vol. 123, no. 2, pp. 450-465, 1996.

- [16] T. Ye, R. Mittal, H. S. Udaykumar and W. Shyyb, "An accurate Cartesian grid method for viscous incompressible flows with complex immersed boundaries," *Journal of Computational Physics*, vol. 156, no. 2, pp. 209-240, 1999.
- [17] N. Moës, J. Dolbow and T. Belytschko, "A finite element method for crack growth without remeshing," *International Journal for Numerical Methods in Engineering*, vol. 46, no. 1, pp. 131-150, 1999.
- [18] A. Hrennikoff, "Solution of problems of elasticity by the framework method," *Journal of Applied Mechanics*, vol. 8, no. 4, pp. 169-175, 1941.
- [19] R. Courant, "Variational methods for the solution of problems of equilibrium and vibrations," *Bulletin of the American Mathematical Society*, vol. 49, no. 1, pp. 1-23, 1943.
- [20] C. Beckermann, H. Diepers, I. Steinbach, A. Karma and X. Tong, "Modeling melt convection in phase-field simulations of solidification," *Journal of Computational Physics*, vol. 154, no. 2, pp. 468-496, 1999.
- [21] S. Singh and R. Bhargava, "Numerical simulation of a phase transition problem with natural convection using hybrid FEM/EFGM technique," *International Journal of Numerical Methods*, vol. 25, no. 3, pp. 570-592, 2015.
- [22] V. R. Voller, M. Cross and N. C. Markatos, "An enthalpy method for convection/diffusion phase change," *International Journal of Numerical Methods*, vol. 71, no. 10, pp. 1282-1296, 2013.
- [23] A. Gerstenberger, "An extended finite element method/Lagrange multiplier based approach for fluid structure interaction," *Computer Methods in Applied Mechanics and Engineering*, vol. 197, no. 19, pp. 1699-1714, 2008.
- [24] A. Gerstenberger and W. Wall, "An extended finite element method based approach for large deformation fluid-structure interaction," in *European Conference on Computational Fluid Dynamics*, Netherlands, 2005.
- [25] A. Gerstenberger, "An XFEM based fixed-grid approach to fluid-structure interaction," PhD Thesis, Technische Universität München, Munich, 2010.
- [26] J. Chessa, P. Smolinski and T. Belytschko, "The extended finite element method (XFEM) for solidification problems," *International Journal of Numerical Methods*, vol. 53, no. 8, pp. 1959-1977, 2002.
- [27] N. Zabaras, B. Ganapathysubramanian and L. Tan, "Modeling dendritic solidification with melt convection using extended finite element method," *Journal of Computational Physics*, vol. 218, no. 1, pp. 200-227, 2006.
- [28] P. Stapor, "A two-dimensional simulation of solidification processes in materials with thermo-dependent properties," *International Journal of Numerical Methods*, vol. 26, no. 6, pp. 1661-1683, 2016.
- [29] D. Martin, H. Chaouki, J.-L. Robert, D. Ziegler and M. Fafard, "A XFEM phase change model with convection," *Frontiers in Heat and Mass Transfer*, vol. 10, no. 18, pp. 1-11, 2018.
- [30] D. Martin, H. Chaouki, J.-L. Robert, D. Ziegler and M. Fafard, "Modelling of phase change with non-constant density using XFEM and a Lagrange multiplier," *Frontiers in Heat and Mass Transfer*, vol. 7, no. 40, pp. 1-11, 2017.

- [31] M. Li, H. Chaouki, J.-L. Robert, D. Ziegler, D. Martin and M. Fafard, "Numerical simulation of Stefan problem with ensuing melt flow through XFEM/level set method," *Finite Elements in Analysis and Design*, vol. 148, no. 1, pp. 13-26, 2018.
- [32] W. Woo and A. Mujumdar, "Effects of electric and magnetic field on freezing and possible relevance in freeze drying," *Drying Technology*, vol. 28, no. 1, pp. 433-443, 2010.
- [33] H. R. Pruppacher and J. D. Klett, *Microphysics of clouds and precipitation*, 2nd Edition: Springer, 1997.
- [34] C. Tropea, M. Schremb and I. Roisman, "Physics of SLD impact and solidification," in *7th European Conference for Aeronautics and Aerospace Sciences*, 2017.
- [35] L. Wang, W. Kong, F. Wang and H. Liu, "Effect of nucleation time on freezing morphology and type of a water droplet impacting onto cold substrate," *International Journal of Heat and Mass Transfer*, vol. 130, no. 1, pp. 831-842, 2019.
- [36] M. Schremb, J. M. Campbell, H. K. Christenson and C. Tropea, "Ice layer spreading along a solid substrate during solidification of supercooled water: experiments and modeling," *Langmuir*, vol. 33, no. 19, pp. 4870-4877, 2017.
- [37] W. Kong and H. Liu, "A theory on the icing evolution of supercooled water near solid substrate," *International Journal of Heat and Mass Transfer*, vol. 91, no. 1, pp. 1217-1236, 2015.
- [38] Z. Jin, H. Zhang and Z. Yang, "Experimental investigation of the impact and freezing of a water droplet on ice surface," *International Journal of Heat and Mass Transfer*, vol. 109, no. 1, pp. 716-724, 2017.
- [39] Y. H. Tseng and J. H. Ferziger, "A ghost-cell immersed boundary method for flow in complex geometry," *Journal of Computational Physics*, vol. 192, no. 2, pp. 593-623, 2003.
- [40] H. Bandringa, "Immersed boundary methods," PhD Thesis, Institute of Mathematics and Computing Science, Netherlands, 2010.
- [41] R. Mittal and G. Iaccarino, "Immersed boundary methods," *Annual Review of Fluid Mechanics*, vol. 37, no. 1, pp. 239-261, 2005.
- [42] D. Goldstein, R. Handler and L. Sirovich, "Modeling a no-slip flow boundary with an external force fields," *Journal of Computational Physics*, vol. 105, no. 2, pp. 354-366, 1993.
- [43] K. Khadra, P. Angot, S. Parneix and J.-P. Caltagirone, "Fictitious domain approach for numerical modelling of Navier-Stokes equations," *International Journal for Numerical Methods in Fluids*, vol. 34, no. 8, pp. 651-684, 2000.
- [44] E. A. Fadlun, R. Verzicco, P. Orlandi and J. Mohd-Yusof, "Combined immersed-boundary finite-difference methods for three-dimensional complex flow simulation," *Journal of Computational Physics*, vol. 161, no. 1, pp. 35-60, 2000.
- [45] R. Glowinski, T. W. Pan and J. Périaux, "Distributed Lagrange multiplier methods for incompressible viscous flow around moving rigid bodies," *Computational Methods in Applied Mechanical Engineering*, vol. 151, no. 1, pp. 181-194, 1998.
- [46] S. Majumdar, G. Iaccarino and P. Durbin, "RANS solver with adaptive structured boundary non-conforming grids," Center for Turbulence Annual Research Briefs, 2001.

- [47] F. Gibou, R. P. Fedkiw, L. T. Cheng and M. Kang, "A second-order-accurate symmetric discretization of the Poisson equation on irregular domains," *Journal of Computational Physics*, vol. 207, no. 2, pp. 457-492, 2002.
- [48] R. P. Fedkiw, T. Aslam, B. Merriman and S. Osher, "A non-oscillatory Eulerian approach to interfaces in multimaterial flows (the ghost fluid method)," *Journal of Computational Physics*, vol. 152, no. 2, pp. 457-492, 1999.
- [49] J. Chessa and T. Belytschko, "An extended finite element method for two-phase fluids," *Journal of Applied Mechanics*, vol. 70, no. 1, pp. 10-17, 2003.
- [50] A. R. Khoei, *Extended finite element method: theory and applications*, John Wiley & Sons, Ltd, 2014.
- [51] T. P. Fries, "A corrected XFEM approximation without problems in blending elements," *International Journal for Methods in Mechanical Engineering*, vol. 75, no. 5, pp. 503-532, 2008.
- [52] R. Gracie, H. Wang and T. Belytschko, "Blending in the extended finite element method by discontinuous Galerkin and assumed strain methods," *International Journal for Numerical Methods in Engineering*, vol. 74, no. 11, pp. 1645-1669, 2008.
- [53] H. Sauerland and T.-P. Fries, "The extended finite element method for two-phase and free-surface flows: a systematic study," *Journal of Computational Physics*, vol. 230, no. 9, pp. 3369-3390, 2011.
- [54] C. Vuik, "Some historical notes on the Stefan problem," Delft University of Technology, 1992.
- [55] H. Ji and J. E. Doblrow, "On strategies for enforcing interfacial constraints and evaluating jump conditions with the extended finite element method," *International Journal of Numerical Methods in Engineering*, vol. 60, no. 6, pp. 2508-2535, 2004.
- [56] S. Osher and R. Fedwik, *Level set methods and dynamic implicit surfaces*, Springer Science & Business Media, 2006.
- [57] F. Shakib, "Finite element analysis of the compressible Euler and Navier-Stokes equations," PhD Thesis, Stanford University, Stanford, 1988.
- [58] T. Belytschko, "Structured extended finite element methods for solids defined by implicit surfaces," *International Journal for Numerical Methods in Engineering*, vol. 56, no. 4, pp. 609-635, 2003.
- [59] K. Kamran, R. Rossi and E. Oñate, "A locally extended finite element method for the simulation of multi-fluid flows using a particle level set method," *Computer Methods in Applied Mechanics and Engineering*, vol. 294, no. 1, pp. 1-18, 2015.
- [60] A. Bakkar, "A finite element-level set Eulerian model of supercooled large droplet dynamics," PhD Thesis, McGill University, Montreal, 2017.
- [61] S. Mirjalili, S. S. Jain and M. S. Dodd, "Interface-capturing methods for two-phase flows: an overview and recent developments," Center for Turbulence Research, 2017.
- [62] J. A. Sethian, "A fast marching level set method for monotonically advancing fronts," *Applied Mathematics*, vol. 93, no. 1, pp. 1591-1595, 1996.
- [63] A. Bakkar, W. G. Habashi, M. Fossati and G. S. Baruzzi, "A hybrid Taylor–Galerkin variational multi-scale stabilization method for the level set equation," *Computers & Fluids*, vol. 121, no. 1, pp. 192-205, 2015.

- [64] S.-G. Cai, A. Ouahsine, J. Favier, Y. Hoarau and H. Smaoui, "Immersed boundary method for the simulation of lid-driven cavity flow with an embedded cylinder," in *International Conference on Computational Methods for Coupled problems*, Venice, CIMNE Paper 2015-01462151, 2015.
- [65] E. D. dos Santos, A. P. Petry, L. A. O. Rocha and F. H. Franca, "Numerical study of forced convection lid-driven cavity flows using LES (large eddy simulation)," *Journal of Energy and Power Engineering*, vol. 7, no. 1, pp. 1669-1680, 2013.
- [66] Fluent, (*Version 6.3.16*), ANSYS, Inc., 2007.
- [67] A. W. Islam, M. A. R. Sharif and E. S. Carlson, "Mixed convection in a lid driven cavity with an isothermally heated square blockage inside," *International Journal of Heat and Mass Transfer*, vol. 55, no. 19, pp. 5244-5255, 2012.
- [68] D. Martin, H. Chaouki, J.-L. Rober, D. Ziegler and M. Fafard, "A XFEM Lagrange multiplier technique for Stefan problems," *Frontiers in Heat and Mass Transfer*, vol. 7, no. 31, pp. 1-9, 2016.
- [69] D. Martin, "Multiphase modelling of melting/solidification with high density variations using XFEM," PhD Thesis, Université Laval, 2016.
- [70] A. S. Usmani, R. W. Lewis and K. N. Seetharamu, "Finite element modeling of natural-convection controlled change of phase," *International Journal for Numerical Methods in Fluids*, vol. 14, no. 1, pp. 1019-1036, 1992.